ISBN 978-82-471-1537-4 (printed ver.)
ISBN 978-82-471-1538-1 (electronic ver.)
ISSN 1503-8181

Espen Berg

Doctoral Thesis

Doctoral theses at NTNU, 2009:80

Espen Berg

Numerical analysis of ductile fracture in surface cracked shells

NTNU
Norwegian University of
Science and Technology

Thesis for the degree of
philosophiae doctor

Faculty of Engineering Science and Technology
Department of Structural Engineering

NTNU
Norwegian University of
Science and Technology

Doctoral theses at NTNU, 2009:80

NTNU

Espen Berg

Numerical analysis of ductile fracture in surface cracked shells

Thesis for the degree of philosophiae doctor

Trondheim, June 2009

Norwegian University of
Science and Technology
Faculty of Engineering Science and Technology
Department of Structural Engineering

NTNU
Norwegian University of
Science and Technology

NTNU
Norwegian University of Science and Technology

Thesis for the degree of philosophiae doctor

Faculty of Engineering Science and Technology
Department of Structural Engineering

ISBN 978-82-471-1537-4 (printed ver.)
ISBN 978-82-471-1538-1 (electronic ver.)
ISSN 1503-8181

Doctoral Theses at NTNU, 2009:80

Printed by Tapir Uttrykk

Numerical analysis of ductile fracture in surface cracked shells

Espen Berg

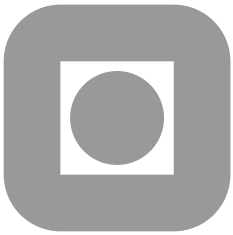

Norwegian University of Science and Technology
Faculty of Engineering Science and Technology
Department of Structural Engineering
Trondheim, Norway

Preface

This doctoral thesis is submitted to the Norwegian University of Science and Technology (NTNU) for the degree Philosophiae Doctor.

The project work has been carried out at Department of Structural Engineering, NTNU. My supervisor has been Professor Bjørn Skallerud and my co-supervisors have been Kjell Holthe and Professor Christian Thaulow (Department of Engineering Design and Materials, NTNU). The work has been financially supported by a scholarship from the Norwegian University of Science and Technology.

I have been the main author for the three latter papers in this thesis. I have been responsible for the simulations in all the papers included in this thesis. I have also been responsible for the implementations presented herein. In paper 4, Professor Kjell Holthe contributed to the plasticity formulation for the line-spring element. I have received very helpful contributions from the co-authors regarding comments and corrections of the papers.

Acknowledgements

When doing a PhD, there are a numerous amount of people involved in different ways. Some of these people deserve my acknowledgements for their contributions.

First I want to thank my supervisor Professor Bjørn Skallerud for his guidance and support of my work. I have learnt a lot from you and you always give me constructive feedback straight away. My co-supervisors, Professor Christian Thaulow and Professor Kjell Holthe, also deserves my acknowledgements for their everlasting ideas and discussions.

I also want to give my gratitude to my fellow PhD students and colleagues for support, inspiration and social gatherings throughout these years. To all my friends everywhere – you are not forgotten.

Dr. Erling Østby in SINTEF also deserves my acknowledgements for many fruitful discussions and advices. Then my colleagues in LINKftr who have always encouraged and inspired me to complete this project. Your support has meant a lot to me. Also the joint industry project, Fracture Control Offshore Pipelines, deserves acknowledgements for providing data from large scale experiments.

Then my wife, Tone, is highly acknowledged for her patience and support during the years of PhD-work. Our daughter, Marie, who was born during the PhD must be mentioned here. To get a baby when you are doing a PhD does not always speed up the work, but you get some new perspective of life you can not get anywhere else, and which is so valuable. The ultimate joy you show when I pick you up in the kindergarten in the afternoon lifts me up and gives me motivation.

Finally my parents, sister and close family deserve special thank you for always supporting me in what I am doing.

Contents

Chapter 1

Introduction and motivation

1.1 Structure of the thesis

This thesis consists of an introduction section followed by four separate journal papers which have been completed during the last four years. During this period I have also contributed to four international conferences. The conference proceedings papers are not included in this thesis.

To get a theoretical background for the content of the journal papers, an introduction part is included. This introduction is organised in six chapters. The first chapter contains the motivation and aim for the study. The second chapter gives a brief summary of the definitions and concepts in elastic plastic fracture mechanics. The third and fourth chapter presents the line-spring theory and material model of the ANDES shell finite element in detail. This has been presented before in different journal articles, hence it is not included in the articles in this thesis. Chapter five gives a brief overview of some kinematic hardening models. The sixth chapter gives a short summary of the appended journal papers, and the seventh chapter gives some conclusions and suggestions for further work.

1.2 Motivation

The main topic of this thesis is fracture mechanics assessment of offshore pipelines with transversal (circumferential) surface defects. Offshore pipelines are used to transport oil and gas e.g. from the platforms to land-based terminals. The length of a pipeline can be from several kilometres to several hundred kilometres. The pipelines may be subjected to different loadings during it's lifetime which depends on the situation and life phase.

Installation of pipelines can be done in several ways. Three methods, J-lay, S-lay and Reeling are shown in Fig. 1.1. The examples in Fig. 1.1 expose the pipeline to large plastic strains. Common for most pipe laying methods is the joining of pipe segments by girth welding. Welds introduce some defects to the construction and it is important to know how these eventual

cracks evolve in order to assess structural integrity and decide whether the pipeline needs to be repaired or not.

For J-laying and S-laying joining of pipe segments are performed on the vessel. Plastic strains arise at touchdown and in the sagbend region, which is located between touchdown and the vertical region in Fig. 1.1. For S-laying the region where the pipe leaves the stinger also imposes the same scale of plastic strains. Reeling is an alternative method where pipe segments are welded together on land before reeled onto a spool on a ship. This reeled pipe has both large tensile and compressive plastic strains. A defect might cause crack growth beyond the acceptance limits.

Cyclic plastic strains are potentially introduced in all three methods in Fig. 1.1. These cyclic plastic strains introduce a very low cycle fatigue behaviour which must be considered. For reeling, a plastic strain cycle is performed as the pipe is first reeled to the spool on a ship before it is unreeled offshore. The sag-bend in the region between the vessel and touchdown point on the seabed gives another plastic strain cycle. If a defect is detected and the pipe must be reeled back on the spool again for repairing, yet another strain cycle occurs.

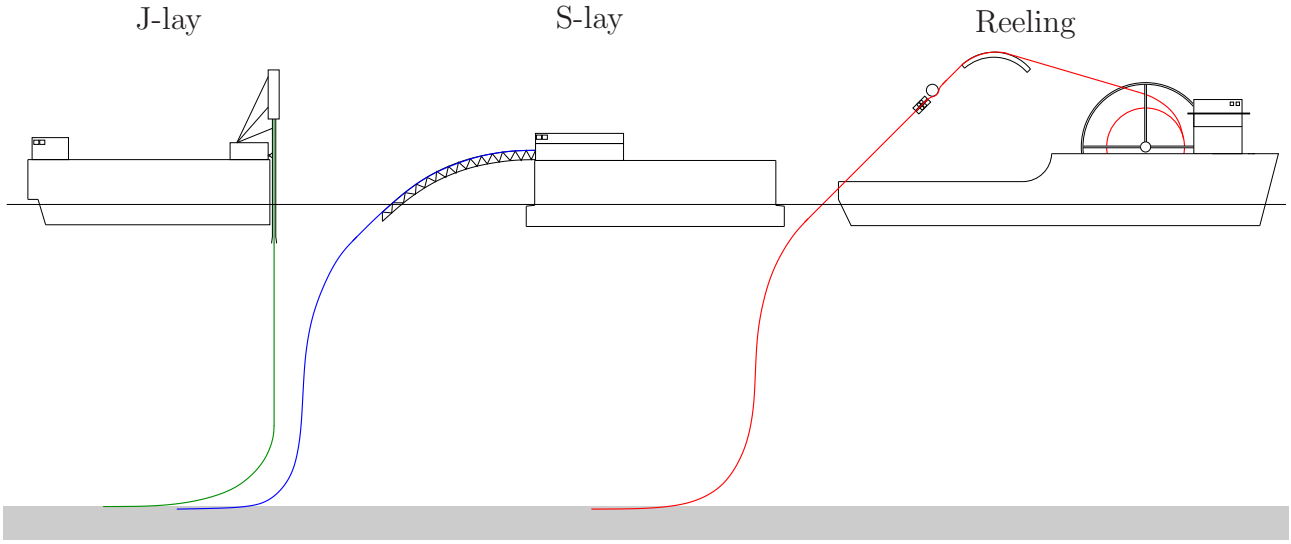

Figure 1.1: J-lay, S-lay and reeling techniques

The operational phase is the longest time period in the life of a pipeline. Here the pipelines is exposed to different loading depending on many factors.

Due to the topography on the seabed, the pipeline will have to cross free spans on it's route. These free spans can impose large bending moments that may give plastic deformations. Also seabed movements can introduce new free spans, or the pipe can be moved out of it's original position which gives raise to external forces acting on the pipe.

Internal pressure is another important factor. An increasing internal pressure will give an increasing hoop stress in the pipeline which prevents the pipe from buckling. This effect can change the failure mode from a global structural failure to a fracture failure problem where the crack can grow through the wall thickness and cause leakage and pollution. Thermal forces also result in large plastic deformations such as upheaval or lateral buckling. During shutdowns and

start-ups the internal pressure in the pipeline decreases and increases rapidly, which can lead to local forces of magnitude large enough to cause low cycle fatigue crack growth.

Monitoring of the structural integrity of a pipeline is performed continuously to prevent structural failure, local or global. When a defect is detected efficient tools for the operator is needed to decide whether a shutdown to repair is needed. Efficient and accurate calculation tools can also assist the designer in constructing a safer and more cost-effective structure for the given installation laying technique and operational conditions.

1.3 Aims for the study

The aim for the present study has been to utilise the line-spring element in a numerical model for fracture assessment of pipe segments where large plastic strains are present. This approach is called strain based design. Efficient numerical tools with the capability of capturing both the fracture failure mode and the global structural failure mode is demanded.

Two-parameter fracture assessments will be a focus throughout the study. It has been shown that the fracture toughness is not only a material parameter, but also depends on the geometry and mode of loading. This effect is called constraint. The aim is to use the T-stress as the constraint parameter also for large scale yielding. The T-stress is readily available from the line-spring element which is to be used in the numerical analyses. Thaulow et al. [41] demonstrated that the crack growth resistance curve could be normalised using the T-stress. This methodology was implemented in this study and used actively in numerical analyses with success.

Also a study to investigate the effect of crack growth in the circumferential direction for a surface crack was carried out. The results from this study was implemented in the finite element code.

In the installation phase a pipeline is subjected to large plastic strain cycles, hence a low cycle fatigue or tearing fatigue crack growth study should be performed. During the operational phase of a pipeline the load cycles are mainly of elastic character, hence this is not included in the present study. A material model for the shell element and line-spring element to account for non-linear cyclic plasticity must be implemented in the software.

Comparisons with large scale experiments are important for validations of numerical models. Large scale experiments usually can not be carried out in a PhD project, hence external projects or studies which can provide experimental results must be available. The joint industry project, Fracture Control Offshore Pipelines, carried out large scale experiments of pipe segments subjected to bending loading and internal pressure (see Østby and Hellesvik [28]). Nyhus et al. [23] carried out large scale experiments of pipe segments subjected to large plastic cyclic bending loading. These experiments will be used in the validation of the numerical analyses.

Chapter 2

Fracture mechanics theory

2.1 Elastic-plastic fracture mechanics

For ductile materials subjected to large plastic deformations, linear elastic fracture mechanics (LEFM) using the stress intensity factor, K_I, to characterise the near crack tip stress field, is invalidated. Due to the large scale yielding behaviour, other fracture mechanics models taking the possible non-linear behaviour into account are required.

The J contour integral was proposed by Rice [31] as a fracture characterising parameter for non-linear materials. The J integral is founded on the energy release rate and is assumed to be path independent. The J-integral assumes an isotropic and non-dissipative material and rate independency. The J-integral is written as a line integral as expressed in Eq. 2.1 (see also Fig. 2.1).

$$J = \int_{\Gamma} \left(w dy - T_i \frac{\partial u_i}{\partial x} ds \right) \tag{2.1}$$

where w is the strain energy density, T_i are the components of the traction vector, u_i are the components of the displacement vector and ds is the length of an increment along the contour Γ.

An alternative to the J-integral is to use the crack tip opening displacement ($CTOD$) as a measure of the crack driving force. The $CTOD$ is defined as shown in Fig. 2.2. Shih [36] demonstrated the existence of a linear relation between the J-integral and $CTOD$ for a stationary and growing crack beyond LEFM (see Eq. 2.2).

$$J = m\sigma_0\delta \tag{2.2}$$

where m is a dimensionless constant depending on the material properties and stress state (see Anderson [2]). According to the literature, the value of m will be in the range between 1 and 2. Skallerud [37] proposed an analytical function for m based on the local bending moment. Østby [27] later presented an analytical expression for m based on the ratio between the yield stress and tensile strength from the nominal stress-strain curve. In this study m is set as 1.5.

This study also makes use of the $CTOD$ as fracture parameter.

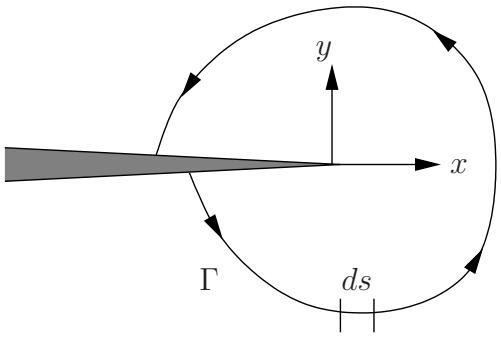

Figure 2.1: An arbitrary contour around the crack tip for evaluation of the J-integral

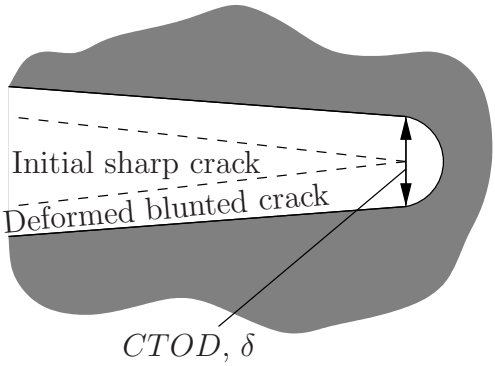

Figure 2.2: An initial sharp crack is blunted due to plastic deformations. The $CTOD$ is shown

2.2 Two-parameter fracture mechanics

In addition to the material properties, the geometry and loading conditions have an influence of the conditions surrounding the crack tip area. Because of this, the fracture toughness can not be treated as a true material parameter. The term "constraint" defines this dependency on the geometry and loading conditions. Thaulow et al. [41] measured the constraint level for different fracture mechanics specimens. The results for the fracture toughness as a function of the constraint is schematically shown in Fig. 2.3.

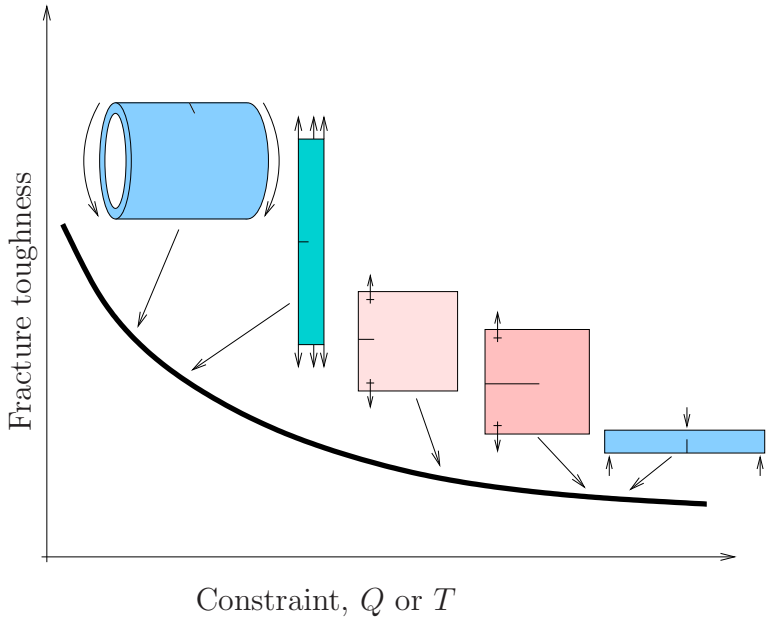

Figure 2.3: Variation of the fracture toughness due to different constraint level

Several constraint measures have been proposed over the years, with the Q-parameter and the T-stress as the two most widely used. The Q-parameter was introduced by O'Dowd and

Shih [25, 26] where they approximated the difference field ahead of the crack tip as

$$\sigma_{ij} = \sigma_{ij}^{ref} + Q\sigma_0\delta_{ij} \tag{2.3}$$

σ_{ij}^{ref} is the reference stress field with high stress triaxiality, e.g. HRR stress field. σ_0 is the yield stress and δ_{ij} is the Kronecker's delta symbol.

Another approach to quantify the constraint effects is to use the T-stress which is the first non-singular term in the William's power series expansion for the stress component normal to the crack front (see Eq. 2.4).

$$\sigma_{ij} = \frac{K_I}{\sqrt{2\pi r}} f_{ij}(\theta) + \begin{bmatrix} T & 0 & 0 \\ 0 & 0 & 0 \\ 0 & 0 & \nu T \end{bmatrix} \tag{2.4}$$

The T-stress was presented by Larsson and Carlsson [16] and Du and Hancock [9] with restrictions to small scale yielding conditions. Bétegon and Hancock [4] and Hancock et al. [11] argue that the T-stress can also be used under large-scale yielding conditions. Jayadevan et al. [14] have provided a compendium with T-stress solutions for pipe geometries.

Constraint measurements is an important task in ductile tearing problems. Since the fracture toughness is not a pure material parameter, neither will the crack growth resistance curve be. Ainsworth and O'Dowd [1] proposed a methodology to correct the crack growth resistance curve using the T-stress. To perform the correction, a reference curve is multiplied by a function as

$$CTOD^{corr} = CTOD^{ref} \cdot g(T) \tag{2.5}$$

$$g(T) = \begin{cases} \left[1 + \alpha\left(-\frac{T(\Delta a)}{\sigma_0}\right)^m\right]^2 & \text{for } T < 0 \\ 1 & \text{for } T \geq 0 \end{cases} \tag{2.6}$$

where α and m are two parameters that need to be determined from experimental crack growth resistance curves. Nyhus et al. [24] demonstrated how crack growth resistance curves can be normalised using the equation from Ainsworth and O'Dowd. A result is shown in Fig. 2.4.

The reference crack growth resistance curve is chosen as one of the curves used in the determination of the parameters α and m.

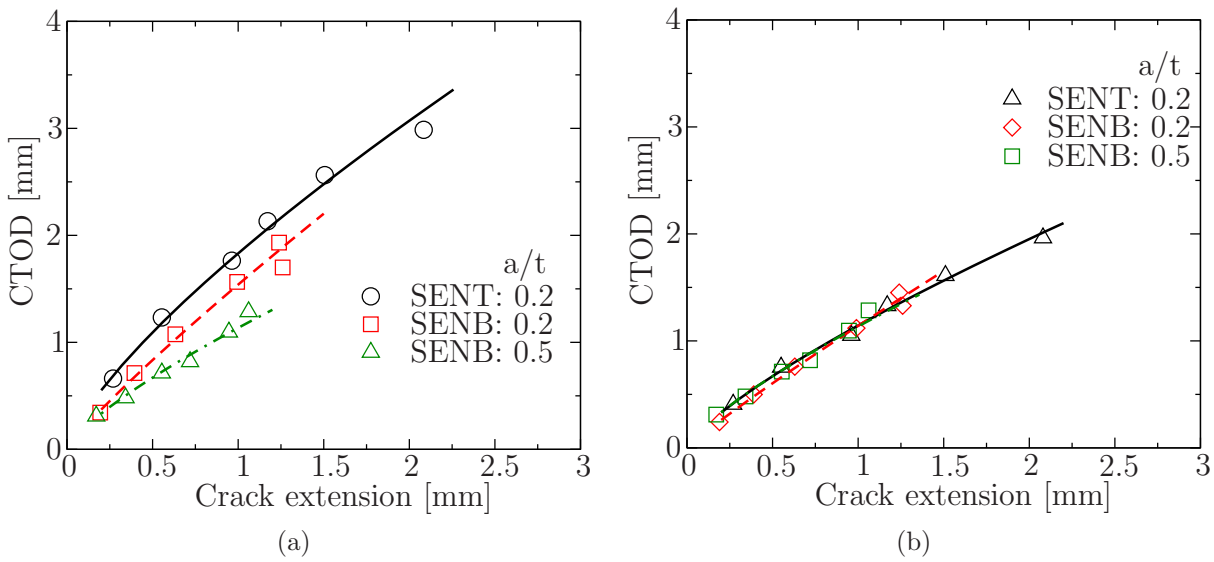

Figure 2.4: (a) the experimental crack growth resistance curves for X65 steel and (b) constraint corrected curves [24]

Chapter 3

Line-spring model

The line-spring model is used to transform a surface cracked thin walled structure to a two dimensional model using shell- and line-spring finite elements. The shell model contains a through slit of where the crack is located. The line-spring elements are used to add stiffness to the through slit depending on the crack geometry. These springs connect the two ends of the through slit. The stiffness of the springs is calculated based on known solutions from single edge notched specimens under plane strain conditions (see Fig. 3.1).

The line-spring model was initially proposed by Rice [32] and Rice and Levy [33] as an approach to compute the stress intensity factor for a surface crack in wide plates. The line-spring element was later extended by Parks and co authors [44],[43],[17], Chiesa et al. [7] and Jayadevan and co authors [14], [13].

The shell element used with the line-spring element in this study is a four noded quadrilateral element, hence the line-spring element is also four noded with linear Gauss interpolation functions.

The line-spring element formulation is based on stress resultant plasticity. The generalised shell resultants transmitted are the membrane force, N, and bending moment, M per unit length. The corresponding work conjugates are the relative separation, Δ, and rotation, θ, respectively.

Two-parameter fracture mechanics utilising the elastic T-stress for the line-spring element was shown by Wang and Parks [43]. With this the constraint level could be computed in the line-spring model.

3.1 Elastic line-spring finite element

The elastic formulation of the line-spring element is used to compute the elastic stress intensity factor. The generalised forces and the generalised displacement in the line-spring element are related through the elastic compliance matrix, C_{ij} as shown in Eq. 3.1.

$$q_i = C_{ij} Q_j \tag{3.1}$$

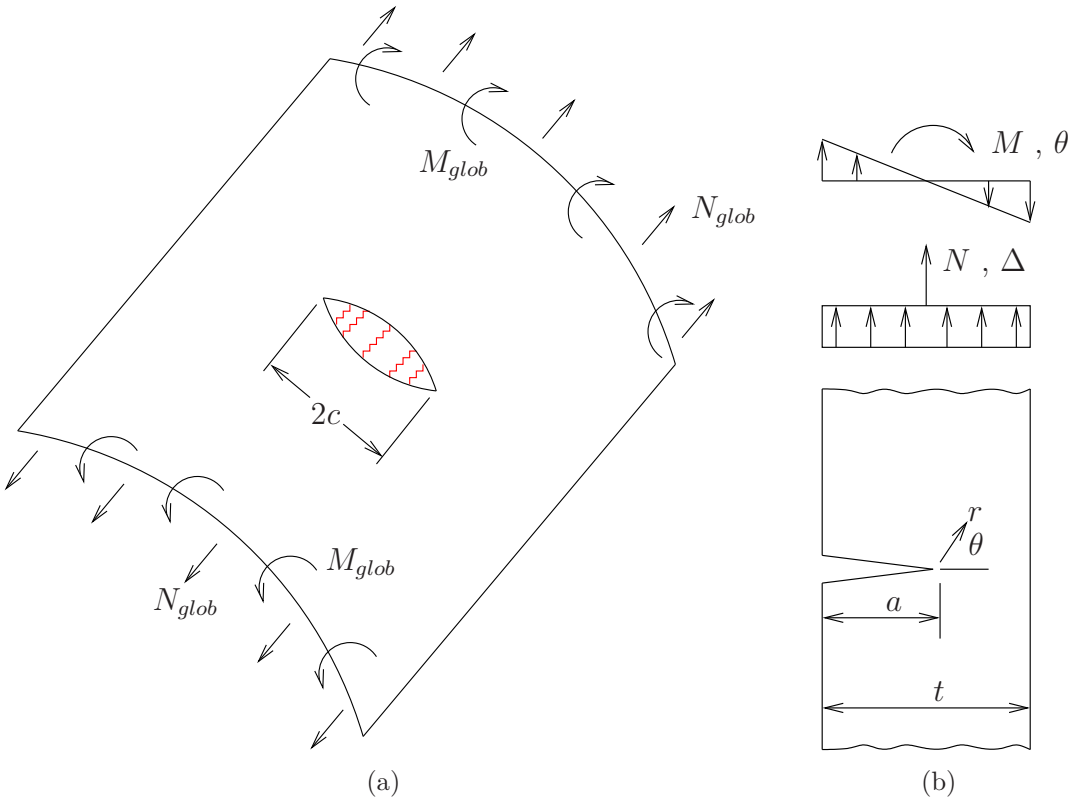

Figure 3.1: (a) two dimensional shell model with line-springs representing the surface crack and (b) the reduced stiffness at any point along the line-spring are obtained from corresponding single edge notched specimens under plane strain conditions

$$[q_i] = \begin{bmatrix} \Delta \\ \theta \end{bmatrix} \quad , \quad [Q_j] = \begin{bmatrix} N \\ M \end{bmatrix} \tag{3.2}$$

where q_i are the generalised displacements and Q_j are the generalised forces. The elastic compliance terms are polynomials depending on the crack depth to thickness ratio, Young's modulus and Poisson's ratio.

$$\begin{aligned} \xi &= \frac{a}{t} \\ f_1 &= 1.12 - 0.231\xi + 10.55\xi^2 - 21.72\xi^3 + 30.39\xi^4 \qquad (3.3) \\ f_2 &= 1.122 - 1.40\xi + 7.33\xi^2 - 13.08\xi^3 + 14.0\xi^4 \qquad (3.4) \end{aligned}$$

It is seen that the polynomials from Eq. 3.3 and 3.4 approach 1.12 when the crack depth to thickness ratio approaches zero. These polynomials are used to form the components of the elastic compliance matrix as shown in Eq. 3.5-3.7. The elastic compliance matrix is symmetric,

thus $C_{12} = C_{21}$.

$$C_{11} = \frac{2\pi\left(1-\nu^2\right)}{Et^2}\int_0^a af_1^2 da \tag{3.5}$$

$$C_{12} = \frac{2\pi\left(1-\nu^2\right)}{E\frac{1}{6}t^3}\int_0^a af_1 f_2 da \tag{3.6}$$

$$C_{22} = \frac{2\pi\left(1-\nu^2\right)}{E\frac{1}{36}t^4}\int_0^a af_2^2 da \tag{3.7}$$

The elastic compliance matrix is calibrated from single edge notched specimens in plane strain conditions subjected to membrane force and/or bending moment using the energy-compliance method proposed by Rice [32].

Mode I stress intensity factor, K_I, is a function of the generalised forces, the crack depth and the wall thickness as presented by Rice and Levy [33]. It is expressed as

$$K_I = \sqrt{\xi}\left(\frac{N}{t}k_N + \frac{6M}{t^2}k_M\right) \tag{3.8}$$

where k_N and k_M are polynomials depending on the crack depth and wall thickness. These polynomials are obtained from stress intensity handbook by Tada et al. [40] and written as

$$k_N = \sqrt{\xi}\left(1.99 - 0.41\xi + 18.70\xi^2 - 38.48\xi^3 + 53.85\xi^4\right) \tag{3.9}$$

$$k_M = \sqrt{\xi}\left(1.99 - 2.47\xi + 12.97\xi^2 - 23.17\xi^3 + 24.80\xi^4\right) \tag{3.10}$$

The elastic part of the crack tip opening displacement for the line-spring element is related to the stress intensity factor, K_I, as expressed in Eq. 3.11.

$$CTOD_{el} = \frac{1-\nu^2}{mE\sigma_0}K_I^2 \tag{3.11}$$

The same approach as for the mode I stress intensity factor is used for the T-stress. The T-stress is computed along the crack front and is expressed as presented by Wang and Parks [43] and shown in Eq. 3.12

$$T = g_i(a,t)Q_i \tag{3.12}$$

where g_i are polynomials dependent on the crack depth and wall thickness. They are calibrated against plane strain single edge notched specimens as presented by Sham [35].

3.2 Elastic-plastic line-spring finite element

The plastic line-spring response is based on a pointwise convex yield surface and an associated flow rule with isotropic hardening. Mode I (normal crack opening) is the only fracture mode in

the current implementation. Skallerud [37] demonstrated the applicability of a combined mode I/II line-spring formulation, but this enhancement is not used herein.

The yield surface, $\Phi(Q_i, a, t, \sigma(\varepsilon^{pl}))$, is based on the work of Lee and Parks [17] who presented a set of tabulated points to describe the yield surfaces for a range of crack depth to thickness ratios. Berg et al. [3] expanded the number of tabulated yield surfaces to refine the transition between crack depth to thickness ratios. Fig. 3.2 shows the location of the corner points which are located where maximum tension or compression in the ligament occurs. The yield surfaces are constructed in the stress resultant space where the x-axis is the normalised bending moment and the y-axis is the normalised membrane force. A linear interpolation between the tabulated surfaces is used to calculate the intermediate surfaces.

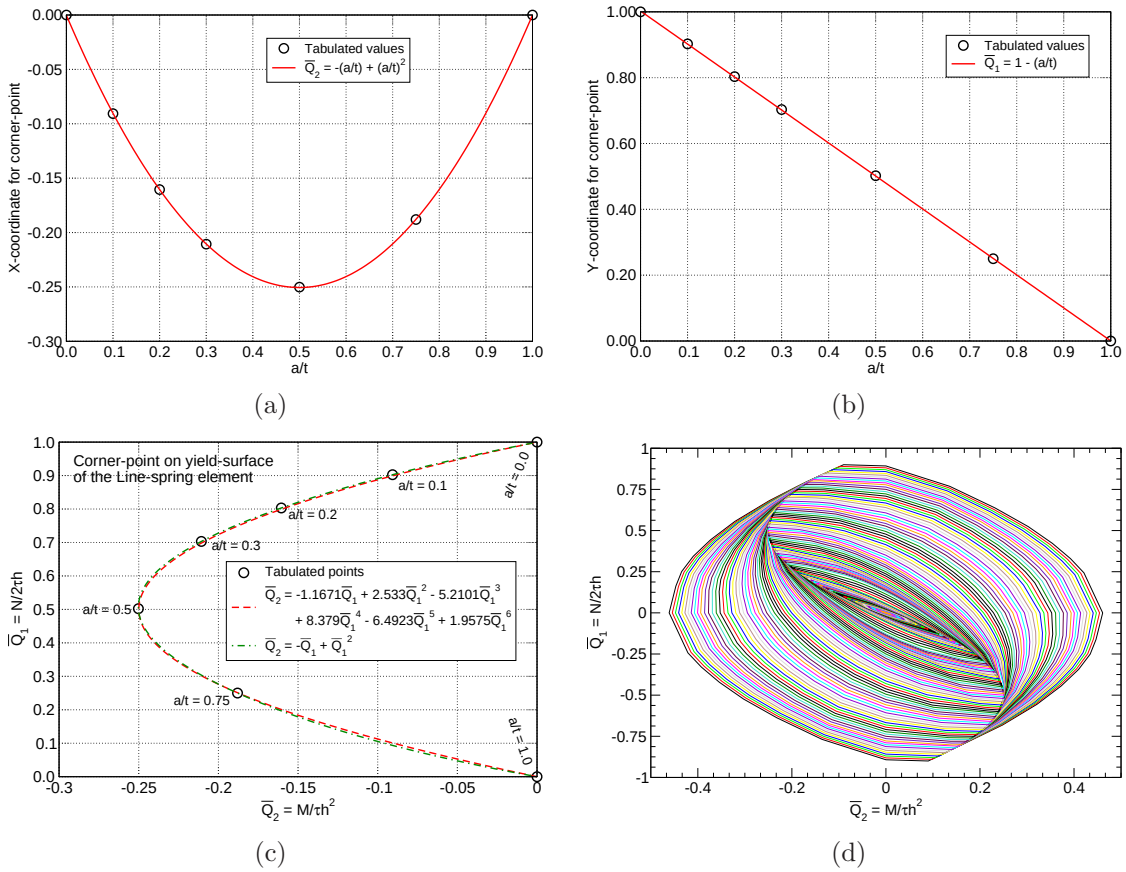

Figure 3.2: (a), (b) and (c) locate the corner-point of the yield-surface, (d) a collection of interpolated yield-surfaces (Berg et al. [3])

The formulation assumes an additive decomposition of the incremental generalised displacements into an elastic and plastic part as shown in Eq. 3.13.

$$dq_i = dq_i^{el} + dq_i^{pl} \tag{3.13}$$

If the product of the stress resultant increment and the normal vector of the yield surface is greater than zero, i.e. $(\partial\Phi/\partial Q_i) \cdot dQ_i > 0$, plastic deformation occurs. The plastic part of the generalised displacement increment is assumed to follow the normality rule, which means that

it can be expressed as the product of the normal vector of the yield surface and a positive scalar as shown in Eq. 3.14.

$$dq_i^{pl} = \Lambda \dot{\Phi}_Q = \Lambda \frac{\partial \Phi}{\partial Q_j} \tag{3.14}$$

The plastic multiplier, Λ is computed from the consistency condition (see Eq. 3.15) during plastic loading. This demands the updated stress point to be located on the yield surface at the end of the load step.

To account for work hardening of the material a hardening law is introduced using the average equivalent plastic strain over the ligament. The material's uniaxial stress strain curve is employed as user input which gives a non-linear material response as demonstrated by Jayadevan et al. [14].

$$d\Phi = \frac{\partial \Phi}{\partial Q_i} dQ_i + \frac{\partial \Phi}{\partial \sigma} d\sigma = 0 \tag{3.15}$$

where $d\sigma$ is found using the slope, h, of the uniaxial stress strain curve as expressed in Eq. 3.16.

$$d\sigma = h d\varepsilon^{pl} \tag{3.16}$$

To relate the plastic part of the generalised displacement increment to the average plastic strain over the remaining ligament, the incremental plastic work per unit length over the ligament is used. The incremental plastic work over the ligament can be written in two ways as proposed by Parks [30] and Parks and White [44]. Following classical plasticity theory, the incremental plastic work using generalised field quantities is given as

$$dW^{pl} = Q_i dq_i^{pl} = \Lambda Q_i \frac{\partial \Phi}{\partial Q_i} \tag{3.17}$$

Parks and White [44] argues that the incremental plastic work can be written as the integral of the continuum over the area, A, of the surface cracked structure as

$$dW^{pl} = \int_A \sigma_{ij} d\varepsilon_{ij}^{pl} dA \tag{3.18}$$

where the area A is a characteristic area of the edge-cracked problem. It is assumed that the yielding only occurs in the remaining ligament, $c = t - a$ (see also Fig. 3.3). Hence the area, A, is defined as the square of the remaining ligament. Using this in the integral in Eq. 3.18, the equation of the incremental plastic work can be approximated to

$$dW^{pl} = f \cdot \sigma_y(\varepsilon^{pl}) \cdot d\varepsilon^{pl} \cdot (t - a)^2 \tag{3.19}$$

where f is a non-dimensional scalar which is called the "strain hardening factor" which is expected to be of order unity.

The incremental stress increment is written as

$$dQ_i = C_{ij} dq_j = C_{ij} \left(dq_j - dq_j^{pl} \right) \tag{3.20}$$

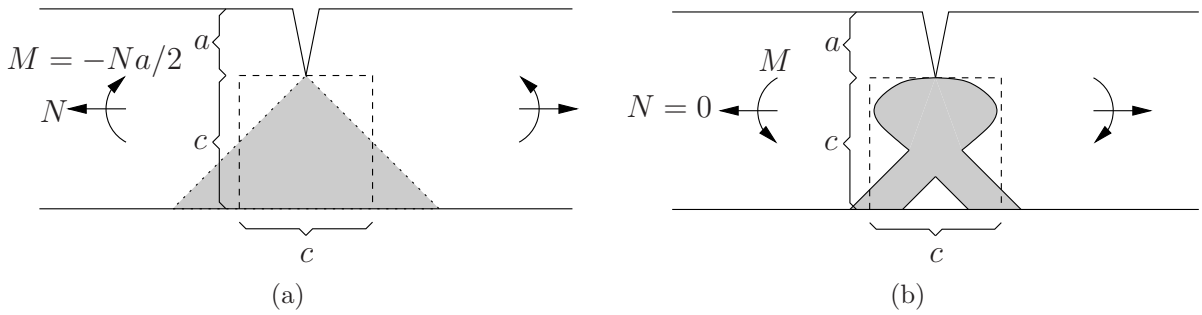

Figure 3.3: Slip line field approximation in the kc-zone for (a) pure tension and (b) pure bending

Combining Eq. 3.17 and Eq. 3.19 gives the following expression for the plastic strain:

$$d\varepsilon^{pl} = \Lambda Q_i \frac{\partial \Phi}{\partial Q_i} \cdot \frac{1}{fc^2\sigma} \tag{3.21}$$

Now combining Eqs. 3.13, 3.14, 3.15, 3.20 and 3.21 the expression for Λ is found as

$$\Lambda = \frac{\dfrac{\partial \Phi}{\partial Q_i} C_{ij}}{\dfrac{\partial \Phi}{\partial Q_m} C_{mn} \dfrac{\partial \Phi}{\partial Q_n} - \dfrac{\partial \Phi}{\partial \sigma} \dfrac{\partial \Phi}{\partial Q_k} Q_k \dfrac{h}{fc^2\sigma}} dq_j \tag{3.22}$$

Inserting Eq. 3.22 into Eq. 3.20 gives the tangent stiffness for as integration point of the line-spring element:

$$C_{ij}^{pl} = C_{ij} - \frac{C_{ik} \dfrac{\partial \Phi}{\partial Q_k} \dfrac{\partial \Phi}{\partial Q_l} C_{lj}}{\dfrac{\partial \Phi}{\partial Q_m} C_{mn} \dfrac{\partial \Phi}{\partial Q_n} - \dfrac{\partial \Phi}{\partial \sigma} \dfrac{\partial \Phi}{\partial Q_o} Q_o \dfrac{h}{fc^2\sigma}} \tag{3.23}$$

The crack driving force J or CTOD are readily available from the line-spring element. As for the generalised displacements, the J or CTOD also follows an additive decomposition of an elastic and a plastic part. The incremental plastic part of the $CTOD$ is expressed as

$$d\delta^{pl} = C_N(Q_N, \sigma_y, a, t) d\Delta^{pl} + C_M(Q_M, \sigma_y, a, t) t d\theta^{pl} \tag{3.24}$$

where the functions C_N and C_M are dimensionless functions presented by Lee and Parks [17].

Lee and Parks [18, 19] introduced ductile crack growth in the line-spring element for fully plastic condition. They used the sliding-off and cracking model of McClintock et al. [21] to obtain the crack tip opening angle in terms of the uniaxial material parameters and the slip-line angle and stress triaxiality (two-parameter fracture mechanics) at the crack tip. This method requires some material parameters in addition to the stress-strain curve to be determined from experiments prior to the numerical analyses. Jayadevan et al. [13] showed the applicability of using the crack growth resistance curve which is in accordance with the established use as defined in BS7910:1999 [5].

The updated crack depth at the end of a load increment is expressed as

$$a^{(i+1)} = a^{(i)} + da^{(i)} \tag{3.25}$$

As mentioned, the constraint level in the line-spring element is computed using the T-stress. This quantity is based on elastic assumptions, but Lee and Parks [17] proposed to extend the use of Eq. 3.12 from the elastic-plastic line-spring behaviour using the current values of the generalised forces, M and N. Under linear-elastic conditions the ratio between the generalised forces is constant, but for elastic-plastic conditions, the ratio is varying with the loading and this is immediately taken care of in the computation of the T-stress. Jayadevan et al. [14] showed the applicability of using this "elastic-plastic T-stress" for the line-spring element.

Chapter 4

ANDES shell finite element

The shell element used together with the line-spring element in this study is a high-performance and non-conforming thin shell finite element based on assumed natural deviatoric strains, denoted ANDES. The ANDES element was initially developed by Felippa and Militello [10]. It was further extended by Skallerud and Haugen [38] to handle large rotations and inelastic behaviour. The ANDES shell finite element is derived in a co-rotated formulation which gives a stringent way of extracting only the strains and curvatures producing deformations in the element. The strains at element level is assumed to be small, but the global deformations can still be large. The derivations for the co-rotated ANDES finite element are rather lengthy and a detailed description is published by Skallerud et al. [39].

The material model is based on stress resultant plasticity. A stress resultant yield criterion derived by Ilyushin is employed and expressed as

$$
\begin{aligned}
f(\bar{\mathbf{n}}, \bar{\mathbf{m}}) &= \sqrt{\frac{\bar{N}}{t^2} + \frac{4s\bar{P}}{\sqrt{3}t^3} + \frac{16\bar{M}}{t^4}} - \sigma_0 = 0 \qquad (4.1)\\
\bar{N} &= N_x^2 + N_y^2 - N_x N_y + 3N_{xy}^2\\
\bar{M} &= M_x^2 + M_y^2 - M_x M_y + 3M_{xy}^2\\
\bar{P} &= N_x M_x + N_y M_y - \frac{1}{2}N_x M_y - \frac{1}{2}N_y M_x + 3N_{xy}M_{xy}\\
s &= \frac{\bar{P}}{\|\bar{P}\|} = \pm 1
\end{aligned}
$$

Writing the stress resultant vector in an integration point as $\boldsymbol{\sigma} = [\bar{\mathbf{n}}, \bar{\mathbf{m}}]^T$, the yield criterion from Eq. 4.1 can be expressed in quadratic form (see Matthies [20] and Ibrahimbegovic and

Frey [12]) as

$$f = \boldsymbol{\sigma}^T \mathbf{A} \boldsymbol{\sigma} - \left(1 + \frac{H\varepsilon_{pl}}{\sigma_0}\right)^2 = 0 \tag{4.2}$$

$$\mathbf{A} = \begin{bmatrix} \frac{1}{n_0^2}\bar{\mathbf{A}} & \frac{s}{2\sqrt{3}m_0 n_0}\bar{\mathbf{A}} \\ \frac{s}{2\sqrt{3}m_0 n_0}\bar{\mathbf{A}} & \frac{1}{m_0^2}\bar{\mathbf{A}} \end{bmatrix} \qquad \bar{\mathbf{A}} = \frac{1}{2}\begin{bmatrix} 2 & -1 & 0 \\ -1 & 2 & 0 \\ 0 & 0 & 6 \end{bmatrix} \tag{4.3}$$

$$m_0 = \frac{1}{4}\sigma_0 t^2 \quad , \quad n_0 = \sigma_0 t$$

Skallerud and Haugen [38] simplified the original Ilyushin yield criterion from Eq. 4.1 by setting the parameter s to zero. The yield surface is now constructed as a circle in the MN space. The Ilyushin and the simplified yield surface are plotted in Fig. 4.1. It is seen that the maximum difference is about 12% and is located where membrane force and bending moment are balanced. $s = 0$ removes the numbers on the off-diagonal of the $\bar{\mathbf{A}}$ matrix which also removes the corners on the Ilyushin yield surface. The simplification where $s = 0$ is used herein. Using this stress resultant yield criterion one does not need to perform a through the thickness integration, hence the stress resultant update for the element is very fast.

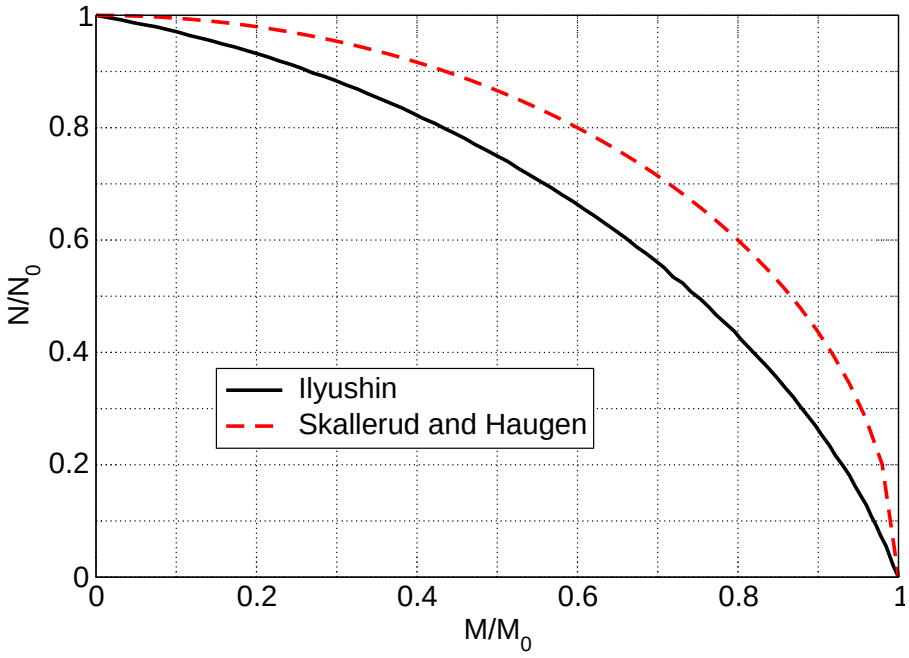

Figure 4.1: Ilyushin and simplified yield surface in the MN space [38]

Implicit backward Euler stress update scheme is being used for the stress resultant stress update in the ANDES finite element. An associated flow rule reads

$$\Delta\boldsymbol{\varepsilon}_{pl,n+1} = \Delta\lambda_{n+1}\frac{\partial f}{\partial \boldsymbol{\sigma}_{n+1}} = 2\Delta\lambda_{n+1}\mathbf{A}\boldsymbol{\sigma} \tag{4.4}$$

where $\Delta\boldsymbol{\varepsilon}$ are the incremental membrane and curvature strains as shown in Eq. 4.5

$$\Delta\boldsymbol{\varepsilon} = \begin{bmatrix} \Delta\boldsymbol{\varepsilon}_m \\ \Delta\boldsymbol{\kappa} \end{bmatrix} \tag{4.5}$$

The stress resultant vectors (strains and stresses) and the equivalent scalar quantities are related through a work hardening model as shown in Eq. 4.6.

$$\boldsymbol{\sigma}^T d\boldsymbol{\varepsilon} = \bar{\sigma} d\varepsilon_{pl} \tag{4.6}$$

where $\bar{\sigma} = \sqrt{\boldsymbol{\sigma}^T \mathbf{A} \boldsymbol{\sigma}}$. Using the yield criterion on the form in Eq. 4.2, the flow rule from Eq. 4.4 and the work hardening model from Eq. 4.6, the equivalent plastic strain increment can be expressed as

$$d\varepsilon_{pl} = 2 d\lambda \bar{\sigma} \tag{4.7}$$

A power law hardening model for the material is used:

$$\bar{\sigma} = \sigma_0 \left(\frac{\bar{\varepsilon}}{\varepsilon_0} + 1 \right)^n \tag{4.8}$$

where $\sigma_0 = E\varepsilon_0$ and n is the hardening exponent ($0 \leq n \leq 1$). The expression for the updated stress following the elastic predictor and plastic corrector approach reads

$$\boldsymbol{\sigma}_{n+1} = \boldsymbol{\sigma}_{trial} - \mathbf{C} \Delta\boldsymbol{\varepsilon}_{pl,n+1} \tag{4.9}$$

Reorganising Eq. 4.9 and substituting $\Delta\boldsymbol{\varepsilon}_{pl,n+1}$ with the result from the flow rule in Eq. 4.4, the expression for the updated stress level is

$$\boldsymbol{\sigma}_{n+1} = \left[\mathbf{I} + 2\Delta\lambda_{n+1} \mathbf{C}\mathbf{A} \right] \boldsymbol{\sigma}_{trial} \tag{4.10}$$

Now the yield criterion from Eq. 4.2 only depends on $\Delta\lambda$. Using a Newton-Raphson iteration scheme, the non-linear function $f(\Delta\lambda_{n+1})$ can be solved to update the stresses. The consistent material tangent stiffness matrix in the integration point now reads

$$d\boldsymbol{\sigma} = \left[\mathbf{D} - \frac{\mathbf{D}\mathbf{g}\mathbf{g}^T\mathbf{D}}{\mathbf{g}^T\mathbf{D}\mathbf{g} + \gamma} \right] d\boldsymbol{\varepsilon} = \mathbf{C}_{ct} d\boldsymbol{\varepsilon} \tag{4.11}$$

$$\gamma = \frac{2\alpha\bar{\sigma}}{1 - \alpha\dfrac{\Delta\lambda}{\bar{\sigma}}} \quad , \quad \alpha = \frac{2H}{\sigma_0^2}\left(\sigma_0 + H\varepsilon_{pl,n+1}\right) \quad , \quad \mathbf{g} = 2\mathbf{A}\boldsymbol{\sigma}$$

$$\mathbf{D}^{-1} = \mathbf{C}^{-1} + 2\Delta\lambda\mathbf{A} \tag{4.12}$$

The consistent tangent stiffness matrix in Eq. 4.12 is transmitted back to the main program to solve the equation system.

Chapter 5

Cyclic plasticity - kinematic hardening

For cyclic plastic loading, a kinematic hardening model must be used to capture the Bauschinger effect for reversed loading. Isotropic hardening is not capable of capturing this effect. The Bauschinger effect is normally associated with conditions where the yield strength of a metal decreases when the direction of strain is changed. For kinematic hardening models this is inherited in the models while it is not the case for isotropic hardening.

For kinematic hardening models, the shape and the size of the yield surface is kept constant while the back stress defines the vector between the centre of the moving yield surface and the centre of the initial yield surface configuration. Kinematic hardening models can be divided into three distinct groups - single surface models, two-surface models and multi-surface models. Examples of single surface models are Prager and Ziegler. The Prager model can lead to inconsistences when working on sub-spaces like plane stress. This was described by Ziegler [45] who presented a modification of the Prager model as a remedy for these inconsistences. The Prager and Ziegler translation rules are shown in Fig. 5.1a.

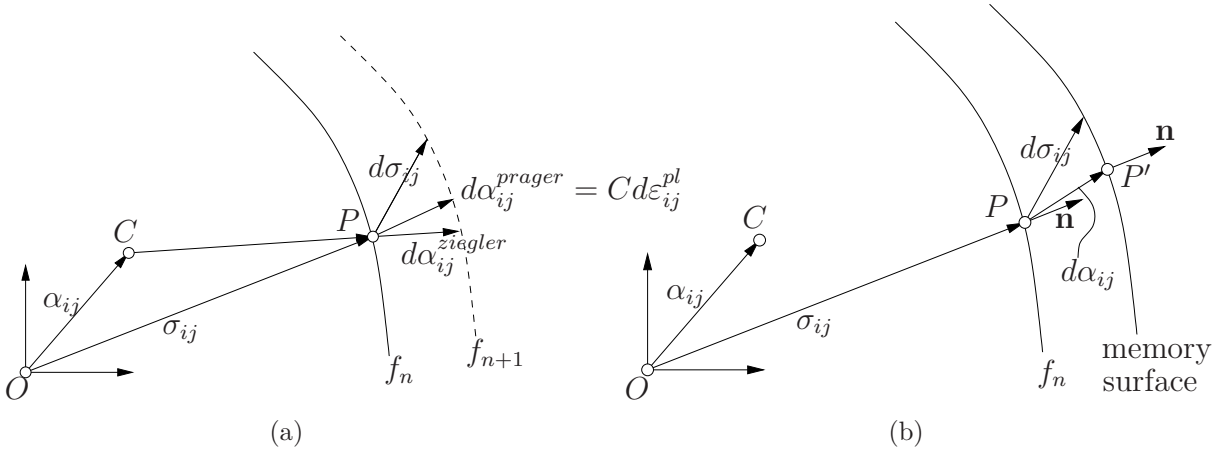

Figure 5.1: Translation rules for the (a) Prager and Ziegler model and (b) Mróz model

It is seen in Fig. 5.1a that the Prager model assumes the yield surface is moving in the direction of the plastic strains, ε_{ij}^{pl}. The Ziegler model assumes the yield surface is moving in the direction

of the vector $\sigma_{ij} - \alpha_{ij}$ (CP in Fig. 5.1a). The point C is the centre of the yield surface. α_{ij} is the back stress tensor and σ_{ij} is the stress tensor.

Dual surface models have one active yield surface and one bounding or memory surface. Examples of dual surface models are Dafalias-Popov [8], Tseng-Lee [42] and Mróz [22]. The active yield surface defines the elastic domain. The bounding surface or memory surface behaves different for different models. The Mróz translation rule is shown in Fig. 5.1b. The yield surface translates along the direction $P - P'$. Point P' on the memory surface has the same direction as the normal vector in point P on the active surface, f_n.

One approach is to let the active and memory surface be identical for the initial configuration. When the structure is loaded, the active surface translates and the memory surface is expanded isotropically. The size of the memory surface represents the maximum stress level in the loading history. The maximum stress level will not increase until the active surface comes into contact with the memory surface. The active surface will always be located inside the memory surface and will be attached to the memory surface as long as the maximum stress level is increasing. When the load is reversed, the two yield surfaces are detached. This approach together with the Mróz translation rule is used in the Tseng-Lee model.

The Dafalias-Popov model is similar to the Tseng-Lee model, but the bounding surface can also translate when the active surface is attached to it. When the two surfaces attach, both surfaces become active when further loading occurs.

A family of kinematic hardening models with increased popularity is the multi surface models. These models are capable of describing an arbitrary load history for a pointwise stress-strain curve. The number of yield surfaces equals the number of points on the stress-strain curve. The most outer surface defines the plastic domain assuming the stress-strain curve is perfectly plastic after the last point on the curve. Recent implementations of this method is presented by several authors, e.g. Caminero and Montáns [6], Khoei and Jamali [15] and Owolabi and Singh [29].

Chapter 6

Summary of papers

Two-parameter fracture assessment of surface cracked cylindrical shells during collapse
B. Skallerud, E. Berg, K. R. Jayadevan
Engineering Fracture Mechanics, **73**(2):264–282, 2006.

The competition between global and local failure modes are presented. Global failure mode is here defined as buckling of pipes subjected to a global bending moment. The local failure mode is a surface crack subjected to unstable crack growth. For the pipes subjected to pure tensile loading, unstable crack growth was the only failure mode occurring. When the pipes subjected to bending loading buckles, the crack tip opening displacement saturates.

Two-parameter fracture mechanics and circumferential crack growth in surface cracked pipelines using line-spring elements
E. Berg, B. Skallerud, C. Thaulow
Engineering Fracture Mechanics, **75**(1):17–30, 2008.

A numerical study of circumferential crack growth in surface cracked pipes was carried out from ABAQUS analyses performed by Sandvik et al. [34]. The effect was implemented and used in the study. Also a normalisation of the ductile crack growth using the T-stress as constraint parameter was carried out on single edge notched tension and pipe subjected to tensile loading.

Ultimate fracture capacity of pressurised pipes with defects comparisons of large scale testing and numerical simulations
E. Berg, E. Østby, C. Thaulow, B. Skallerud
Engineering Fracture Mechanics, **75**(8):2352–2366, 2008.

This paper presents a validation of the implementations where numerical results are compared with large scale experimental data. Both the local failure mode of ductile crack growth and the global failure mode of local buckling occurs and is captured in the numerical analyses. The effects of wall thickness and yield stress is also investigated. The effect of internal pressure was studied both in the experiments and in the numerical analyses.

Cyclic plasticity modelling behaviour of ANDES thin shell and line-spring finite elements
E. Berg, K. Holthe, B. Skallerud
International Journal of Applied Mechanics, **1**(1):201–232, 2009.

A new methodology to account for cyclic plastic response in the thin shell ANDES and line-spring finite elements is presented. The Ziegler kinematic translation rule is used in the shell element. In the line-spring element an alternative translation rule based on the Ziegler rule is used. Comparisons between the numerical simulations and large scale a experiment of pipe subjected to cyclic bending loading and "tearing fatigue crack growth" are presented.

Conference proceedings

Direct calculations, 2-parameter fracture mechanics and ductile crack growth
E. Berg, B. Skallerud, C. Thaulow, K. Holthe, K. R. Jayadevan
17. Nordic Seminar on Computational Mechanics, Stockholm, Sweden, 2004.

Using constraint correction to ductile crack growth in surface cracked shell-structures
E. Berg, B. Skallerud, C. Thaulow, K. Holthe
MekIT'05, Trondheim, Norway, 2005.

An integrated approach to analysis of surface cracked shells subject to instabilities
B. Skallerud, E. Berg
International Conference on Computational Methods in Marine Engineering, Oslo, Norway, 2005.

Ductile fracture of pipelines - effects of constraint correction and circumferential crack growth
E. Berg, B. Skallerud, C. Thaulow, K. Holthe
17. International Offshore and Polar Engineering Conference, Lisbon, Portugal, 2007.

Surface and embedded cracks in offshore pipelines subjected to plastic strains
E. Berg, B. Skallerud, K. Holthe
6. International Conference on Computation of Shell and Spatial Structures, Ithaca, New York, USA, 2008.

Chapter 7

Conclusions and suggestions for further work

7.1 Conclusions

Two failure modes interplay in this study - local and global failure mode. The local failure mode represents the ductile crack growth. The global failure mode is ovalisation or buckling.

For a pipe subjected to pure bending with an internal pressure, buckling is not likely to occur for the geometries studied herein. The internal pressure prevents the cross section from ovalisation due to the hoop stress. For a pipe subjected to pure bending and no internal pressure, the pipe suffers from local buckling. When the pipe buckles, the crack growth saturates, i.e. the ductile tearing stops. For pipes subjected to tensile loading, the internal pressure will not change the failure mode.

Ductile crack growth in the thickness direction also gives a contribution to crack growth in the circumferential direction. The magnitude of the circumferential crack growth seems to be approximately equal the initial ligament size. A non-linear function was established to quantify the circumferential crack growth.

Analyses comparing the line-spring model with large scale experiments of pipes subjected to a monotonic bending loading with or without internal pressure are carried out with very good agreement. Both the global and local failure modes were captured.

A non-linear kinematic hardening material model based on the Ziegler translation rule was implemented for both the shell and line-spring finite elements. The line-spring yield surface consists of points connected by line segments. The stress-strain curve is also pointwise with line segments between the points. Comparisons for different load cases was carried out with promising results. Ductile tearing for a pipe subjected to cyclic bending loading was also presented with good agreement.

Hence, the combination of shell and line-spring finite elements proves to be an efficient and accurate approach in order to predict complex fracture models in pipe line structures.

7.2 Suggestions for further work

The work in this thesis is mainly focusing on the installation phase for a pipeline where the largest plastic deformations are most likely to occur. The operational phase covers the main part of the lifetime of a pipe. During the operational phase, the pipe is subjected to a fatigue situation due to wave induced stresses, shut-offs and start-ups and other loads and situations occurring.

Low and high cycle fatigue is a very central task for future work. Cyclic plasticity for both the shell element and the line-spring element is presented in the thesis, which opens up for fatigue analyses. To be able to perform reliable fatigue analyses an enhanced study of the cyclic ΔK_I solutions must be carried out in order to see the effect of the crack geometry and loading conditions.

Material mismatch is also of high interest. Material mismatch is present where two or more materials meet. For a pipeline, material mismatch occurs where two pipe segments are welded together. The present implementation assumes that the weld is rectangular (a real weld is trapezoidal rather than rectangular) and the width is wider than the cracked ligament. This limits the use of studying material mismatch with the present formulation. Improvements in the line-spring formulation to account for a more general mismatch situation would increase the applicability of the line-spring methodology.

The current implementation assumes that the crack is located in a homogeneous material. This prevents the possibility of having the crack on the fusion line where two materials meet. A decomposition of the line-spring element for the cases where the crack is on the fusion line, or any material intersection, can be a potential approach.

Misalignment occurs where pipe segments are welded together. Since these welds occur about every 6 meters, the amount of positions with misalignment along a pipeline is quite significant. This is a well known phenomenon, but the fracture mechanical response and detailed understanding of the effects are still immature. A decomposition similar to the suggestion for mismatch can be a potential approach for the line-spring element also for misalignmenfor misalignment.

Bibliography

[1] R. A. Ainsworth and N. P. O'Dowd. A framework for including constraint effects in the failure assessment diagram approach for fracture assessment. *In: Proceedings of ASME Pressure Vessels and Piping Conference, PVP-vol.287/MD-vol. 47*, 1994.

[2] T. L. Anderson. *Fracture mechanics - Fundamentals and Applications*. Taylor and Francis, 2005. ISBN: 978-0-8493-1656-2.

[3] E. Berg, B. Skallerud, C. Thaulow, and K. Holthe. Using constraint correction to ductile crack growth in surface cracked shell-structures. *In proceedings: MekIT'05 Computational Mechanics, Trondheim, Norway. ISBN: 82-519-2052-3.*, pages 75–85, 2005.

[4] C. Betegon and J. W. Hancock. Two parameter caracterization of elastic-plastic crack-tip fields. *Journal of Applied Mechanics*, 58:104–110, 1991.

[5] British Standard. BS7910:1999: Incorporating Amendment No. 1. Guide on methods for assessing the acceptability of flaws in metallic structures. *British Standards Institute*, 2000. Skriv inn tekst her.

[6] M. Á. Caminero and F. J. Montáns. An enhanced algorithm for nested surfaces plasticity using the implicit Mróz translation rule. *Computers and Structures*, 84:1684–1695, 2006.

[7] M. Chiesa, B. Skallerud, and D. Gross. Closed form line spring yield surfaces for deep and shallow cracks: formulation and numerical performance. *Computers and Structures*, 80:533–545, 2002.

[8] Y. F. Dafalias and E. P. Popov. Cyclic loading for materials with a vanishing elastic region. *Nuclear Engineering and Design*, 41:293–302, 1977.

[9] Z. Z. Du and J. W. Hancock. The effect of non-singular stresses on crack-tip constraint. *Journal of the Mechanics and Physics of Solids*, 39:555–567, 1991.

[10] C. A. Felippa and C. Militello. Membrane triangles with corner drilling freedoms: II. The ANDES element. *Finite Elements in Analysis and Design*, 12:189–201, 1992.

[11] J. W. Hancock, W. G. Reuter, and D. M. Parks. Constraint and toughness parametrized by: T-stress. *American Society for Testing and Materials, Philadelphia*, 1171:21–40, 1993.

[12] Ibrahimbegovic A. and Frey F. Stress resultant elasto-plastic analysis of plates and shallow shells. *In proceedings: COMPLAS-3, Barcelona, Spain*, pages 2047–2059, 1992.

[13] K. R. Jayadevan, E. Berg, C. Thaulow, E. Østby, and B. Skallerud. Numerical investigation of ductile tearing in surface cracked pipes using line-springs. *International Journal of Solids and Structures*, 43:2378–2397, 2006.

[14] K. R. Jayadevan, C. Thaulow, E. Østby, E. Berg, B. Skallerud, K. Holthe, and B. Nyhus. Structural integrity of pipelines: T-stress by line-spring. *Fatigue and Fracture of Engineering Materials and Structures*, 28:467–488, 2005.

[15] A. R. Khoei and N. Jamali. On the implementation of a multi-surface kinematic hardening plasticity and its applications. *International Journal of Plasticity*, 21:1741–1770, 2005.

[16] S. G. Larsson and A. J. Carlsson. Influence of non-singular stress terms and specimen geometry on small-scale yielding at crack tips in elastic-plastic materials. *Journal of the Mechanics and Physics of Solids*, 21:263–277, 1973.

[17] H. Lee and D. M. Parks. Enhanced elastic-plastic line-spring finite element. *International Journal of Solids and Structures*, 32(16):2393–2418, 1995.

[18] H. Lee and D. M. Parks. Line-spring finite element for fully plastic crack growth-I. Formulation and one-dimensional results. *International Journal of Solids and Structures*, 35:5115–5138, 1998.

[19] H. Lee and D. M. Parks. Line-spring finite element for fully plastic crack growth-II. Surface cracked plates and pipes. *International Journal of Solids and Structures*, 35:5139–5158, 1998.

[20] H. Matthies. A decomposition method for integration of elastic-plastic rate problem. *International Journal for Numerical Methods in Engineering*, 28:1–11, 1989.

[21] F. A. McClintock, Y.-J. Kim, and D. M. Parks. Tests for fully plastic fracture mechanics of plane strain mode I crack growth. *Constraint Effects in Fracture: Theory and Applications*, ASTM STP 1256:199–222, 1995.

[22] Z. Mróz. On the description of anisotropic workhardening. *Journal of the Mechanics and Physics of Solids*, 15:163–175, 1967.

[23] B. Nyhus, M.P. Loria, and O.L. Ørjasæter. SENT specimens an alternative to SENB specimens for fracture mechanics testing of pipelines. *Proceedings of OMAE2003, 22nd International Conference of Offshore Mechanics and arctic engineering, Cancun, Mexico*, 2003.

[24] B. Nyhus, Z.L. Zhang, and C. Thaulow. Normalisation of material crack resistance curves by the T-stress. *Proceedings of the 14th European Conference of Fracture, Poland*, 2002.

[25] N. P. O'Dowd and C. F. Shih. Family of crack-tip fields characterized by a triaxiality parameter - I. Structure of fields. *Journal of the Mechanics and Physics of Solids*, 39:989–1015, 1991.

[26] N. P. O'Dowd and C. F. Shih. Family of crack-tip fields characterized by a triaxiality parameter - II. Fracture applications. *Journal of the Mechanics and Physics of Solids*, 40:939–963, 1992.

[27] E. Østby. Fracture control-offshore pipelines - new strain-based fracture mechanics equations including the effect of biaxial loading, mismatch, and misalignment. *Proceeding of OMAE2005, 24th International Conference on Offshore Mechanics and Arctic Engineering. Halkidiki, Greece*, 2005.

[28] E. Østby and A. O. Hellesvik. Fracture control – offshore pipelines jip, results from large scale testing of the effect of biaxial loading on the strain capacity of pipes with defects. *Submitted to ISOPE 2007. Paper. No. ISOPE-2007-SBD-31*, 2007.

[29] G. M. Owolabi and M. N. K. Singh. Extension of a multi-surface plasticity model to two-phase materials. *International Journal of Solids and Structures*, 44:1086–1098, 2007.

[30] D. M. Parks. The inelastic line-spring: estimates of elastic-plastic fracture mechanics parameters for surface cracked plates and shells. *Journal of Pressure Vessel Technology*, 103:246–254, 1981.

[31] J. R. Rice. A path independent integral and the approximate analysis of strain concentration by notches and cracks. *Journal of Applied Mechanics*, 35:379–386, 1968.

[32] J.R. Rice. The line spring model for surface flaws. *Swedlow, J.L. (Ed.), The Surface Crack: Physical Problems and Computational Solutions. American Society of Mechanical Engineers, New York*, pages 171–185, 1972.

[33] J.R. Rice and N. Levy. The part-through surface crack in an elastic plate. *Journal of Applied Mechanics*, 39:185–194, 1972.

[34] A. Sandvik, E. Østby, and C. Thaulow. A probabilistic fracture mechanics model including 3D ductile tearing of bi-axially loaded pipes with surface cracks. *Accepted by Engineering Fracture Mechanics*, 2007.

[35] T.L. Sham. The determination of the elastic T-stress using higher order weight functions. *International Journal of Fracture*, 48:81–102, 1991.

[36] C. F. Shih. Relationships between the J-integral and the crack opening displacement for stationary and extending cracks. *Journal of the Mechanics and Physics of Solids*, 29(4):305–326, 1981.

[37] B. Skallerud. A mixed mode I/II inelastic line spring. *International Journal of Solids and Structures*, 33(28):4143–4166, 1996.

[38] B. Skallerud and B. Haugen. Collapse of thin shell structures - stress resultant plasticity modelling within a co-rotated ANDES finite element formulation. *International Journal for Numerical Methods in Engineering*, 46:1961–1986, 1999.

[39] B. Skallerud, K. Holthe, and B. Haugen. Thin shell and surface crack finite elements for simulation of combined failure modes. *Computer Methods in Applied Mechanics and Engineering*, 194(21-24):2619–2640, 2005.

[40] H. Tada, P.C. Paris, and G.R. Irwin. The stress analysis of cracks handbook. *Fracture Proof Design, Saint Louis, Montana, USA*, 1985.

[41] C. Thaulow, E. Østby, B. Nyhus, Z. L. Zhang, and B. Skallerud. Constraint correction of high strength steel. selection of test specimens and application of direct calculations. *Engineering Fracture Mechanics*, 71:2417–2433, 2004.

[42] N. T. Tseng and G. C. Lee. Simple plasticity model of two-surface type. *Journal of Engineering Materials*, 109:795–810, 1983.

[43] Y.-Y. Wang and D. M. Parks. Evaluation of the elastic T-stress in surface-cracked plates using the line-spring method. *International Journal of Fracture*, 56:25–40, 1992.

[44] C. S. White and D. M. Parks. Elastic-plastic line-spring finite elements for surface-cracked plates and shells. *Journal of Pressure Vessel Technology*, 104:287–292, 1982.

[45] H. Ziegler. A modification of Prager's hardening rule. *Quarterly of Applied Mechanics*, 17:55–65, 1959.

PAPER I

Two-parameter fracture assessment of surface cracked cylindrical shells during collapse.

B. Skallerud, E. Berg, K. R. Jayadevan

Engineering Fracture Mechanics **73**(2):264–282, 2006.

Two-parameter fracture assessment of surface cracked cylindrical shells during collapse

B. Skallerud[1], E. Berg[1], K. R. Jayadevan[2]

[1]Department of Structural Engineering, Norwegian University of Science and Technology, N-7491 Trondheim, Norway
[2]Dep. Mechanical Engineering, Government Engineering College, Thrissur, Kerala, India

ABSTRACT

The present study addresses the use of CTOD and T-stress in fracture assessments of surface cracked shell structures. A new software is developed for this purpose, denoted LINK$_{pipe}$. It is based on a combination of a quadrilateral assumed natural deviatoric strain thin shell finite element and an improved line-spring finite element. Plasticity is accounted for using stress resultants. A power law hardening model is used for shell and line-spring materials. A co-rotational formulation is employed to represent nonlinear geometry effects. With this, one can carry out nonlinear fracture mechanics assessments in structures that show instabilities due buckling (local/global), ovalisation and large rigid body motion. Many constraint-measuring parameters have been proposed, with the Q-parameter or the T-stress being the most popular ones. Solid finite element meshing for complex structures such as pipes containing semi-elliptical surface cracks in order to compute Q is at present not a feasible approach. However, shell structures are most conveniently meshed with shell finite elements, and the line-spring finite element is a natural way of accounting for surface cracks. The T-stress is readily obtained from the line-spring membrane force and bending moment along the surface crack. In this study we present a new approach to analyse cracked shell structures subjected to large geometric changes. By numerical examples it is shown how geometric instabilities and fracture compete as governing failure mode.

Keywords: plasticity; large rotations; co-rotated formulation; assumed strain thin shell finite element; line-spring finite element; nonlinear fracture mechanics; ductile crack growth

1 Introduction

Surface cracked shell structures occur in many industrial applications, e.g. pressure vessels, pipelines, tubular joints etc. In the present study offshore pipelines for oil and gas transportation have a special focus. Such tubular structures are subjected to many challenging load cases. A very convenient method for pipe laying is reeling. Then the pipeline is continuously un-winded from a spool. During this sequence significant inelastic straining due to high bending evolves. As pipe segments are joined by girth welds, some defects have to be expected and assessed with respect to fracture. Furthermore, free spans for seabed pipelines pose challenging fatigue life calculations due to vortex induced vibrations. External and/or internal pressure also needs to be accounted for. An important point in fracture assessment of pipelines is that the stresses in the shell are mainly of membrane type (tension or compression), even for a pipe subjected to global bending moments. This lowers the constraint in the plastic zone at the crack tip in comparison to the constraint in shells with high local bending moments. It is well known that reduced constraint of the plastic zone in front of the crack tip provides higher fracture toughness than in a high constraint situation. And in many structural applications the low constraint condition is the actual one. Using a fracture toughness based on high constraint test specimens then results in overly conservative capacity of the structure. Put in other words, the low measured toughness in combination with traditional capacity checks may lead to an assessment that does not allow for any cracks or defects at all in a component subjected to high loading. This is unacceptable for welded structures, where some defects have to be expected. A methodology to account for reduced constraint is proposed by Chiesa et al. [7], where a single edge notched tensile specimen is employed as fracture test specimen instead of the usual (high constraint) three point bend specimen.

Traditionally, three-dimensional solid finite elements are employed in discretising the shell structure in order to account for the crack. This puts high demands on both pre- and post-processing in addition to long CPU times. An alternative is to use shell finite elements. Then the challenge is to account for the crack. This may be done using line-spring finite elements at the crack location. A factor of 10 in reduced CPU is typical. But the main benefit of using shell/line-spring elements is the reduced time spent in pre- and post-processing. Using line-springs, the crack is modelled as nonlinear springs between the shell elements, with a varying compliance as a function of crack depth and plastic deformations. A complicating factor in the shell fracture assessment is the fact that large global motion and local instabilities due to local buckling may occur. So it is an interplay between nonlinear geometry effects and the crack driving forces, Skallerud [27]. This is accounted for in the present simulations, providing answer to whether geometrical or fracture mechanical instabilities governs the shell capacity.

The present study addresses the use of CTOD, T-stress, and ductile tearing curves in fracture assessments of surface cracked shell structures using tailored software denoted LINK$_{pipe}$[17]. It is based on a co-rotated kinematical formulation using quadrilateral thin shell and line-spring finite elements. The shell element is a non-conforming high performance finite element based on assumed natural deviatoric strains, denoted ANDES. It was originally developed by Felippa and Militello [9], and further extended for use in large rotation inelastic analyses by Skallerud and Haugen [28]. The line-spring formulation was derived for elastic materials by Rice and Levy

[25]. Elasto-plasticity was incorporated by Parks and White [24]. Closed form yield surfaces also valid for the short crack regime were developed by Chiesa et al [8] and are employed herein. Some additional yield surface refinements are included in the current version of the software. A detailed presentation of numerical aspects and implementation is given by Skallerud et al [29]. Validation of the software, comparing with detailed 3D solid finite element analyses using ABAQUS, is provided in [29, 14, 13].

The first part of the paper addresses some of the theory behind the shell and line-spring formulations, and two-parameter fracture mechanics. Then numerical test cases are presented. Here both elastic and elastic-plastic response and crack tip stress fields are addressed. Finally, some cases including both nonlinear geometry effects (local buckling) and ductile fracture are presented, with focus on the interplay between large displacements and response of surface cracks.

2 Theoretical basis

2.1 Shell finite element, kinematics, and elasto-plasticity

The derivations for the co-rotated ANDES finite element are rather lengthy. A detailed account is provided by Skallerud and Haugen [28]. In the following the basic relationships are presented. The 4-node ANDES shell element is developed as a flat element with decoupled membrane and bending behaviour, and has 6 degrees of freedom at each node (i.e. also a drilling dof that contributes to membrane deformations). It is based on a combination of finite element technologies from the free formulation and assumed natural strains, see [4, 19, 2, 22] and references therein. The element stiffness for the ANDES element is the sum of a basic and higher order stiffness contribution. The basic stiffness is derived from a constant stress in the element doing virtual work on element boundary displacements described in terms of the visible degrees of freedom $\mathbf{v}$:

$$\mathbf{Kv} = (\mathbf{K_b} + \mathbf{K_h})\mathbf{v} = \mathbf{f} \tag{1}$$

$$\mathbf{K_b} = \frac{1}{V}\mathbf{L}\mathbf{C_e}\mathbf{L^T}, \qquad \int_{\mathbf{S}} \delta\mathbf{d^T}\bar{\boldsymbol{\sigma}}_\mathbf{n}\mathbf{dS} = \delta\mathbf{v^T}\int_{\mathbf{S}} \mathbf{N_d^T}\mathbf{T_n}\mathbf{dS}\bar{\boldsymbol{\sigma}} = \delta\mathbf{v^T}\mathbf{L}\bar{\boldsymbol{\sigma}} \tag{2}$$

Here $\bar{\boldsymbol{\sigma}}, \mathbf{d}, \mathbf{L}$ are the constant stress, element boundary displacements, and nodal lumping matrix, respectively. With this approach, the individual element test of Bergan and Hanssen [3] is satisfied (i.e. a strong form of the patch test that provides convergence for mesh refinement). The higher order stiffness may be derived in many ways, e.g. via the free formulation, assumed natural strain, or assumed natural deviatoric strain (ANDES). The latter is used herein, with local (invisible) dof for bending from natural curvature interpolation along the element sides and diagonals linked to curvature degrees of freedom at each node, and from natural membrane strains along element sides and diagonals linked to membrane strain dofs at each node. The

higher order stiffness may be expressed by

$$\mathbf{K}_h = \beta \mathbf{Q}^T \mathbf{K}_d \mathbf{Q} \qquad \mathbf{K}_d = \int_V \mathbf{A}_d^T \mathbf{C}_e \mathbf{A}_d dV \tag{3}$$

$$\varepsilon = \mathbf{A}\mathbf{g} = \mathbf{A}\mathbf{Q}\mathbf{v} = (\bar{\mathbf{A}} + \mathbf{A_d})\mathbf{Q}\mathbf{v} \tag{4}$$

Here $\mathbf{A}$ is the interpolation matrix for assumed strains, $\bar{\mathbf{A}} = (1/V)\int_V \mathbf{A} dV$ provides the average assumed strain, hence $\mathbf{A}_d$ is the interpolation matrix for the deviatoric part. The nodal strain dof $\mathbf{g}$ (membrane and curvature) are linked to the visible dof by $\mathbf{Q}$. β is a scaling factor that may be used to optimise the finite element performance.

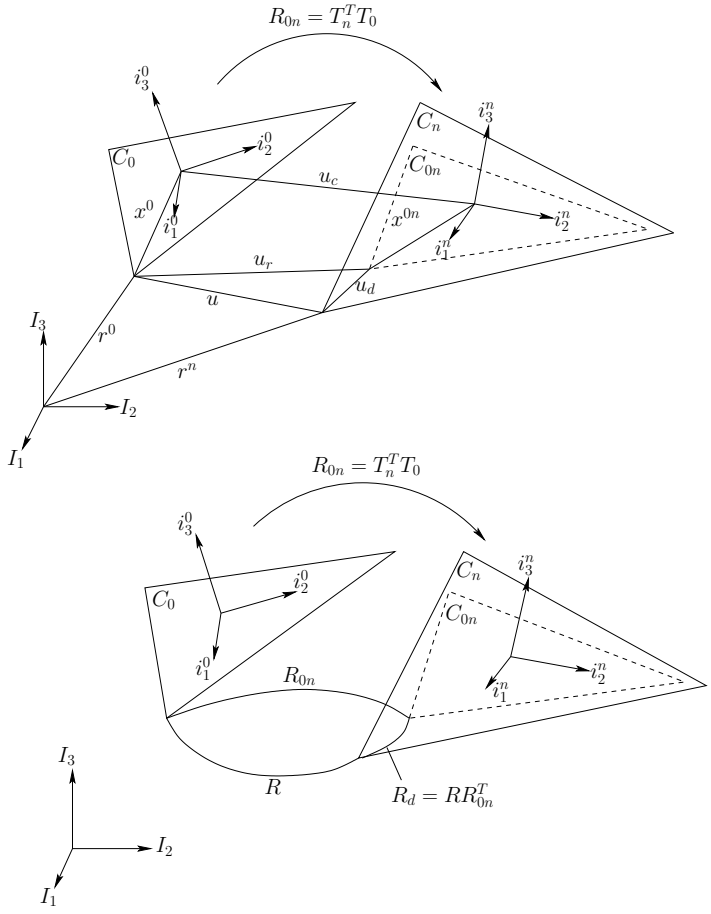

Figure 1: Co-rotated thin shell kinematics (a triangular element is used for illustration)

The co-rotated finite element formulation is convenient in that it gives a stringent way of filtering out rigid body translations and rotations, and the strain and curvature producing deformations at element level are obtained. Assuming small strains at element level gives the possibility to utilise any kind of shell finite element for linear problems in geometrical nonlinear problems. Fig. 1 shows the two basic coordinate systems that are used. The global coordinate system is represented by unit vectors $\mathbf{I}_1$, $\mathbf{I}_2$ and $\mathbf{I}_3$. The co-rotated element coordinate system shared by shadow configuration C_{0n} and configuration C_n is represented by unit vectors $\mathbf{i}_1^n$, $\mathbf{i}_2^n$ and $\mathbf{i}_3^n$. Vectors given in the local element coordinate system are marked with a tilde(˜). A

vector $\mathbf{x}$ in global coordinates is transformed into a vector $\tilde{\mathbf{x}}$ in the local coordinate system *0* by

$$\tilde{\mathbf{x}} = \mathbf{T}_0\mathbf{x} \qquad \mathbf{T}_0 = \begin{bmatrix} \mathbf{i}_1^{0T} \\ \mathbf{i}_2^{0T} \\ \mathbf{i}_3^{0T} \end{bmatrix} \tag{5}$$

$\mathbf{T}_0$ is orthonormal. The rigid body rotation of $\mathbf{i}_i^0$ to $\mathbf{i}_i^n$ is given by

$$\mathbf{i}_i^n = \mathbf{R}_{0n}\mathbf{i}_i^0 \qquad \mathbf{R}_{0n} = \mathbf{T}_n^T\mathbf{T}_0 \tag{6}$$

where $\mathbf{R}_{0n}$ is the rigid body rotation matrix from position *0* to position *n*. The Rodrigues representation of the rotation matrix is used. The rotation matrix for a rotation θ about an axis defined by the unit vector $\mathbf{n}^T = \begin{bmatrix} n_1 & n_2 & n_3 \end{bmatrix}$ is written (see Argyris [1]):

$$\mathbf{R} = \mathbf{I} + \mathbf{N}\sin\theta + \mathbf{N}^2(1 - \cos\theta) \tag{7}$$

$$\mathbf{N} = \mathbf{Spin}(\mathbf{n}) = \begin{bmatrix} 0 & -n_3 & n_2 \\ n_3 & 0 & -n_1 \\ -n_2 & n_1 & 0 \end{bmatrix}$$

$\mathbf{I}$ is the 3 by 3 identity matrix. Rotation of a vector $\mathbf{r}_0$ into $\mathbf{r}$ through an angle θ about an axis defined by the unit vector $\mathbf{n}$ is obtained by:

$$\mathbf{r} = \mathbf{R}\mathbf{r}_0 \tag{8}$$

The displacement vector is given as the difference between the position vector in configuration C_0 and the position vector in configuration C_n.

$$\mathbf{u} = \mathbf{r}^n - \mathbf{r}^0 \tag{9}$$

The displacement vector is split into a deformational displacement vector and a rigid body displacement vector.

$$\mathbf{u} = \mathbf{u}_r + \mathbf{u}_d \qquad \mathbf{u}_r = \mathbf{r}^{0n} - \mathbf{r}^0 \qquad \mathbf{u}_d = \mathbf{r}^n - \mathbf{r}^{0n} \tag{10}$$

Introducing subscript c for the arithmetic mean of the coordinates of the points in the element, the position vectors in initial and shadow element configurations may be written as:

$$\begin{aligned} \mathbf{r}^0 &= \mathbf{r}_c^0 + \mathbf{x}^0 \\ \mathbf{r}^{0n} &= \mathbf{r}_c^{0n} + \mathbf{x}^{0n} = \mathbf{r}_c^0 + \mathbf{u}_c + \mathbf{R}_{0n}\mathbf{x}^0 \end{aligned} \tag{11}$$

where $\mathbf{x}^0$ and $\mathbf{x}^{0n}$ are the vectors from the centroid of the element to the point being considered in the C_0 configuration and the C_{0n} configuration respectively. Substitution of the expressions above into Eqn.10 yields:

$$\mathbf{u}_d = \mathbf{u} - \mathbf{u}_r = \mathbf{u} - (\mathbf{r}^{0n} - \mathbf{r}^0) = \mathbf{u} - \mathbf{u}_c - (\mathbf{R}_{0n} - \mathbf{I})\mathbf{x}^0 \tag{12}$$

The rotation of an element node as it moves from the initial configuration C_0 to the deformed configuration C_n is described by the rotation matrix $\mathbf{R}$. The rotation matrix is split into a rigid body rotation $\mathbf{R}_{0n}$ and a deformational rotation $\mathbf{R}_d$.

$$\mathbf{R} = \mathbf{R}_d\mathbf{R}_{0n} \tag{13}$$

$$\mathbf{R}_d = \mathbf{R}\mathbf{R}_{0n}^T = \mathbf{R}\mathbf{T}_0^T\mathbf{T}_n \tag{14}$$

The deformational rotation matrix transformed into the local coordinate system shared by configurations C_{0n} and C_n reads

$$\tilde{\mathbf{R}}_d = \mathbf{T}_n\mathbf{R}_d\mathbf{T}_n^T = \mathbf{T}_n\mathbf{R}\mathbf{T}_0^T \tag{15}$$

The position of an element node a with initial coordinates $\mathbf{r}_a^0$, is defined by the translational displacement $\mathbf{u}_a$ and the rotational orientation $\mathbf{R}_a$. Together, the set $(\mathbf{u}_a, \mathbf{R}_a)$ for $a = 1, ..N$ is the nodal displacement vector $\hat{\mathbf{v}}$. $\hat{\mathbf{v}}$ is interpreted as an array of numbers that defines the position of the deformed element. In order to establish the force vector and tangent stiffness for an element, the *deformational* vector for the element needs to be established. This vector is denoted $\tilde{\mathbf{v}}_d$ and contains translational and rotational degrees of freedom for each element node ordered as

$$\tilde{\mathbf{v}}_d^T = \left[\tilde{\mathbf{u}}_{d1}^T\tilde{\boldsymbol{\theta}}_{d1}^T \ldots \tilde{\mathbf{u}}_{dN}^T\tilde{\boldsymbol{\theta}}_{dN}^T\right] \tag{16}$$

N is the number of element nodes for the element being considered. $\tilde{\boldsymbol{\theta}}_d$ is obtained from $\tilde{\mathbf{R}}_d$.

Virtual work is employed as weak form of the equilibrium equations:

$$\begin{aligned} \delta_R\tilde{\mathbf{v}}_d^T\tilde{\mathbf{f}}_e - \delta\mathbf{v}^T\mathbf{f}_{ext} &= \delta\mathbf{v}^T\left[\left(\frac{\partial_R\mathbf{v}_d}{\partial\mathbf{v}}\right)^T\mathbf{f}_e - \mathbf{f}_{ext}\right] = 0 \\ \Rightarrow \mathbf{f}_e &= \mathbf{T}^T\tilde{\mathbf{P}}^T\tilde{\mathbf{H}}^T\tilde{\mathbf{f}}_e = \mathbf{f}_{ext} \end{aligned} \tag{17}$$

The transformations are matrices accounting for large rigid body translations and rotations, see Skallerud and Haugen [28] for details. The deformational part of nodal degrees of freedom $\delta_R\mathbf{v}_d$ (containing both displacements and rotations) may be written as

$$\delta_R\mathbf{v}_d = \mathbf{H}\left(\mathbf{I} - \mathbf{P}_T - \mathbf{P}_R\right)\delta\mathbf{v} = \mathbf{H}\mathbf{P}\delta\mathbf{v} \tag{18}$$

Matrix $\mathbf{P}$ is a nonlinear projector operator that filters out rigid body translation and rotation. $\mathbf{H}$ is a matrix that links deformational rotations and finite spatial rotations at the nodes.

The consistent tangent stiffness is obtained by the variation of the internal force vector $\mathbf{f}_e$ with respect to $\mathbf{v}$:

$$\delta\mathbf{f}_e = \frac{\partial\mathbf{f}}{\partial\mathbf{v}}\delta\mathbf{v} = \mathbf{K}_t\delta\mathbf{v} \tag{19}$$

In more detail the result reads:

$$\delta\mathbf{f} = \delta\mathbf{T}^T\tilde{\mathbf{P}}^T\tilde{\mathbf{H}}^T\tilde{\mathbf{f}}_e + \mathbf{T}^T\delta_R\tilde{\mathbf{P}}^T\tilde{\mathbf{H}}^T\tilde{\mathbf{f}}_e + \mathbf{T}^T\tilde{\mathbf{P}}^T\delta_R\tilde{\mathbf{H}}^T\tilde{\mathbf{f}}_e + \mathbf{T}^T\tilde{\mathbf{P}}^T\tilde{\mathbf{H}}^T\delta\tilde{\mathbf{f}}_e \tag{20}$$

$$= \left(\mathbf{K}_{GR} + \mathbf{K}_{GP} + \mathbf{K}_{GM} + \mathbf{K}_{MG}\right)\delta\mathbf{v} = \mathbf{K}_T\delta\mathbf{v} \tag{21}$$

The different terms of the tangent stiffness represent rotational geometric stiffness, projection geometric stiffness, moment correction geometric stiffness, and material stiffness, respectively. The rotational geometric stiffness arises from the variation of the transformation matrix between initial configuration C_0 and shadow configuration C_n. As a rigid rotation of a stressed element rotates the stresses, the internal forces change direction to preserve equilibrium. The equilibrium projection geometric stiffness arises from the variation of the projector matrix $\tilde{\mathbf{P}}^T$,

and reflects the variation of the force vector due to variations in the degrees of freedom. The moment correction geometric stiffness arises from variation of $\tilde{\mathbf{H}}$.

$\tilde{\mathbf{K}}_e$ represents the material stiffness for the element, and may include plasticity effects. It connects the local deformational dof increment with the local force increment:

$$\delta\tilde{\mathbf{f}}_e = \tilde{\mathbf{K}}_e \delta_R \tilde{\mathbf{v}}_d \tag{22}$$

A stress resultants yield criterion based on Ilyushin [12] is employed for the shell element. For thin shells of materials with plastic yielding governed by the Mises yield criterion, the Ilyushin criterion works well. Denoting the integration point stress resultant vector by $\boldsymbol{\sigma} = [\tilde{\boldsymbol{n}}, \tilde{\boldsymbol{m}}]^T$ the isotropic yield criterion is rewritten in quadratic form (see Matthies [18] and Ibrahimbegovic [11]:

$$\begin{aligned} f &= \boldsymbol{\sigma}^T \boldsymbol{A} \boldsymbol{\sigma} - \left(1 + \frac{H\varepsilon_p}{\sigma_y}\right)^2 = 0 \\ \boldsymbol{A} &= \begin{bmatrix} \frac{1}{n_0^2}\bar{\boldsymbol{A}} & \frac{\xi}{2\sqrt{3}m_0 n_0}\bar{\boldsymbol{A}} \\ \frac{\xi}{2\sqrt{3}m_0 n_0}\bar{\boldsymbol{A}} & \frac{1}{m_0^2}\bar{\boldsymbol{A}} \end{bmatrix} \qquad \bar{\boldsymbol{A}} = \begin{bmatrix} 1 & -0.5 & 0 \\ -0.5 & 1 & 0 \\ 0 & 0 & 3 \end{bmatrix} \\ m_0 &= 0.25\sigma_y t^2, n_0 = \sigma_y t, \xi = \pm 1 \end{aligned} \tag{23}$$

The stress resultant vector $\boldsymbol{\sigma}$ and the differential plastic strain vector $d\boldsymbol{\varepsilon}_p$ are related to the equivalent stress and equivalent plastic strain increment by the relation

$$\boldsymbol{\sigma}^T d\boldsymbol{\varepsilon}_p = \bar{\sigma} d\bar{\varepsilon_p} \Rightarrow d\bar{\varepsilon_p} = 2\bar{\sigma} d\lambda \qquad \bar{\sigma} = \sqrt{\boldsymbol{\sigma}^T \boldsymbol{A} \boldsymbol{\sigma}} \tag{24}$$

The following power law work hardening model is employed:

$$\bar{\sigma} = \sigma_y \left(\frac{\bar{\varepsilon_p}}{\varepsilon_y} + 1\right)^n \tag{25}$$

where $\sigma_y = E\varepsilon_y$ and n is the hardening exponent ($0 \leq n < 1$). Utilising an associated flow rule, the backward Euler update of the plastic strain increment reads

$$\Delta\boldsymbol{\varepsilon}_{p,n+1} = \Delta\lambda_{n+1} \frac{\partial f}{\partial \boldsymbol{\sigma}}_{n+1} \qquad \Delta\boldsymbol{\varepsilon} = [\Delta\boldsymbol{\varepsilon}_m, \Delta\boldsymbol{\kappa}]^T \tag{26}$$

The discrete yield condition f_{n+1} now depends only on $\Delta\lambda$. Solving for $f(\Delta\lambda_{n+1})$ (Newton-Raphson) the stress update is obtained. The consistent material tangent for an integration point reads:

$$\begin{aligned} d\boldsymbol{\sigma} &= \left[\boldsymbol{C} - \frac{\boldsymbol{C}\boldsymbol{g}\boldsymbol{g}^T\boldsymbol{C}}{\boldsymbol{g}^T\boldsymbol{C}\boldsymbol{g} + \gamma}\right] d\boldsymbol{\varepsilon} = \boldsymbol{C}_t d\boldsymbol{\varepsilon} \\ \gamma &= \frac{2\alpha\bar{\sigma}}{1 - \alpha\frac{\Delta\lambda}{\bar{\sigma}}} \qquad \alpha = \frac{2H}{\sigma_y^2}(\sigma_y + H\varepsilon_{p,n+1}) \\ \boldsymbol{C}^{-1} &= \boldsymbol{C}_e^{-1} + 2\Delta\lambda\boldsymbol{A} \qquad \boldsymbol{g} = 2\boldsymbol{A}\boldsymbol{\sigma} \end{aligned} \tag{27}$$

2.2 line-spring finite element

The part-through surface crack is originally a three dimensional problem. The three dimensional problem is formulated within the context of two-dimensional plate or shell theory with the part-cracked section represented as a line-spring. The line-springs take into account the additional flexibility due to the surface crack. The line-spring element can be schematically represented by two straight lines connected to each other by a series of springs. At zero deformation the lines lie upon each other. When a Mode I (crack opening) deformation takes place each line displaces in opposite direction. The displacement and rotation are constrained by the springs. As the shell element used herein is 4-noded, the line-spring element is 4-noded with linear interpolation polynomials. A 2-point Gauss integration is employed. Hence, the line-spring element has 8 degrees of freedom (four in-plane displacements and four rotations with axis along the element).

Defining τ_0 as shear yield stress, t shell thickness, and using normalised membrane force and bending moment per length, $\bar{Q}_1 = \frac{N}{2\tau_0 t}, \bar{Q}_2 = \frac{M}{\tau_0 t^2}$, the general yield surfaces ϕ governing the plastic behaviour of cracked shell section ligament reads:

$$\phi = \begin{cases} \phi_{df} & : \quad \bar{Q}_1 \geq \bar{Q}_2 \tan(\frac{\pi}{2} + \alpha) \\ \phi^s_{df} & : \quad \bar{Q}_1 < \bar{Q}_2 \tan(\frac{\pi}{2} + \alpha) \end{cases} \tag{28}$$

where ϕ_{df} is a parabolic yield surface with a validity confined mainly to the I and IV quadrants of the generalised force space. It reads:

$$\phi_{df} = A\bar{Q}_2 + B\bar{Q}_1 + C\bar{Q}_1^2 + D = 0 \tag{29}$$

see [8] for the fitting parameters A, B, C, D. The function ϕ^s_{df}, symmetric to ϕ_{df} with respect to the line $\overline{Q}_1 = tan(\frac{\pi}{2} + \alpha)\overline{Q}_2$, can be used in order to describe simplified (conservative) yielding behaviour in the II and III quadrants.

The angle α between the symmetry line and the Q_1-axis is found to be close to a linear function of the relative crack depth $\frac{a}{t}$. The fitted yield surfaces were obtained from finite element limit-load analysis results from Lee and Parks [15] (see also Chiesa et al. [8]). ϕ contains more accurate information about the general yielding behaviour of shallow, as well as deep cracks, for the single edge cracked (SEC) specimen than the typically employed yield surfaces. Work hardening is employed in order to connect line-spring stress resultants and energy conjugate line-spring deformations with continuum plastic work in the plastified ligament:

$$dW_p = \mathbf{Q}^T d\mathbf{q}_p = \int\limits_{A_{plastic}} \sigma_{eq} d\varepsilon_{p,eq} dA = k\sigma_y \frac{d\sigma_y}{E_p} c^{n'} \tag{30}$$

Here, k is a factor of order unity, $n' = 2$, and $c = t - a$ is ligament size. Combining these equations, using associated flow rule and consistency condition, the line-spring tangent stiffness is obtained.

Ductile tearing is accounted for using CTOD versus Δa curves as input (either obtained from tests or numerical simulations using Gurson based models). Hence, the crack growth reduces

ligament size with consequence that the line-spring yield surfaces shrink accordingly. The line-spring stiffness matrix is modified at the start of the increment, based on CTOD at the previous increment. See Jayadevan et al. [13] for details.

Both a forward and backward Euler line-spring force update method for the line-spring element are implemented in LINK$_{pipe}$. In the present simulations the forward difference was employed, see Skallerud et al. [29] for a discussion.

3 Fracture assessment methods

Many constraint-measuring parameters have been proposed, with the Q-parameter or the T-stress being the most popular ones (see O'Dowd and Shih [21] and Parks [23]). Q measures the difference of the crack tip stress field in a real specimen with respect to a reference stress field such as HRR. T is the first non-singular term in the Williams power series expansion for the stress component normal to the crack front. As such it is valid for elastic material behaviour or small scale yielding, and is feasible for ranking the constraint level in brittle fracture cases. Q is valid for larger amounts of plastic deformations, and may be considered as a more general measure of constraint than the T-stress. But Parks [23] and Betegon and Hancock [5] have shown that T can also be applied up to load levels causing yielding of the ligament. A two-parameter fracture assessment approach is illustrated in Fig. 2. Here a failure locus is obtained from tests on specimens of different constraint levels, and when the computed driving force and corresponding constraint reaches the failure locus, fracture mechanical failure occurs.

In some studies the extended use of elastic T-stress under large-scale plasticity has been investigated (Betegon and Hancock [5] and Hancock [10]). In these studies, the T-stress is computed from the known elastic biaxiality parameter ($\beta = T\sqrt{\pi a}/K$), which is a constant for the given geometry and loading. However, under large-scale yielding, the mode of near-tip loading (and hence, the constraint level) in a specimen will change with deformation. As the T-stress estimate from line-spring is based on the local membrane and bending components, it provides the computation of an "elastic-plastic" T-stress taking into consideration the current near-tip loading modes. Under large-scale yielding, this "elastic-plastic" T-stress from line-spring model is expected to give a better constraint estimate than the one derived from elastic biaxiality parameter.

Discretising cracked structures (e.g. pipes containing semi-elliptical surface cracks) using solid finite elements in order to compute Q (and to some extent T) is at present not a feasible approach. However, shell structures are most conveniently meshed with shell finite elements, and the line-spring finite element is a natural way of accounting for surface cracks. The T-stress is readily obtained from the line-spring membrane force N and bending moment M along the crack using relationships derived by Sham [26], and further refined by Lee and Parks [16]:

$$T(s) = (N(s)/t)t_N(a(s)/t) + (6M(s)/t^2)t_M(a(s)/t) \tag{31}$$

Here t_N and t_M are polynomial relationships depending on ratio of crack depth to shell thickness, s is the coordinate along the crack front. Note that when the line-spring enters the elastic-plastic

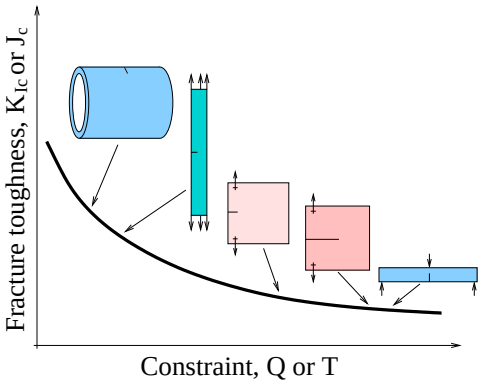

Figure 2: Two-parameter fracture assessment, failure locus.

regime, N and M moves along the yield surface due to plastic deformations and redistribution of shell stresses. In the subsequent calculations of T, Eq. 30 is employed for this situation also. The deformation output from the line-spring calculations is relative Mode I displacement $\Delta\delta$ and rotation $\Delta\theta$. These quantities are split into elastic and plastic contributions. The crack driving force J as well as crack-tip opening displacement δ_{CTOD} is divided into elastic and plastic parts, J^e and J^p and δ^e_{CTOD} and δ^p_{CTOD} . Using the relation between K_I and elastic J-integral the elastic part of crack tip opening is obtained from $J_e = K_I^2/E(1-\nu^2)$. ASTM 1290 suggests that the elastic part of CTOD of a hardening material in plane strain small-scale yielding conditions can be estimated as

$$\delta^e_{CTOD} = \frac{J^e}{m\,\sigma_o} \tag{32}$$

where m is a scalar. In ASTM E 1290, a value of 2.0 for m is suggested. The increment in plastic CTOD is obtained from the plastic line-spring deformation increments. The plastic part of CTOD is related to the plastic parts of the line-spring displacement (δ^p) and rotation (θ^p) in incremental form as

$$\Delta\delta^p_{CTOD} = C_1(Q_i, \sigma_y, a/t)\,\Delta\delta^p + C_2(Q_i, \sigma_y, a/t)\,t\,\Delta\theta^p \tag{33}$$

where the dimensionless functions C_i, are discussed by Lee and Parks [16].

4 Numerical simulations

4.1 T-stress

Results for T-stress and K_I published in the literature are mainly for surface cracked plates. Still results for surface cracked pipes are scant. Table 1 and 2 give some results for pipes with outer diameter to thickness ratio 20, having a crack width 5% and 50% of circumference and crack depth 5% or 50% of shell thickness. For the 3D simulations ABAQUS was employed.

The results are in good correspondence. Jayadevan et al [13] provides more results and a T-stress compendium for surface cracked pipes. Fig. 3b shows the T-stress normalised with K

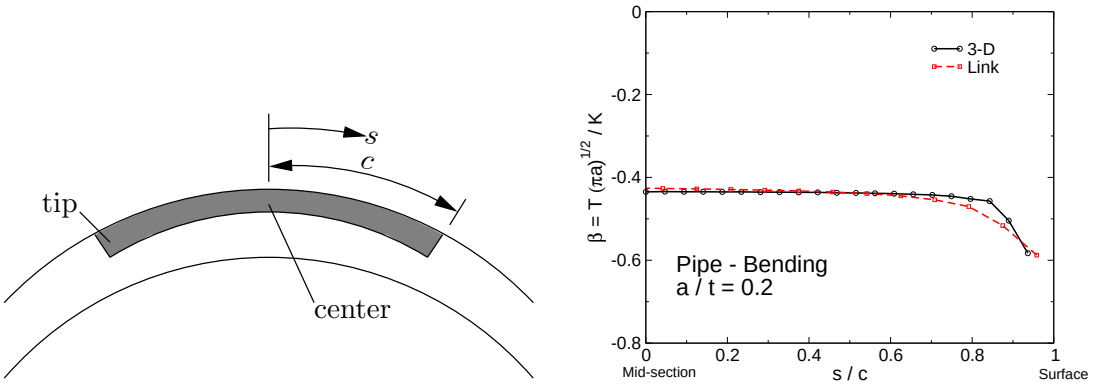

(a) (b)

Figure 3: (a) Crack geometry and notation and (b) normalised T along crack.

Table 1: A comparison of (a) normalised stress intensity factors and (b) T-stress corresponding to different a/t ratios from 3-D and line-spring simulations (with $c/\pi R = 0.05$ and $D/t = 20$) under tensile loading.

(a)

$\frac{a}{t}$	$\frac{K}{\sigma_\infty\sqrt{\pi a}}$	
	3D	LS
0.05	1.13	1.13
0.5	1.38	1.26

(b)

$\frac{a}{t}$	$\frac{T}{\sigma_\infty}$	
	3D	LS
0.05	-0.53	-0.56
0.5	-0.65	-0.73

Table 2: A comparison of (a) normalised stress intensity factors and (b) T-stress corresponding to different crack length ratios $c/\pi R$ from 3-D and line-spring simulations (with $c/\pi R = 0.5$ and $D/t = 20$) under tensile loading.

(a)

$\frac{a}{t}$	$\frac{K}{\sigma_\infty\sqrt{\pi a}}$	
	3D	LS
0.05	1.13	1.11
0.5	1.87	1.80

(b)

$\frac{a}{t}$	$\frac{T}{\sigma_\infty}$	
	3D	LS
0.05	-0.53	-0.55
0.5	-0.70	-0.75

along the crack for a pipe subjected to global bending. Except for some deviation between the two simulations at the crack end, the correspondence is good.

Parks [23] proposed that the crack opening stresses σ_{22} (i.e., $\sigma_{\theta\theta}$ at $\theta = 0$), for power law hardening materials, in any plane perpendicular to a 3-D crack front can be characterised by

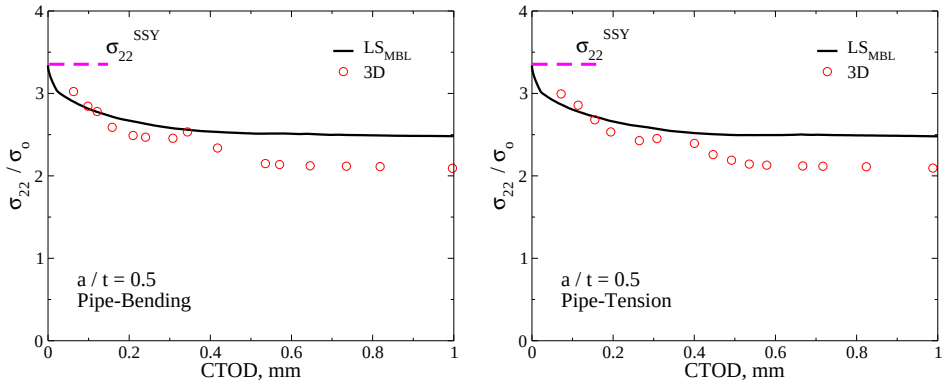

Figure 4: Comparison of stress magnitude at $r = 2J/\sigma_0$, a) pipe in bending, b)pipe in tension.

the modified boundary layer (MBL) solution,

$$\frac{\sigma_{22}^{3D}(r\sigma_o/J(\phi);\tau(\phi))}{\sigma_o} = \frac{\sigma_{22}^{ssy}(r\sigma_o/J(\phi))}{\sigma_o} + A_n\tau(\phi) + B_n\tau^2(\phi) + C_n\tau^3(\phi). \tag{34}$$

Here, in the local coordinate system (x_1, x_2, x_3), the $x_1 - x_2$ plane is perpendicular to the crack front, whereas the x_3-axis is tangential to the crack front. The local polar coordinates (r, θ) are in the plane of $x_1 - x_2$, and $\theta = 0$ when $x_2 = 0$ and $x_1 > 0$. The stress on the left hand side of Eq. 34 is the crack opening stress in a surface cracked pipe (or any structure) at crack front location ϕ and normalised distance $r\sigma_o/J$ ahead of the crack front. The right hand side of Eq. 34 is the MBL solution at the same normalised distance. In this, the first term denotes the small scale yielding (SSY) solution which can be interpreted as a particular value of the MBL solution at $\tau = 0$. The constants A_n, B_n and C_n depends upon the strain hardening exponent n of the material, and $\tau(\phi) = T(\phi)/\sigma_o$.

At a distance $r = 2J/\sigma_o$, Wang [30] fitted the MBL solution with $(A_n,\ B_n,\ C_n)$ = (0.6168, -0.5646, 0.1231) for the case of a surface cracked plate with material properties $n = 0.1$ and $\nu = 0.3$. For the above material, the analyses by O'Dowd and Shih [21] showed that $\sigma_{22}^{ssy} = 3.34\sigma_o$ at the same normalised distance. These values have been introduced in Eq. 34 along with the predicted "elastic-plastic" T-stress (modified for elastic-plastic deformation using the load history of each line-spring) from line-spring model to compare the results directly obtained from 3-D simulations.

Fig. 4 shows the opening stress evolution for increasing CTOD for a pipe in bending and tension at the distance $2J/\sigma_0$ in front of the crack tip. It is noted that the correspondence between the MBL based T-stress corrected opening stress from LINK$_{pipe}$ and the detailed 3D stress result from ABAQUS is quite good, even up to very high CTOD levels. This gives some credibility in using an "elastic-plastic" T-stress for load levels that cause full ligament yielding and beyond.

4.2 Cracked cylindrical shell in tension, stationary cracks

The cases analysed in the remaining sections are based on hardening exponent 0.1, yield stress 400MPa, elasticity modulus 200GPa, outer pipe diameter 400mm, see Fig. 5. Two D/t ratios are considered: 25 and 40. The crack depth to thickness ratios are 0.2 and 0.4, and the crack width to pipe circumference ratios are 0.05 and 0.15.

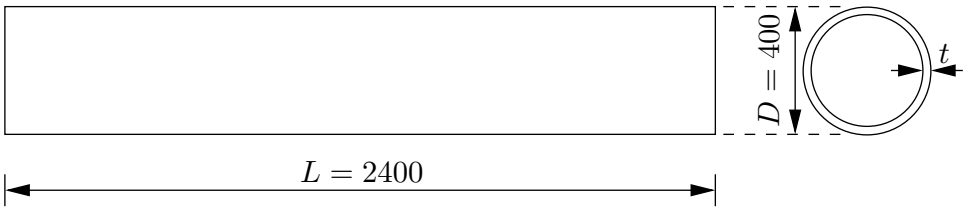

Figure 5: Tube geometry.

Fig. 6a shows the global tension load, normalised with the plastic capacity of the uncracked pipe, versus global axial elongation. It is noted that the cracks do not affect global behaviour significantly. Considering local response, Fig. 6b depicts the CTOD versus global elongation for the different crack sizes for D/t=25. Here significant effects of crack size are noted. First, it is noted that the effect of crack length is small for the shallowest crack (a/t=0.2). Second, for the deeper crack the effect of crack length is significant, showing about twice as high CTOD for the crack of width 0.15 compared to with 0.05.

One question that can be raised is whether the central section of the crack is the most critical with respect to fracture, or whether the pipe geometry and stress redistribution can transfer the most critical point out to the crack edges. This is investigated in Figs. 6c and d. Here, the legend "tip" means the centre point of the line-spring element farthest from the crack centre (see Fig. 3a). Fig. 6c shows that CTOD is always highest at centre point of the crack for c/πR=0.05. In Fig. 6d, for the deepest crack, the centre point always has a much higher CTOD than at the crack edge. But for the shallowest crack both crack locations have about the same CTOD. This is of interest in (semi-)brittle fracture, considering weakest link statistics, as a much larger part of the ligament material experiences the same local deformation.

4.3 Cracked cylindrical shell in bending, stationary cracks

Fig. 7 shows the global response of pipes subjected to bending moment at each end. The ordinate axis is bending moment normalised with respect to the plastic bending capacity of the uncracked pipe, and the abscissa axis is the maximum out-of-plane deflection at mid length of the pipe. It is observed that for both D/t ratios a limit point behaviour occur. This is due to ovalisation and local buckling instabilities, but it is noted that significant load carrying capacity is present in the post-collapse regime. As for the tension cases, the global response is marginally affected by the cracks. Considering local response, Fig. 8a, some interesting features appear. First, due to the geometrical instability (limit point), the CTOD at centre point of the crack saturates. Second, this saturation is not seen (to the same extent) at the outer part of the

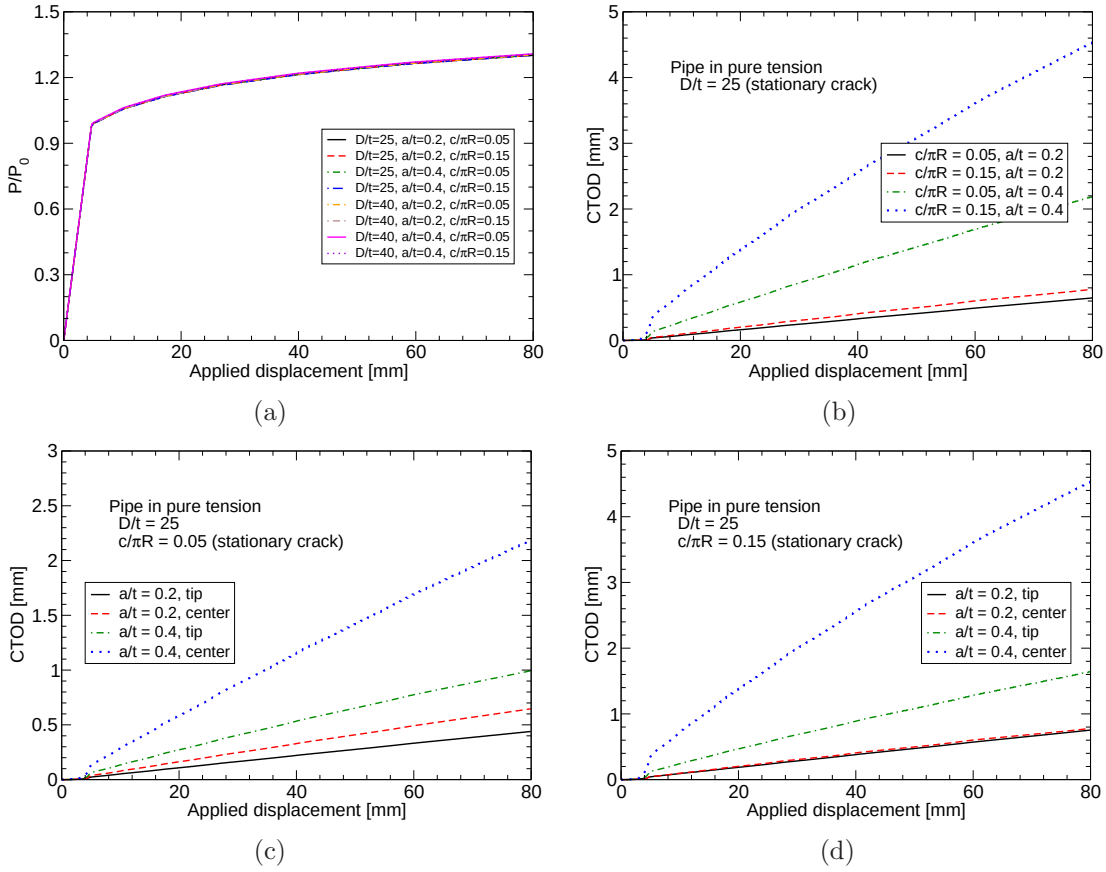

Figure 6: Pipe in tension.

crack close to the edges. So in the bending case the redistribution of stresses from centre point of crack to outer parts gives an increasing CTOD there. If one defines onset of local buckling to govern the capacity, and e.g. the material has a fracture mechanical capacity in terms of CTOD that is higher than 0.4mm, this redistribution is not critical. But if one allows for further global deformation of the pipe, the critical point of the crack is moving to outer parts of the crack, and a fracture may initiate off-centre subsequent to local buckling/ovalisation instability.

Fig 8b. shows the evolution of CTOD versus "elastic-plastic" T-stress at centre point of the crack. This plot is interesting in that although the CTOD saturates, the constraint increases after local instability. Considering the failure locus curve in Fig2, this constraint increase may increase the possibility of fracture. So in pipes subjected to global bending it is not obvious what governs the capacity (local buckling, fracture initiation at centre point, fracture inititation at end region of the crack), and numerical tools that can treat all effects in an integrated manner is necessary for a realistic capacity assessment.

4.4 Cracked cylindrical shell in tension, ductile crack growth

Now the effect of ductile tearing is investigated. Nyhus et al. [20] have shown that for a given material (and temperature), the CTOD versus crack growth curve can be normalised

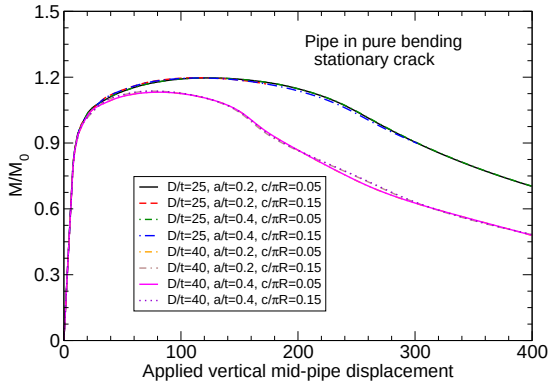

Figure 7: pipe in bending.

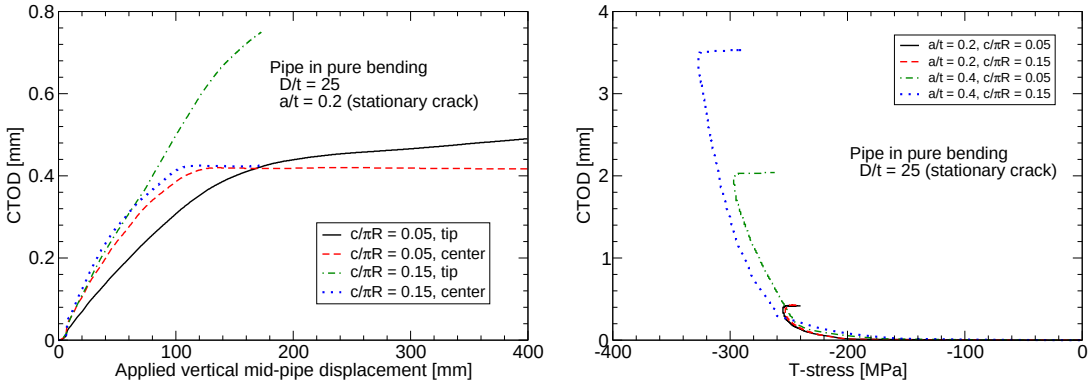

(a) (b)

Figure 8: Pipe in pure bending

with respect to geometry using the T-stress: $CTOD(\Delta a) = CTOD_{ref}(\Delta a)g(T)$. Here g is a function that is obtained from tests of different specimens or from detailed finite element computations accounting for void growth. Jayadevan et al. [13] have employed this approach using line-spring response and corresponding T-stress levels for prediction of growing cracks in surface cracked pipes. This approach is adopted herein also. Fig. 9 shows a numerically generated CTOD tearing curve for initial crack depth to thickness ratio of 0.2. The complete Gurson model as implemented in ABAQUS by Zhang et al. [32] is used. The calibration data (initial void volume fraction and crack tip finite element size) stems from the study of Chen and Lambert [6] and is representative for an X65 pipeline steel, see Jayadevan et al. [13] for more details.

Considering the effect of ductile tearing on the global tension versus elongation and bending moment versus out-of-plane displacement, it is small, and the response curves does not differ much from those given in Figs. 6a and 7. But the local response is altered significantly. Fig 10a (D/t=25, a/t=0.2) illustrates a large increase in slope of the applied CTOD (driving force) compared to assuming stationary cracks. The slope going to infinity indicates unstable crack growth. A small increase in global strain level will cause the crack to grow rapidly through the thickness of the pipe wall. For a/t=0.4, Fig. 10b, this increase happens very early in global elongation history. In Fig. 11a, considering the CTOD versus T-stress evolution, some

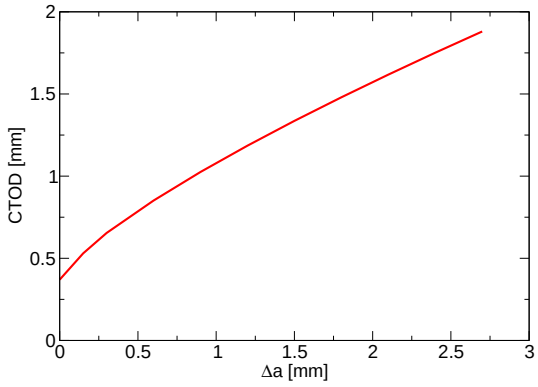

Figure 9: Ductile tearing curve based on complete Gurson simulation for the case $a_0/t = 0.2$.

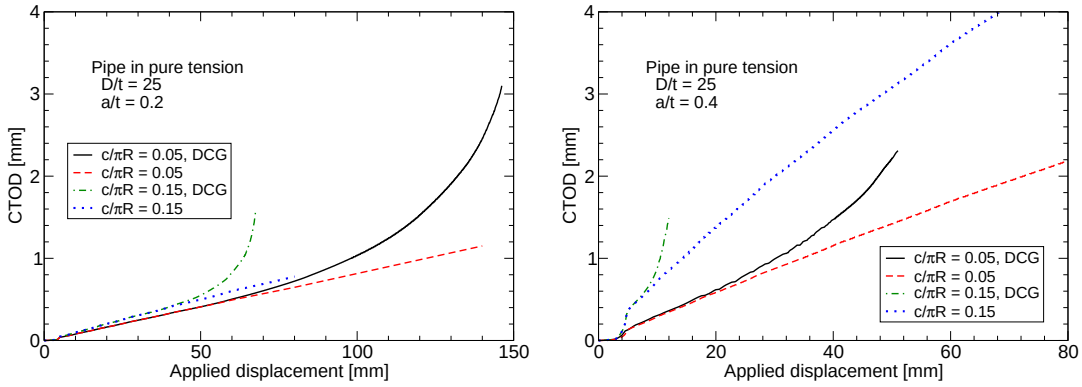

(a) (b)

Figure 10: CTOD evolution for pipe in tension, a) a/t=0.2, b) a/t=0.4 (legend DCG means simulation including ductile crack growth).

deviation between stationary cracks and ductile crack growth for cracks of initial depth a/t=0.2 is observed. The T-stress saturates at a somewhat higher level in ductile tearing compared to stationary cracks. But in Fig 11b, for a/t=0.4 initial crack depth, this trend is in the opposite direction. Note that Eq.30 was employed in the calculation of the T-stress, using the current value of crack depth, i.e. updated crack depth due to ductile crack growth.

Comparing the ductile crack growth at crack centre and end points for a pipe in tension, Fig. 11c, it is noted that the ductile crack growth is always largest at centre point. Hence, the effect of stress redistribution to the crack edges is not as important as in the stationary crack case.

4.5 Cracked cylindrical shell in bending, ductile crack growth

Fig. 12 depicts the deformed geometry of a pipe subjected to constant bending moment. On the opposite side of the buckle, the surface crack is located. Note that a somewhat finer mesh is used there in order to account for the crack. Typically ten line-spring elements were used in crack discretisation.

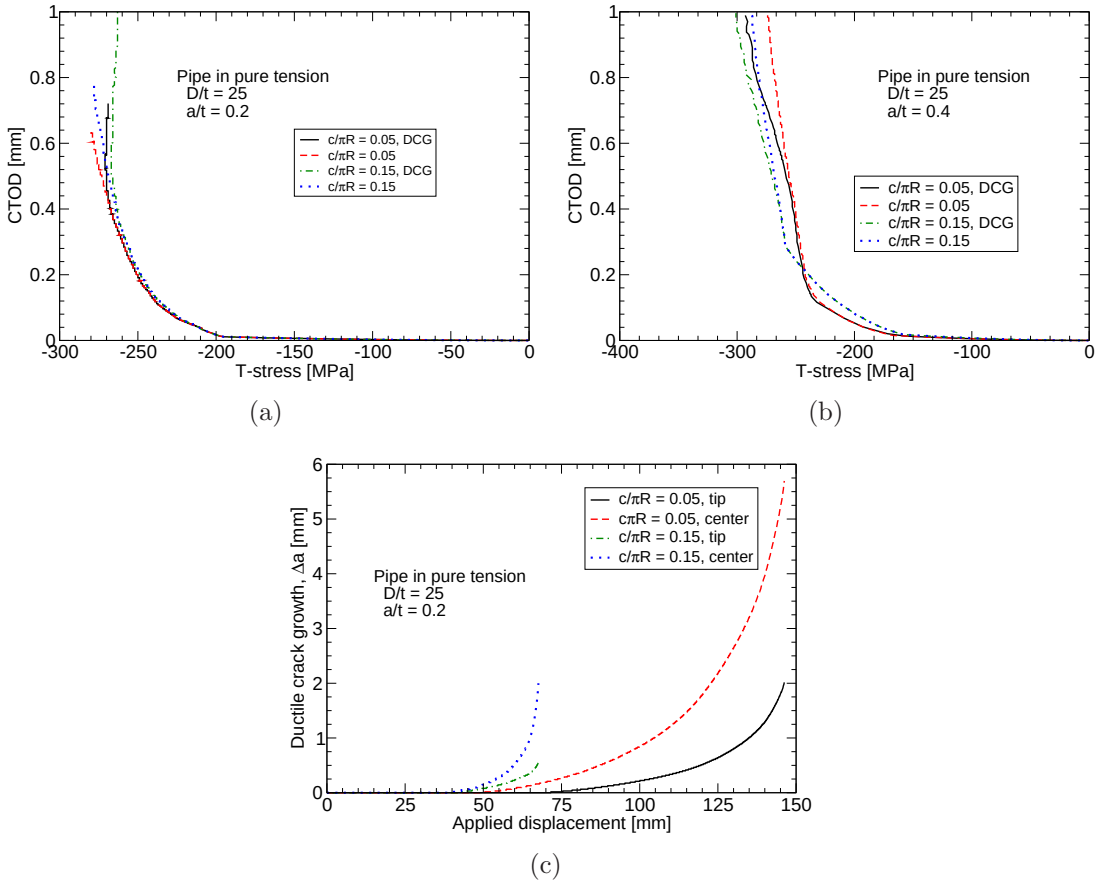

Figure 11: pipe in tension.

As can be seen in Fig.13a the global response is not affected by crack growth significantly. This is mainly because the crack area is small compared to the total load carrying area. Fig. 13b illustrates the CTOD evolution at centre point of the crack. Due to geometrical instability, CTOD saturates, and the difference from stationary cracks is small. Considering Fig. 9, the ductile crack growth starts at about 0.4mm CTOD. In Fig. 13b the CTOD reaches a level that is only slightly higher than this level, indicating that ductile crack growth hardly starts before the pipe is subject to geometrical instability, hence CTOD saturates.

The effect of ductile tearing in pipes subjected to bending is not as critical as for pipes subjected to tension. For the cases studied here the pipe ovalises and buckles right after ductile crack growth has started. This means that the global response is more critical than the local.

Figs. 13c and d depicts the CTOD versus T-stress for a pipe in bending. The saturation of CTOD is observed, the T-stress increases somewhat (as observed for stationary cracks), then followed by a decrease. But the T-stress changes are moderate.

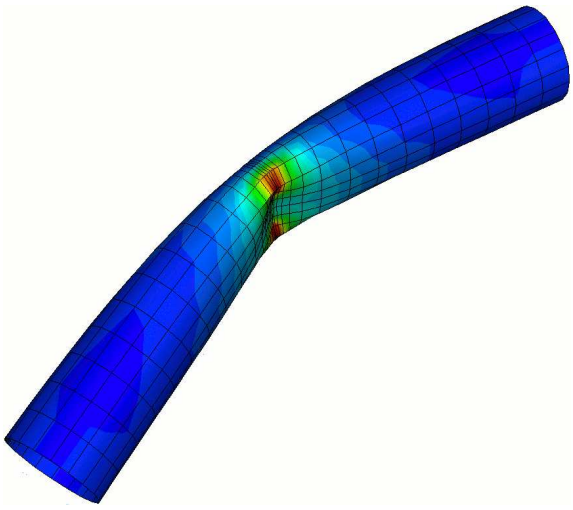

Figure 12: Buckled pipe subjected to bending

5 Concluding remarks

The present study focuses on global and local response of surface cracked pipes in global tension and constant bending. The D/t-ratios considered, 20-40, represent a quite compact cross section and a moderately slender cross section, and are in the slenderness regime often used in industrial applications. Efficient finite element modelling, using high performance thin shell and line-spring elements, was used to investigate interactions between global geometry (curved shell), nonlinear geometry (large displacements and local buckling), stress redistribution in the surface crack regions, and ductile tearing. In the bending cases significant effects of geometrical instabilities on driving force (CTOD) were observed. Typically, the CTOD saturates when local buckling occurs, at least considering the central region of the cracks. But it was shown that stress redistribution to outer parts of the crack may lead to a continuously increasing driving force there. This may transfer the critical region of the crack from the centre to edges. Furthermore, subsequent to local buckling the T-stress increases somewhat. The fracture mechanical consequence of this is not clear at present. But, even though a CTOD-saturation develops, the increased constraint may re-introduce fracture mechanical failure subsequent to local buckling. Considering ductile crack growth, the amount of ductile tearing reduces significantly if local buckling occurs. Hence, for very ductile materials, limit point behaviour may govern the capacity. In tension cases the cracks have little effect on global response. But the local response given by CTOD depends to a large amount on crack depth and length. Hence, a load based design is not very feasible. In the ductile crack growth cases, the crack growth was always largest at crack centre.

In summary, the simulations show that a capacity assessment of surface cracked pipes requires rather advanced tools in order to capture the many interactions between geometry, loading, and material. Traditional design equations as defined in standards (and mainly based on plate solutions) may be inaccurate for these geometries, and the most convenient way of assessment is obtained using direct finite element computations.

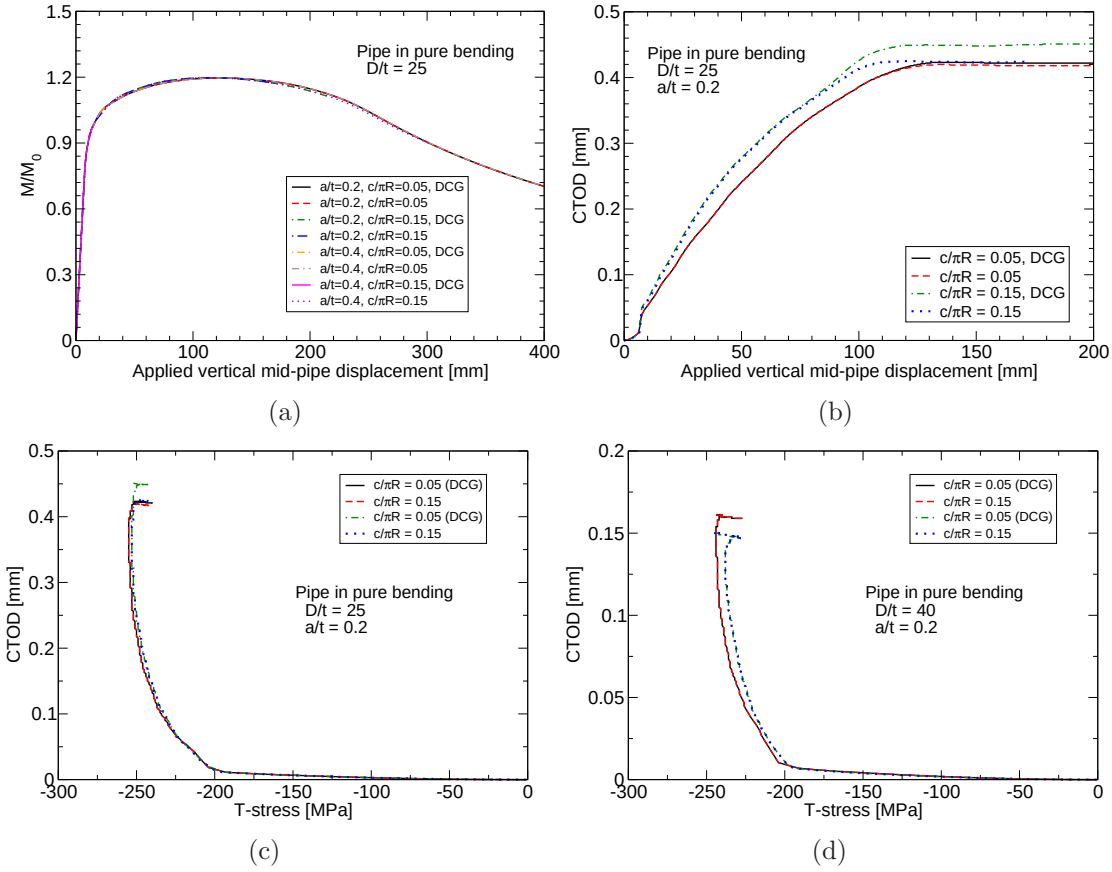

Figure 13: Pipe in bending

Acknowledgements

The authors would like to express their gratitude to Professors C. Thaulow, K. Holthe, and Dr E. Østby for helpful discussions and assistance regarding the work presented herein.

References

[1] J. H. Argyris. An Excursion into Large Rotations. *Computer Methods in Applied Mechanics and Engineering*, **32**:85–155, 1985.

[2] P. Bergan and C. A. Felippa. A triangular membrane element with rotational degrees of freedom. *Computer Methods in Applied Mechanics and Engineering*, **50**:25–69, 1985.

[3] P. Bergan and L. Hanssen. A new approach for deriving 'good' finite elements. *MAFELAP II*, Academic Press, 483-498, 1976.

[4] P. Bergan and M. Nygård. Finite elements with increased freedom in choosing shape functions. *International Journal of Numerical Methods in Engineering*, **20**:643–663, 1984.

[5] C. Betegón and J. W. Hancock. Two-parameter characterisation of elastic-plastic crack-tip fields. *Journal of Applied Mechanics*, **58**:104–110, 1991.

[6] Y. Chen and S. Lambert. Analysis of ductile tearing of pipeline-steel in single edge notch tension specimens. *International Journal of Fracture*, **124**:179–199, 2003.

[7] M. Chiesa, B. Nyhus, B. Skallerud and C. Thaulow. Efficient fracture assessment of pipelines. A constraint corrected SENT specimen approach. *Engineering Fracture Mechanics*, **68**:527–547, 2001.

[8] M. Chiesa, B. Skallerud and D. Gross. Closed form line-spring yield surfaces for deep and shallow cracks: formulation and numerical performance. *Computers and Structures*, **80**:533–545, 2002.

[9] C. A. Felippa and C. Militello. Membrane triangles with corner drilling freedoms: II. The ANDES element. *Finite Elements in Analysis & Design*,**12**:189–201, 1992.

[10] J. W. Hancock, W. G. Reuter and D. M. Parks. Constraint and Toughness Parametrized by T. *Constraint Effects in Fracture* (Edited by E. M. Hackett, K.-H. Schwalbe and R. H. Dodds Jr.), ASTM STP-1171, pp. 21–40, American Society for Testing and Materials, Philadelphia, 1993.

[11] A. Ibrahimbegovic and F. Frey. Stress resultant elasto-plastic analysis of plates and shallow shells. *COMPLAS-3*, Barcelona, pp.2047–2059, 1992.

[12] A. A. Ilyushin. *Plasticite*, Editions Eyrolles, Paris, 1956.

[13] K. R. Jayadevan, E. Berg, C. Thaulow, E. Østby, and B. Skallerud. Numerical investigation of ductile tearing in surface cracked pipes using line-spring. *International Journal of Solids and Structures*, **43**:2378–2397, 2006.

[14] K. R. Jayadevan, C. Thaulow, E. Østby, E. Berg, B. Skallerud, K. Holthe and B. Nyhus. Structural Integrity of Pipelines: T-stress by line-spring. *Fatigue & Fracture of Engineering Materials & Structures*, **28**:467–488, 2005.

[15] H. Lee and D. M. Parks. Fully plastic analysis of plane strain single edged cracked specimen subjected to combined tension and bending. *International Journal of Fracture*, **63**:329–349, 1993.

[16] H. Lee and D. M. Parks. Enhanced elastic-plastic line-spring finite element. *International Journal of Solids and Structures*, **32**:2393–2418, 1995.

[17] LINK_{pipe}Verification manual, LINKftr as, Trondheim, Norway, 2004.

[18] H. Matthies. A decomposition method for integration of elastic-plastic rate problem. *International Journal of Numerical Methods and Engineering*, **28**:1–11, 1989.

[19] C. Militello and C. A. Felippa. The first ANDES elements: 9-dof plate bending triangles. *Computer Methods in Applied Mechanics and Engineering*, **93**:217–246, 1991.

[20] B. Nyhus, Z. L. Zhang and C. Thaulow. Normalization of material crack resistance curves by the T-stress. *In: Proceedings of the 14th European Conference of Fracture*, Cracow, Poland, 2002.

[21] N. P. O'Dowd and C. F. Shih. Family of crack-tip fields characterised by a triaxiality parameter – I. Structure of fields. *Journal of the Mechanics and Physics of Solids*, **39**:989–1015, 1991.

[22] K. C. Park and G. M. Stanley. A curved C^0 shell element based on assumed natural-coordinate strains. *Journal of Applied Mechanics*, **53**:278–290, 1986.

[23] D. M. Parks. Three-dimensional aspects of HRR-dominance. *Defect Assessment in Components – Fundamentals and Applications* (Edited by J. C. Blauel and K.-H. Schwalbe), ESIS/EGF9,206-231. Mechanical Engineering Publications, London, 1991.

[24] D. M. Parks and C. S. White. Elastic-plastic line-spring finite element formulation. *Journal of Pressure Vessel Technology*, **104**:287–292, 1982.

[25] J. R. Rice and N. Levy. The part through surface crack in an elastic plate. *Journal of Applied Mechanics*, **39**:185–194, 1972.

[26] T. L. Sham. The determination of the elastic T-term using higher order weight functions. *International Journal of Fracture*, **48**:81–102, 1991.

[27] B. Skallerud. Numerical analysis of cracked inelastic shells under large deformation or mixed mode loading. *International Journal of Solids and Structures*, **56**:25–40, 1999.

[28] B. Skallerud and B. Haugen. Collapse of thin shell structures – Stress resultant plasticity modelling within a co-rotated ANDES finite element formulation. *International Journal of Numerical Methods in Engineering*, **36**:1961–1986, 1999.

[29] B. Skallerud, K. Holthe and B. Haugen. Thin shell and surface crack finite elements for simulation of combined failure modes. *Computer Methods in Applied Mechanics and Engineering*, **194**:2619–2640, 2005.

[30] Y.-Y. Wang. On the two-parameter characterization of elastic-plastic crack-front fields in surface-cracked plates. *Constraint Effects in Fracture* (Edited by E. M. Hackett, K.-H. Schwalbe and R. H. Dodds Jr.), 1993, ASTM STP-1171, 120-138, American Society for Testing and Materials, Philadelphia.

[31] Y.-Y. Wang and D. M. Parks. Evaluation of the elastic T-stress in surface-cracked plates using the line-spring method. *International Journal of Fracture*, **56**:25–40, 1992.

[32] Z. L. Zhang, C. Thaulow and J. Ødegård. A complete Gurson model based approach for ductile fracture. *Engineering Fracture Mechanics*, **67**:155–168, 2000.

PAPER II

Two-parameter fracture mechanics and circumferential crack growth in surface cracked pipelines using line-spring elements

E. Berg, B. Skallerud, C. Thaulow

Engineering Fracture Mechanics **75**(1):17–30, 2008.

Two-parameter fracture mechanics and circumferential crack growth in surface cracked pipelines using line-spring elements

E. Berg[1], B. Skallerud[1], C. Thaulow[2]

[1]Department of Structural Engineering, Norwegian University of Science and Technology, N-7491 Trondheim, Norway
[2]Department of Engineering Design and Materials, Norwegian University of Science and Technology, N-7491 Trondheim, Norway

ABSTRACT

A procedure for constraint correction of crack growth resistance curves for single edge notched specimens and for pipe geometries is presented. The procedure is based on FE models with the combination of shell- and line-spring finite elements. Crack tip opening displacement and T-stress are employed, and ductile crack growth is accounted for. Experimental crack growth resistance curves are obtained for both single edge notched tension- and bending-specimens for different crack depths to cover significantly different constraint levels. To account for different constraint levels, a method to scale the resistance curve using the T-stress is implemented. The analyses include ductile crack growth in both the circumferential and thickness directions. The effect of circumferential crack growth with biaxial loading is also presented. The results from the line-spring model are compared with detailed 3D-models for verification of the implementation of circumferential crack growth. The importance of including crack growth in circumferential direction is discussed based on numerical parametric studies. A measure to quantify the importance of circumferential crack growth is proposed.

Keywords: Fracture mechanics; Line-spring; Constraint; Two-parameter fracture mechanics; Ductile crack growth; Plasticity

1 Introduction

Over the last years, large research effort to predict the reliability of offshore pipelines with surface defects has been carried out (e.g. the joint industry project, Fracture Control Offshore Pipelines). Surface flaws might arise from weld defects in girth welds used to join pipe segments, corrosion damage etc. External forces due to impact, snaking or underwater currents could also

result in buckling which is a global failure mode. When installing offshore pipelines by reeling, the material is likely to be subjected to large scale yielding with plastic strains of the order of 2-3% in which the ductility and the crack growth resistance of the material are important challenges to manage.

The traditional pipeline design criteria used today are mainly focusing on the buckling phenomenon. The allowable strain limit on the compressive side is quite large (about 3%), but the maximum strain allowed on the tension side is very restricted, and it is on the tension side fracture mainly is a problem. The standard BS7910:2000 [5] for fracture assessment is mainly for load controlled situations. For offshore pipelines, a displacement controlled situation resulting in high plastic strains occurs, e.g during reeling. In this case, strain-based design is a more appropriate approach (see Linkens et al. [16]).

An important observation in fracture assessment of pipes is that the stresses in the pipe are mainly of membrane type even for pipes subjected to global bending as shown by Chiesa et al. [7]. This effect will lower the constraint in the near crack-tip stress field, and thereby increase the fracture toughness. This situation characterises many structural applications. Use of a high constraint single edge notched bending specimen in fracture assessments could then lead to very conservative decisions. One might reach the situation where no cracks can be tolerated. This is unacceptable for welded structures, where some defects have to be expected. A methodology to account for reduced constraint using a single edge notched tensile specimen for fracture assessment is proposed by Chiesa et al. [7], and implemented in this study.

Three dimensional solid finite element models can be employed to account for surface cracks. This approach is very time consuming with respect to pre- and post-processing in addition to long CPU times for the analysis to complete. An alternative approach would be to use a model of shell finite elements. The surface crack is modelled by introducing line-spring finite elements. This method is less time-consuming, and gives a good agreement with detailed 3D-models (Skallerud et al. [23], Jayadevan et al. [11] and Thaulow et al. [28]).

The present study addresses the use of crack tip opening displacement, T-stress and ductile crack growth in fracture assessment of surface cracked shell structures. The software used for the shell-model is the tailor-made program LINK$_{pipe}$. A detailed presentation of numerical aspects and implementation is given by Skallerud et al. [25]. It is based on on a co-rotational quadrilateral thin shell element denoted ANDES. It was originally developed by Felippa and Militello [9], and further extended by Skallerud and Haugen [24]. The line-spring formulation was proposed for elastic materials by Rice [19] and Rice and Levy [20]. It was further extended to account for elastic-plastic material by Parks and White [30]. Closed-form yield surfaces were developed by Chiesa et al. [6].

In Skallerud et al. [23], the effect of ductile tearing in thickness direction on pipe response was studied, and the crack growth in circumferential direction was neglected. In the present study, crack growth in both thickness and circumferential direction are accounted for. With this one can assess for what crack sizes it is necessary to account for circumferential ductile crack growth. The first part of the paper addresses some of the theory behind the line-spring formulation, and two-parameter fracture mechanics. The effect of circumferential crack growth for different initial crack lengths is then presented. Circumferential crack growth will be an

important effect when studying small crack lengths compared to crack depth. Then a small increase in crack length will give a significant contribution to the total crack growth. This effect is demonstrated. The final section examines the effect of using two-parameter fracture mechanics for cracks under large scale yielding. With this, one gets improved predictions of the strain capacity of the pipelines.

A comparison between the line-spring model and recent full scale testing of pipe-segments is in progress (Berg et al. [2]). One comparison is published by Thaulow et al. [28].

2 Theory

2.1 Line-spring theory

In a line-spring model, the surface crack is represented by a 2D shell structure with a through slit connected by springs. The additional compliance introduced by replacing the part-through flaw with a through-slit is accounted for line-spring elements.

When a cracked structure is analysed using the line-spring/shell model, the generalised shell resultants transmitted by the series of springs are a membrane force and a bending moment per unit length of the foundation.

The yield-surface of the line-spring element is based on tabulated values for different crack ratios published by Lee and Parks [14]. To refine the transition between the tabulated curves, analyses of additional crack ratios have been carried out to expand the table containing the tabulated yield-surfaces. The yield function is not smooth in the whole regime as corners appear where the SEN reaches maximum mid-ligament tension or compression. As seen in Fig. 1c, the corner-point location of the yield-surface can very well be fitted using a quadratic polynomial. If the $\bar{Q}_1$ (normalised membrane force) and $\bar{Q}_2$ (normalised bending moment) is plotted individually, it is seen that the $\bar{Q}_2$ follows a parabola (Fig. 1a). The $\bar{Q}_1$ (Fig. 1b) follows a linear curve. Fig. 1c shows the position of the corner-point for all crack depth ratios. Fig. 1d shows yield-surfaces for different crack depth ratios.

The Mode-I elastic-plastic behaviour of the line-spring model assumes an incremental formulation based on a simple associated flow rule with isotropic hardening. In the present line-spring model, the crack growth is fully plastic, and the crack is propagated quasi-statically based on the material tearing data. Fracture mechanic testing gives a resistance curve ($CTOD - \Delta a$) which can be treated as a material property for the given constraint-level. The accuracy of this implementation is verified and demonstrated by Jayadevan et al. [11] and Skallerud et al. [23].

2.2 2-parameter fracture assessment

It is well known that the stress field ahead of the crack tip is not only influenced by the loading conditions, but it also depends highly upon the crack geometry. This effect is called constraint. Since the crack initiation of a structure depends upon the stress field in the crack tip region,

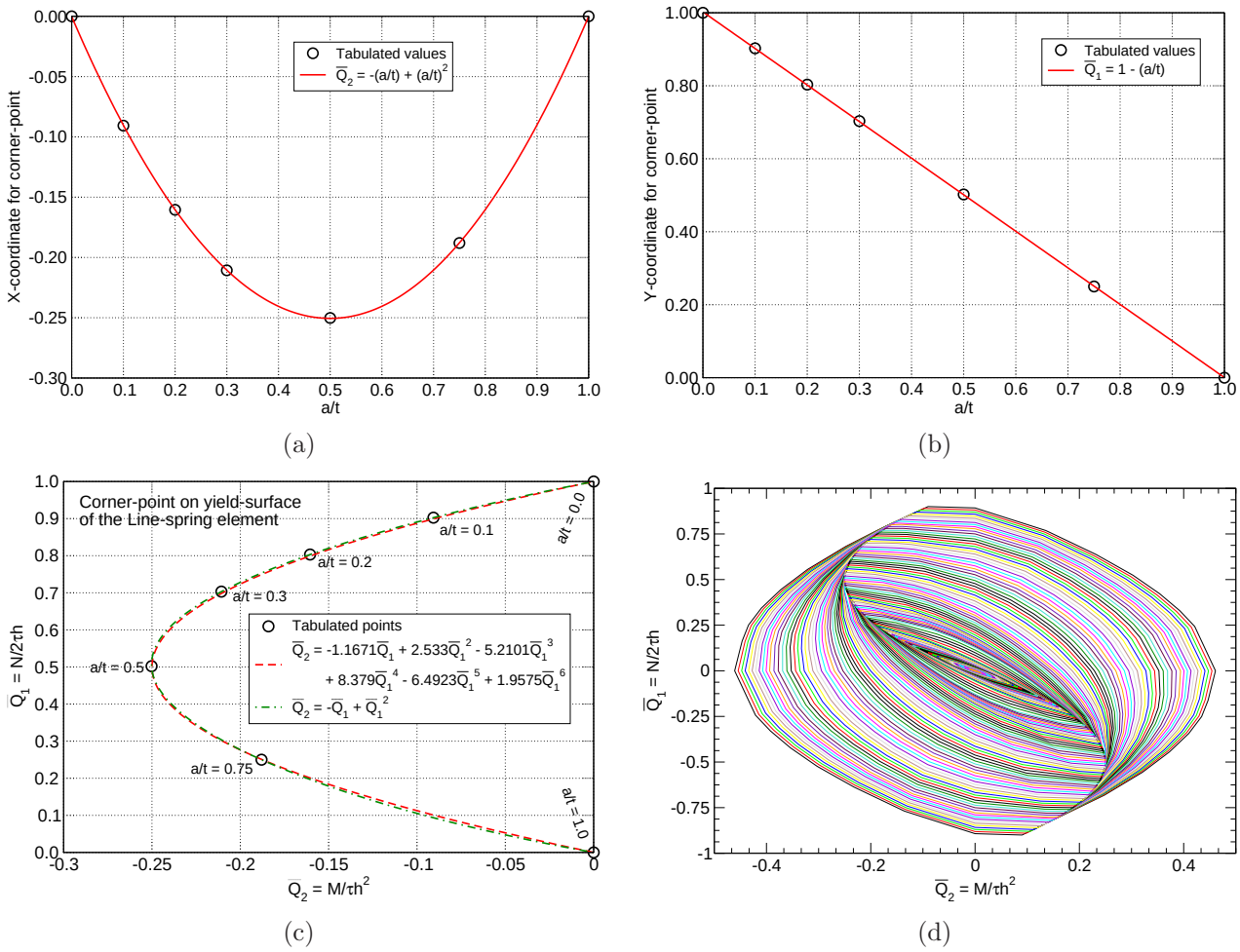

Figure 1: (a)-(c) shows the position of the corner-point of the yield-surface as functions of crack depth to thickness ratio, and (d) shows a collection of interpolated yield-surfaces for relative crack depths from $a/t = 0.1$ to 0.99.

the fracture parameters depend on the geometry as well as load. Due to this fact, the fracture toughness (K_{Ic}, J_c or $CTOD$) is not a material parameter, but also a geometry dependent parameter. The T-stress and the Q-parameter are the two most widely used approaches to measure the constraint. The T-stress is used as a constraint measurement in the subsequent analyses.

The T-stress is the first non-singular term in William's solution of the stress field (Larsson and Carlsson [13] and Du and Hancock [8]), as shown in Eq. 1. The T-stress characterises the local crack tip stress field for materials with the restriction of small-scale yielding (SSY) conditions.

$$[\sigma_{ij}] = \frac{K_I}{\sqrt{2\pi r}}\,[f_{ij}(\theta)] + \begin{bmatrix} T & 0 & 0 \\ 0 & 0 & 0 \\ 0 & 0 & \nu T \end{bmatrix} \tag{1}$$

The T-stress theory assumes that the T-stress corresponds to to elastic conditions. Most published data on the T-stress is based on plate solutions, whereas few studies are carried

out for the pipe geometry. Jayadevan et al. [12] have provided a T-stress compendium for surface cracked pipes where the Line-spring element is used. Although the T-stress is based on elastic assumptions, several studies are performed to extend the use of the T-stress under large scale plasticity. Betegon and Hancock [3] and Hancock [10] have shown the applicability of the T-stress for large scale yielding. In these studies, the T-stress is computed by employing the elastic biaxiality parameter ($\beta = T\sqrt{\pi a}/K_I$), which is a constant for a given geometry and load. In large-scale yielding conditions, the stress field surrounding the crack tip will change with deformation. The T-stress in the line-spring element is based on the local membrane force and bending moment, hence the local loading modes are taken into account when computing the "elastic-plastic" T-stress. This is expected to give a better constraint estimate compared to the one derived from the elastic biaxiality parameter (see Jayadevan et al. [12]).

To get a deeper understanding of the effect of constraint in structures, the constraint level for different standard fracture mechanics test specimens are reported by O'Dowd and Shih [18] and Thaulow et al. [27]. These data shows the fracture toughness as a function of the constraint level. This is illustrated as a two-parameter failure locus in Fig. 2. It is seen that the widely used three point bend specimen has a high constraint, which yields a low fracture toughness compared to the lower constrained tensile specimen with the same physical geometry. Crack initiation is expected to occur when the driving force cuts the failure curve. For a low constraint geometry, the intersection of the driving force curve and the experimentally derived resistance will allow for higher driving forces than for a high-constrained geometry. Hence, the need for an efficient and accurate constraint procedure arises, such as T-stress calculated by line-springs. The T-stress is computed in the Line-spring element from the membrane force, N, and the

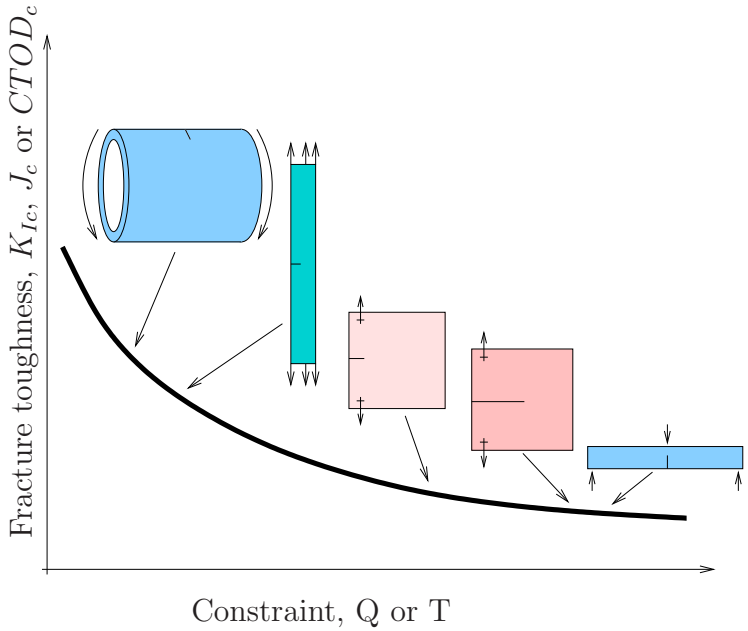

Figure 2: Two parameter fracture assessment, failure locus.

bending moment, M, along the crack using relationships derived by Sham [22], and further

refined by Lee and Parks [15] and Wang and Parks [29].

$$T(s) = \frac{N(s)}{t} t_N \left(\frac{a(s)}{t}\right) + \frac{6M(s)}{t^2} t_M \left(\frac{a(s)}{t}\right) \tag{2}$$

where the functions t_N and t_M are polynomial relationships depending on the crack ratio along the crack front. Note that when the line-spring enters the elastic-plastic regime, N and M moves along the yield-surface due to plastic deformations and redistribution of shell stresses. In the subsequent calculations of the T-stress, Eq. 2 is employed also for this situation.

2.3 Ductile crack growth

Ductile crack growth is implemented in the line-spring element. To account for ductile crack growth, the crack growth resistance curve must be applied. The curve employed herein follows the form of Eq. 3 (BS7448:4 [4]).

$$CTOD = CTOD_i + C_1(\Delta a)^{C_2} \tag{3}$$

where $CTOD_i$ is the critical CTOD-value where ductile crack growth is initiated. C_1 and C_2 are fitting constants. It is well known that the crack growth resistance curve does not uniquely characterise the material's crack growth resistance. It also depends on the current geometry and the stress triaxiality ahead of the crack tip as shown by Nyhus et al. [17]. Recent experimental crack growth data for X65 steel reported by Storslet [26] is shown in Fig. 3a. The crack growth resistance curves for two single edge notched bend specimens and one tension specimen are plotted. These results demonstrate the effect of constraint, and the crack growth resistance curve can not be treated directly as a material parameter.

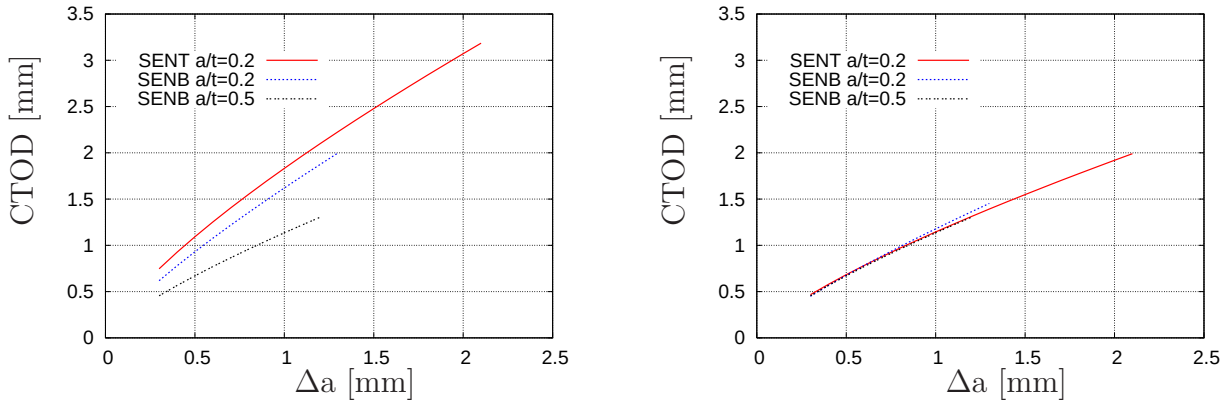

Figure 3: (a) Experimental crack growth resistance curves and (b) constraint corrected resistance curves for an X65 steel (Storslet [26]).

Nyhus et al. [17] have shown that the resistance curves can be normalised by employing the T-stress. They proposed that the resistance curves derived from different test specimens can be corrected for constraint based on a reference crack growth curve as

$$CTOD^{corr} = CTOD^{ref} g(T) \tag{4}$$

where $CTOD^{corr}$ is the constraint corrected resistance curve and $CTOD^{ref}$ is the reference curve. One of the crack growth resistance curves should be treated as the reference curve, whereas the other curves are treated as slave curves. The dimensionless function $g(T)$, after Ainsworth and O'Dowd [1], is a geometry dependent function which also may depend on the material:

$$g(T) = \begin{cases} \left[1 + \alpha \left(-\frac{T(\Delta a)}{\sigma_0}\right)^m\right]^2 & T < 0 \\ 1 & T \geq 0 \end{cases} \tag{5}$$

The parameters α and m in Eq. 5 are two material constants. Three resistance curves from different constraint levels are needed to calculate the constants. σ_0 is the yield stress. The parameters, α and m will change depending on the curve that is selected as reference curve.

It is important to note that not all crack growth resistance curves can be normalised this way. If the difference in constraint for the curves to be normalised is too small, and still the resistance curves are not overlapping, one might not be able to determine the parameters in Ainsworth's equation.

3 Numerical implementation

In a surface cracked pipe with semi-elliptical surface cracks oriented in the circumferential direction, some amount of circumferential crack growth will occur in addition to the growth in the thickness direction. This crack growth will contribute to the reduction of stiffness in the model.

One benefit of the line-spring model is that it is not necessary to do re-meshing regarding the crack growth in the thickness direction. A procedure to account for crack growth in the circumferential direction is now presented.

The circumferential crack growth is controlled by the initial crack geometry, the loading conditions and the structural geometry.

$$\Delta c = f\left(a, c, t\right) \tag{6}$$

The initial aspect ratio for the crack geometry is denoted $a/2c$, where a is the initial crack depth and $2c$ is the total initial crack length.

By the end of each time increment, the crack depth and the crack length is updated.

$$a^{(i+1)} = a^{(i)} + \Delta a^{(i)} \tag{7}$$

$$c^{(i+1)} = c^{(i)} + \Delta c^{(i)} \tag{8}$$

The quantities in Eq. 7 and Eq. 8 are shown in Fig. 4.

The four nodes at the crack ends is moved along at the end of a time increment, thus increasing the length of the end-elements. The approach is illustrated in Fig. 5. Note that in LINK_{pipe}, the line-spring element is given a small transverse extension to achieve a defined local coordinate

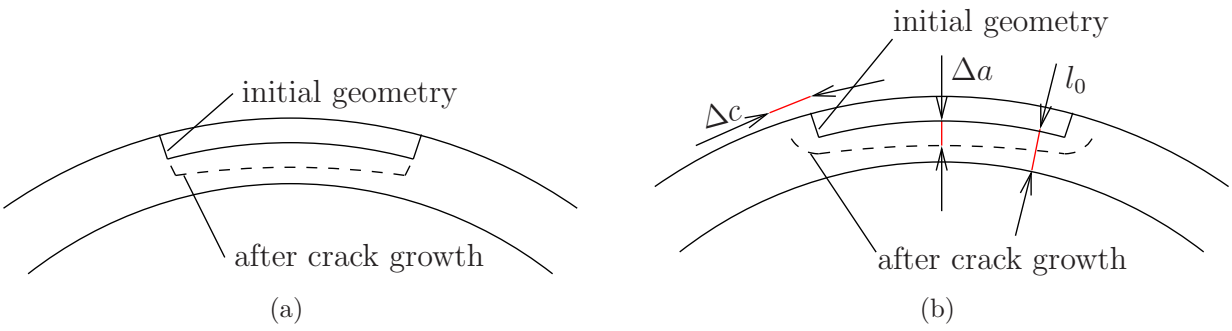

Figure 4: Crack growth behaviour of a surface crack subjected to loading. (a) gives a schematic view of the previous implementation where only crack growth in the thickness direction was accounted for, and (b) shows principles in the improved implementation of the crack growth.

system in space to fit with the co-rotated formulation. The extension in Fig. 5 is artificially large, but used here to clarify the symbols in the figure.

The method showed in Fig. 5 is based on nodal movement. The nodes at the crack ends are moved in the circumferential direction to perform ductile tearing in the circumferential direction. In this way, four nodes will be moved, thus 10 shell-elements are altered due to change in local geometry. One should note that if the circumferential crack growth is larger than (almost) the size of the neighbour shell element, a re-meshing is required. In the subsequent analyses, this was not necessary.

The abscissa axis in Fig. 6 is the ratio of crack depth (a) to the initial ligament (l), where the ordinate axis is the ratio of circumferential crack growth to initial ligament. See Fig. 4b for detailed view of the dimensions. In Fig. 6 the "+" are results from 81 3D-analyses, employing the Gurson-Tvergaard damage model (see Sandvik et al. [21] for details) of pipes subjected to various internal pressure and pure tensile loading. The dashed trend line is a best fit interpolation of the points, and this curve is implemented in LINK$_{pipe}$, i.e. defining Eq. 6.

Due to difference in crack depth along the crack front, the constraint will also have influence on the circumferential crack growth. When the crack length increases, the cracked section becomes softer compared to the global geometry, hence the crack growth at the deepest point of the crack will increase faster, resulting in modification of constraint. This effect is automatically taken into account when performing constraint correction of the crack growth resistance curve for all time increments.

4 Results and discussion

The results from the line-spring model are obtained using LINK$_{pipe}$. For the 3D-analyses, ABAQUS is employed. LINK$_{pipe}$ uses a high performance ANDES shell element along with the line-spring element, whereas the 3D-analyses are performed using C3D8-elements. The built-in Gurson-model in ABAQUS is used for the 3D-analyses. The resulting crack growth resistance curves from the 3D-analyses are used as input to LINK$_{pipe}$ for the analyses in Figs. 8-

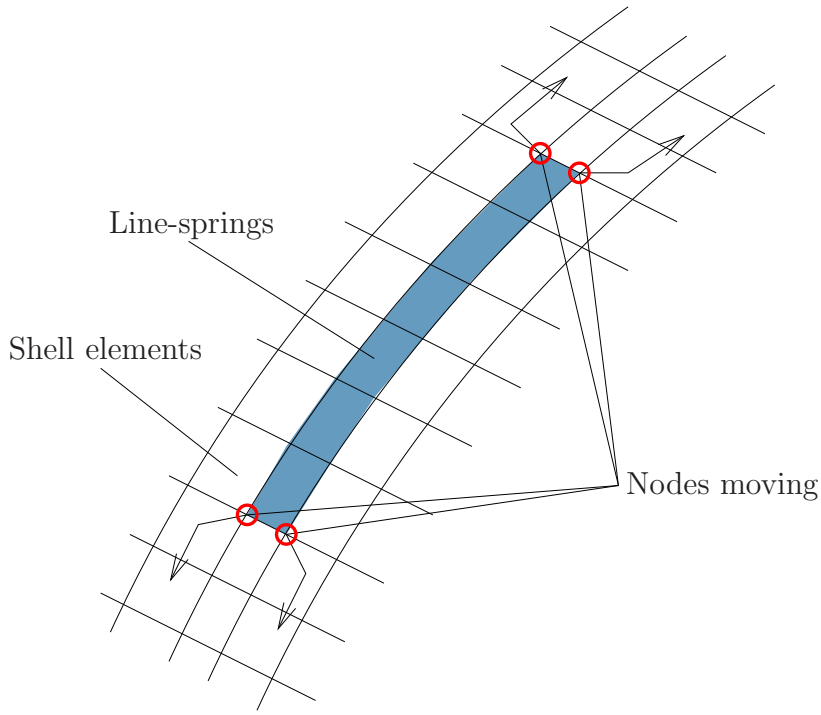

Figure 5: Schematic view of the method used to model circumferential crack growth.

10. The Gurson-parameter for initial void volume fraction used in Zybell [31] is $f_0 = 0.001$. Comparisons with full scale tests on pipes with and without internal pressure will be presented in a subsequent paper (Berg et al. [2]). The simulation results in that study compare well with the test results.

4.1 Material model

The material behaviour for this pipe is assumed to follow an isotropic non-linear hardening model according to

$$\sigma_i = \sigma_0 \left(\frac{\varepsilon_{pl}}{\varepsilon_0} + 1 \right)^n, \quad \text{for } \sigma_i > \sigma_0 \tag{9}$$

where σ_i is the flow stress, σ_0 is the initial yield stress, ε_{pl} is the plastic strain and n is the hardening exponent. The yield strain, ε_0 can be expressed as σ_0/E. The elastic-plastic material properties for the analyses carried out are $E = 200GPa$, the Poisson's ratio, $\nu = 0.3$, the yield stress, $\sigma_0 = 460MPa$, and the hardening exponent $n = 0.07$. These values correspond to an X65 steel.

4.2 Model geometry

The global geometry of the model is a straight pipe. The cross section area is circular with a wall thickness of 20mm. The geometry is illustrated in Fig. 7. Here the outer diameter of

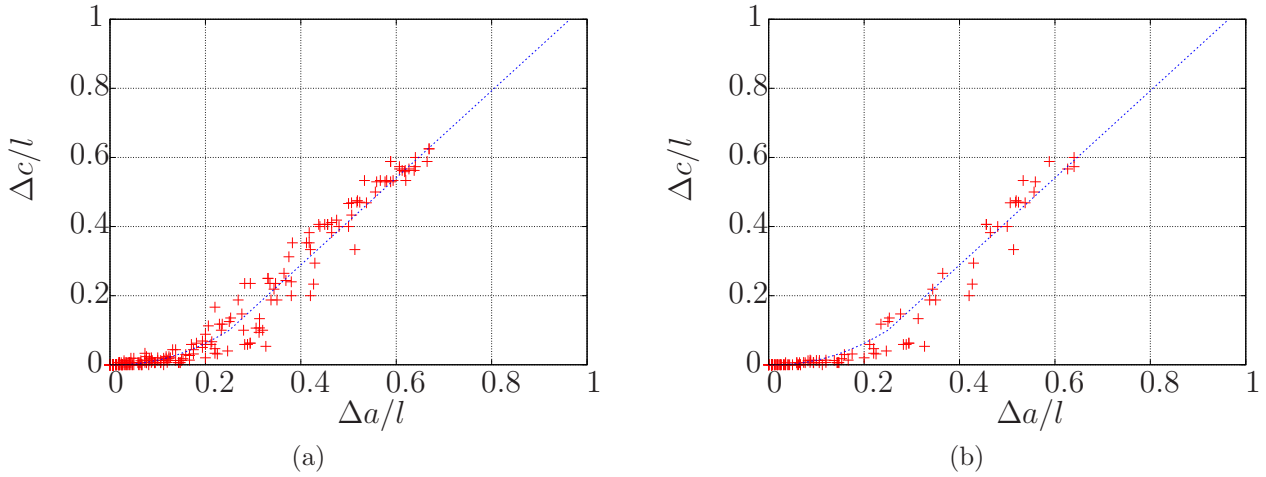

Figure 6: Crack growth data from 3D-analyses performed by Sandvik et al. [21] (+), and dotted line is the trend-line. (a) shows all the 81 3D-analyses and (b) shows only those with no internal pressure. a is the crack depth, c is the half crack length and l is the initial ligament size.

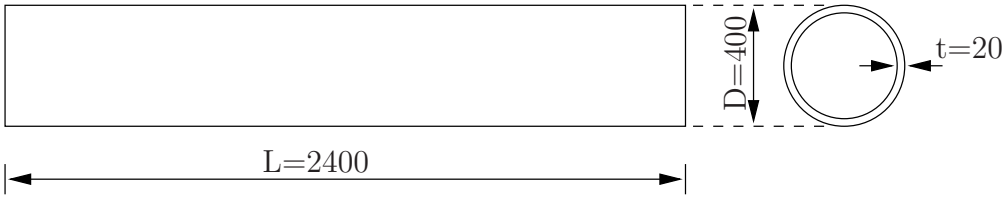

Figure 7: Pipe geometry.

the pipe is 400mm, and the total length of the pipe segment is 2400mm (six times the outer diameter). Three crack length ratios of crack length to circumference ($2c/O$) have been studied: 0.05, 0.10 and 0.30. The initial relative crack depth was was set to $a/t = 0.2$ in all three cases.

4.3 Numerical results

Effect of circumferential crack growth, tension loading

In practise, one could expect some effect of crack growth in the circumferential direction. How important this effect is depends upon several factors. Some of these factors are the initial crack geometry related to the global geometry, loading conditions, material properties and crack growth relations. An important aspect is to know the magnitude of the circumferential crack growth compared to the crack growth in the thickness direction. The result of 81 3D-analyses is shown in Fig. 6. In the following pipe-analyses the trend-line (dashed line) in Fig. 6 is used for the Line-spring model. In the legends in Figs. 8-10, "w/o d2c" expresses analyses without crack growth in the circumferential direction. "w d2c" expresses analyses taking circumferential crack growth into account. 3D is the data from 3D-calculations performed using ABAQUS. For the comparisons, a nominal strain measure was chosen obtained as pipe elongation divided by original pipe length.

The line-spring results are now compared with some recently performed 3D analyses (Zybell [31]). For the case of $2c/O = 0.05$, Fig. 8, the line-spring model is run both with and without circumferential crack growth. It is shown that the effect of circumferential crack growth is important. If circumferential crack growth is not taken into account, the Line-spring model predicts a non-conservative result compared to the 3D-analysis. When the effect of circumferential crack growth is taken into account in the line-spring model, the comparison becomes accurate.

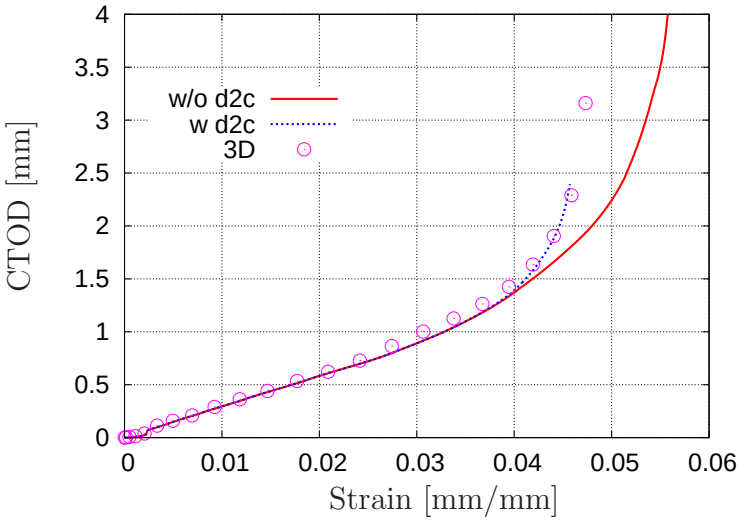

Figure 8: Comparison of nominal strain vs. CTOD for pipe in pure tension. Initial crack length, $2c/O = 0.05$, and initial crack depth, $a/t = 0.2$.

When the ratio of crack length to circumference, $2c/O$, is increased from 0.05 to 0.10, the effect of the circumferential crack growth decreases (see Fig. 9).

In Fig. 10 the crack length to circumference, $2c/O$, is now increased to 0.30, and the effect of the circumferential crack growth is negligible. When the crack growth is initiated at a strain of approximately 2.4%, a very small increase in the global strain is needed for unstable crack growth to occur. The results for the Line-spring model are then overlapping, and both gives some conservatism compared to the 3D-analysis. In this case the percentage increase in crack length is about 8%. Still the initial $2c/a$-ratio is very high. Due to the tensile loading the crack will experience little stable crack growth before unstable crack growth occurs. This is seen by the very sudden change in the slope of the curve.

An error-estimate is proposed to quantify the effect of taking circumferential crack growth into account. The error-estimate is expressed as

$$\alpha = \frac{CTOD_w - CTOD_{w/o}}{CTOD_w} \tag{10}$$

where $CTOD_w$ is the $CTOD$ for the analyses where circumferential crack growth is taken into account, and $CTOD_{w/o}$ is taken from the analyses where circumferential crack growth is neglected.

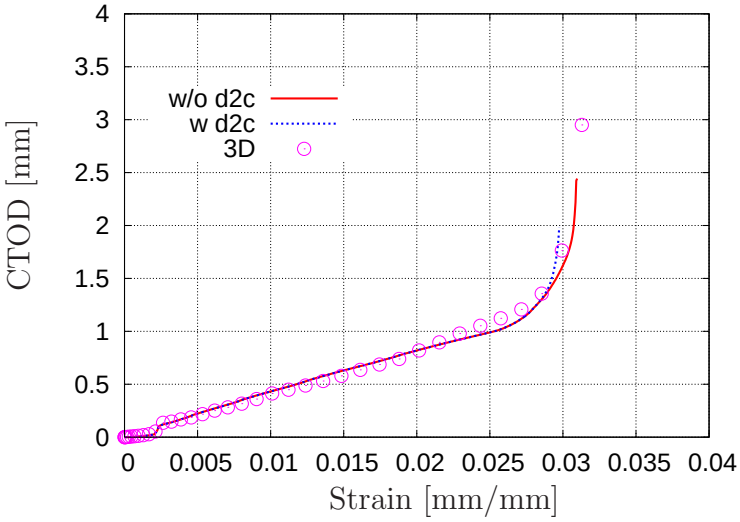

Figure 9: Comparison of nominal strain vs. CTOD for pipe in pure tension. Initial crack length, $2c/O = 0.10$, and initial crack depth, $a/t = 0.2$.

The values for $CTOD_w$ and $CTOD_{w/o}$ used in Eq. 10 are chosen corresponding to a specified slope of the strain versus $CTOD$ curves (e.g. Fig. 9). When ductile crack growth is initiated, the slope increases. When the slope reaches 10 times the slope in the area where ductile crack growth has not been initiated, the data is recorded. The results are presented in Fig. 11 for different crack length ratios ($2c/O$) and for two initial crack depth ratios (a/t). It is seen that the error-estimate decreases for increasing crack length ratios. One also observes that the error estimate increases somewhat when initial crack depth ratio decreases.

4.4 Effect of biaxial loading on circumferential crack growth

Fig. 12 shows the effect of taking circumferential crack growth into account when the pipe is subjected to biaxial loading (internal pressure combined with tension or bending). Pipes without internal pressure are included as a reference case. Note that as the surface crack was located on the outside of the pipe, no effect of pressure on the crack faces was present. The initial crack geometry in this case is $a_0 = 4mm$ and $2c_0 = 50mm$. Four levels of internal pressure are analysed, where the pressure level is given as the ratio between the stress in the circumferential direction to the initial yield stress. The effect of taking circumferential crack growth into account for biaxial loading is here seen for all cases. The effect is however slightly reduced with increasing internal pressure.

It is worth to note that for the pipe in bending with a low internal pressure ($\sigma_h/\sigma_0 \leq 0.2$), the pipe suffers from local buckling rather than crack growth through the thickness. For the case of $\sigma_h/\sigma_0 = 0.2$, the crack opens until $CTOD$ equal to about $4mm$ before the pipe buckles. For higher internal pressures, the pipes do not buckle, hence the crack grows through the thickness. A noticeable effect of taking circumferential crack growth into account is observed.

As also demonstrated by Jayadevan et. al (2005), an increasing internal pressure reduces the

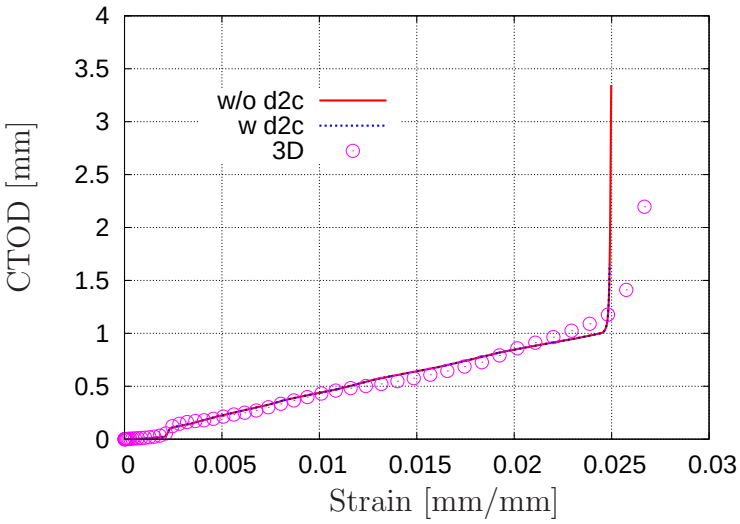

Figure 10: Comparison of nominal strain vs. CTOD for pipe in pure tension. Initial crack length, $2c/O = 0.30$, and initial crack depth, $a/t = 0.2$.

strain carrying capacity of the pipe.

Effect of constraint corrected resistance curves

Fig. 3a shows experimental crack growth resistance curves for three standard test-specimens having different level of constraint. In Fig. 3b, the curves are normalised by employing the T-stress in Eq. 5. In this case, the curves from the SENB specimen with a relative crack depth of $a/t = 0.5$ is used as the reference curve. This specimen also yielded the highest constraint, i.e. gives the lowest fracture toughness. The two unknown parameters in Eq. 5, α and m are then fitted to be $\alpha = 0.7602$ and $m = 1.1352$.

When using the resistance curve for the deepest SENB-specimen in numerical analysis of a SENT-specimen, the curve "*SENB*" in Fig. 13 for the SENT-specimen without taking the effect of constraint correction into account is obtained. It is shown that the load carrying capacity of the specimen is significantly reduced compared to the case when using the resistance curve from the SENT-specimen. When the SENT specimen is constraint corrected, i.e. the resistance curve from the SENB specimen is multiplied by the correction factor, $g(T)$, the same result is obtained as for the SENT-specimen analysed with it's own resistance curve.

In Fig. 14 the surface cracked pipe subjected to pure tensile loading is analysed using different crack growth resistance curves. The case having no ductile crack growth is here included as a reference case, marked "*stationary*". The curve "*SENT*" is the pipe run with the resistance curve for the SENT geometry having the same a/t (from Fig. 3) and thus having almost similar constraint conditions as the pipe. The curve marked "*senb*" is the same model - the only difference is the resistance curve. This analysis is carried out using the curve from the SENB-geometry with a crack ratio of $a/t = 0.5$. This is a high constraint geometry, thus giving less resistance to ductile crack growth. This is clearly seen as unstable crack growth in the pipe

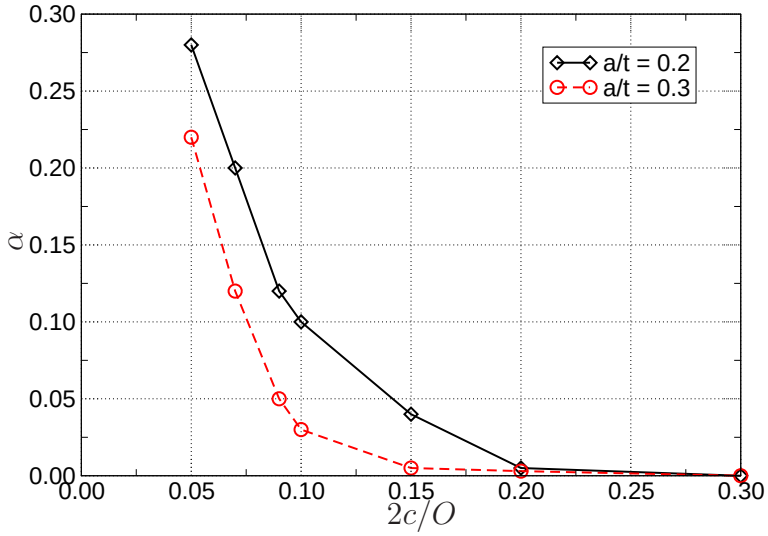

Figure 11: Effect of circumferential crack growth for different crack lengths ratios ($2c/O$) and crack depth ratios (a/t). α is the error estimate (Eq. 10).

occurs at a much lower nominal strain. When the resistance curve for the SENB ($a/t = 0.5$) is constraint-corrected the results are similar as for the pipe with the SENT-resistance curve.

5 Concluding remarks

The present study focuses on the effect of circumferential crack growth and constraint effects in surface cracked pipe segments.

Three different crack lengths are studied with respect to circumferential crack growth. The correspondence between 3D- and line-spring analyses is good. It is clearly seen for the shortest initial crack length ($2c/O = 0.05$) that the circumferential crack growth is important (see Fig. 11). For longer initial crack lengths ($2c/O \geq 0.1$), the crack growth in the circumferential direction has a minor effect. The effect of biaxial loading is also shown. The effect is significant for both tension and bending in combination with an internal pressure. For the cases with a low internal pressure, the pipes subjected to global bending buckled before unstable crack growth occurred.

The effect of constraint corrected resistance curves demonstrated that the crack growth resistance curve has a large influence on the crack growth behaviour. The SENB-geometry has traditionally been used to quantify the fracture toughness for a material, but previous and the present studies show that this can lead to very conservative results. The application of the "elastic-plastic" T-stress seems to work well as a constraint measure also under large scale yielding.

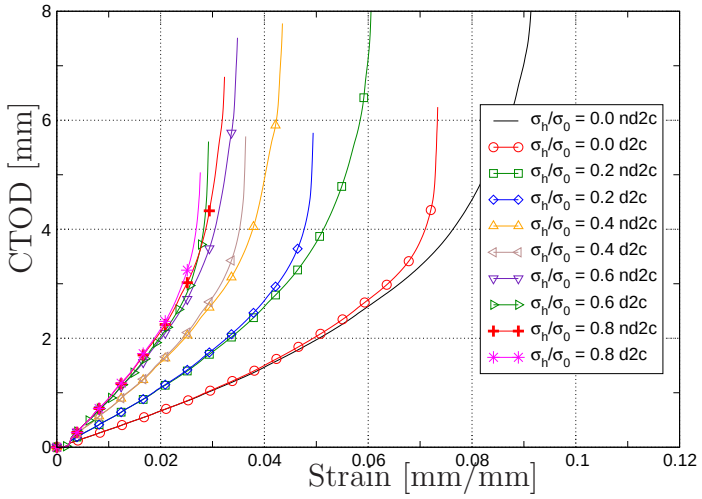

(a)

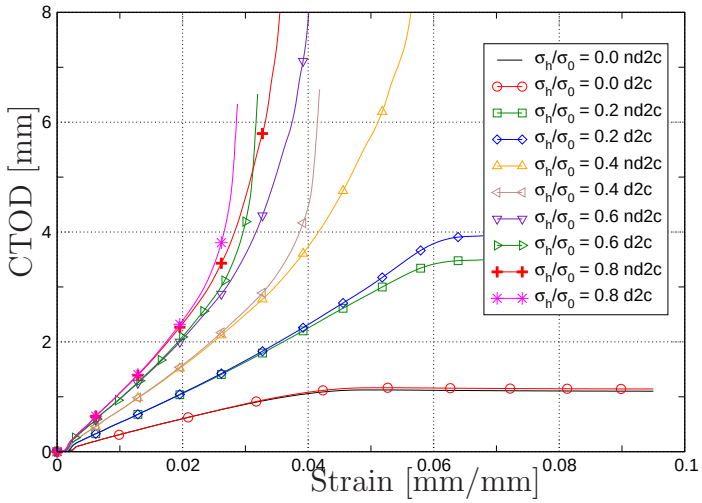

(b)

Figure 12: Effect of internal pressure on CTOD versus nominal strain for pipe subjected to (a) tensile and (b) bending loading.

6 Acknowledgements

The authors would like to acknowledge Mr. A. Sandvik, Professor K. Holthe and Dr. E. Østby for helpful discussions and assistance regarding this work. Also the support from the participants in the joint industry project "Fracture Control Offshore Pipelines" is highly appreciated.

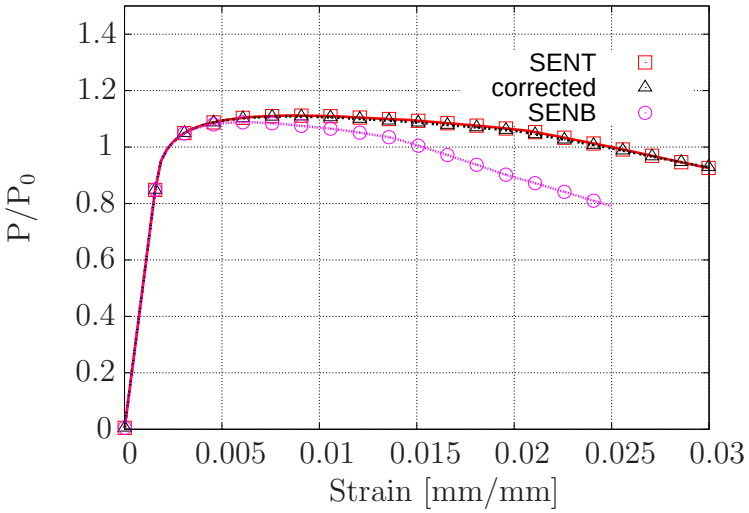

Figure 13: Nominal strain versus normalised applied load.

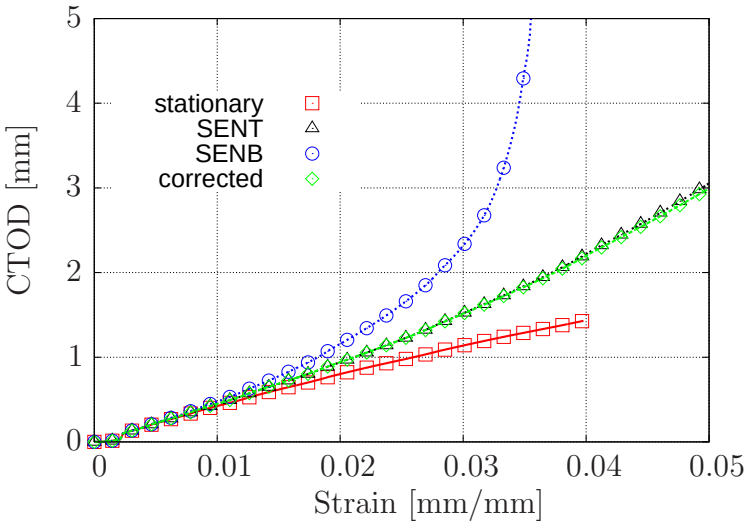

Figure 14: A pipe in pure tension loading. Two different crack growth resistance curves are employed for the analyses - a SENT-curve and a SENB-curve.

References

[1] R.A. Ainsworth and N.P. O'Dowd. A framework for including constraint effects in the failure assessment diagram approach for fracture assessment. *In: Proceedings of ASME Pressure Vessels and Piping Conference, PVP-vol.287/MD-vol. 47*, 1994.

[2] E. Berg, E. Østby, C. Thaulow, and B. Skallerud. Comparisons between the line-spring model and full scale testing of pipe-segments. *Work in progress*, 2007.

[3] C. Betegon and J. W. Hancock. Two parameter caracterization of elastic-plastic crack-tip fields. *Journal of Applied Mechanics*, 58:104–110, 1991.

[4] British Standard. BS7448:4 fracture mechanics thoughness tests. method for determination of fracture resistance curves and initiation values for stable crack extension in metallic materials. *British Standards Institution*, 1997.

[5] British Standard. BS7910:2000 guide on methods for assessing the applicability of flaws in metallic structures. *British Standards Institution*, 2000.

[6] M. Chiesa, B. Skallerud, and D. Gross. Closed form line spring yield surfaces for deep and shallow cracks: formulation and numerical performance. *Computers and Structures*, 80:533–545, 2002.

[7] M. Chiesa, B. Skallerud, and B. Nyhus. Efficient numerical procedures for fracture assessments of surface cracked shells. *Proceeding of European Conference of Computational Mechanics, Krakow, Poland*, 2001.

[8] Z. Z. Du and J. W. Hancock. The effect of non-singular stresses on crack-tip constraint. *Journal of the Mechanics and Physics of Solids*, 39:555–567, 1991.

[9] C. A. Felippa and C. Militello. Membrane triangles with corner drilling freedoms—ii. the andes element. *Finite Elements in Analysis and Design*, 12(3-4):189–201, 1992.

[10] J. W. Hancock, W. G. Reuter, and D. M. Parks. Constraint and toughness parametrized by: T-stress. *American Society for Testing and Materials, Philadelphia*, 1171:21–40, 1993.

[11] K. R. Jayadevan, E. Berg, C. Thaulow, E. Østby, and B. Skallerud. Numerical investigation of ductile tearing in surface cracked pipes using line-springs. *International Journal of Solids and Structures*, 43:2378–2397, 2006.

[12] K. R. Jayadevan, C. Thaulow, E. Østby, E. Berg, B. Skallerud, K. Holthe, and B. Nyhus. Structural integrity of pipelines: T-stress by line-spring. *Fatigue and Fracture of Engineering Materials and Structures*, 28:467–488, 2005.

[13] S. G. Larsson and A. J. Carlsson. Influence of non-singular stress terms and specimen geometry on small-scale yielding at crack tips in elastic-plastic materials. *Journal of the Mechanics and Physics of Solids*, 21:263–277, 1973.

[14] H. Lee and D. M. Parks. Fully plasticanalyses of plane strain single-edge-cracked specimens subjected to combined tension and bending. *International Journal of Fracture*, 63:329–349, 1993.

[15] H. Lee and D. M. Parks. Enhanced elastic-plastic line-spring finite element. *International Journal of Solids and Structures*, 32(16):2393–2418, 1995.

[16] S. Linkens, Formby, C. L., Ainsworth, and R. A. A strain-based approach to fracture assessment – example applications. *Proceedings of fifth International Conference on engineering structural integrity assessment, EMAS*, 63, 2000.

[17] B. Nyhus, Z.L. Zhang, and C. Thaulow. Normalisation of material crack resistance curves by the T-stress. *Proceedings of the 14th European Conference of Fracture, Poland*, 2002.

[18] N. P. O'Dowd and C. F. Shih. Two-parameter fracture mechanics theory and applications. *American Society for Testing and Materials, Philadelphia*, 24(1207):21–47, 1994.

[19] J.R. Rice. The line spring model for surface flaws. *Swedlow, J.L. (Ed.), The Surface Crack: Physical Problems and Computational Solutions. American Society of Mechanical Engineers, New York*, pages 171–185, 1972.

[20] J.R. Rice and N. Levy. The part-through surface crack in an elastic plate. *Journal of Applied Mechanics*, 39:185–194, 1972.

[21] A. Sandvik, E. Østby, and C. Thaulow. A probabilistic fracture mechanics model including 3D ductile tearing of bi-axially loaded pipes with surface cracks. *Preprint submitted to Elsevier Science*, 2006.

[22] T.L. Sham. The determination of the elastic t-stress using higher order weight functions. *International Journal of Fracture*, 48:81–102, 1991.

[23] B. Skallerud, E. Berg, and K. R. Jayadevan. Two-parameter fracture assessment of surface cracked cylindrical shells during collapse. *Engineering Fracture Mechanics*, 73:264–282, 2005.

[24] B. Skallerud and B. Haugen. Collapse of thin shell structures - stress resultant plasticity modelling within a co-rotated andes finite element formulation. *International Journal for Numerical Methods in Engineering*, 36:1961–1986, 1999.

[25] B. Skallerud, K. Holthe, and B. Haugen. Thin shell and surface crack finite elements for simulation of combined failure modes. *Computer Methods in Applied Mechanics and Engineering*, 194(21-24):2619–2640, 2005.

[26] L. Storslett. Fracture control offshore pipelines: Ductile crack growth of semi-elliptical surface cracks. *Master's thesis, Norwegian University of Science and Technology, Norway (in Norwegian)*, 2004.

[27] C. Thaulow, E. Østby, B. Nyhus, Z. L. Zhang, and B. Skallerud. Constraint correction of high strength steel. selection of test specimens and application of direct calculations. *Engineering Fracture Mechanics*, 71:2417–2433, 2004.

[28] C. Thaulow, B. Skallerud, K. Holthe, E. Berg, E. Østby, B. Nyhus, and J. Ødegård. Fracture control of pipelines using linkpipe: From rule based design to direct calculations. *Proceedings of HSLP-IA2006: International seminar on Application of High Strength Line Pipe and Integrity Assessment of Pipeline, 2006, Xi'an, People's Republic of China*, 2006.

[29] Y.-Y. Wang and D. M. Parks. Evaluation of the elastic t-stress in surface-cracked plates using the line-spring method. *International Journal of Fracture*, 56:25–40, 1992.

[30] C. S. White and D. M. Parks. Elastic-plastic line-spring finite elements for surface-cracked plates and shells. *Journal of Pressure Vessel Technology*, 104:287–292, 1982.

[31] L. Zybell. Finite element analysis of ductile fracture behaviour of pipe sections with surface cracks. *Master's thesis, Norwegian University of Science and Technology, Norway*, 2004.

PAPER III

Ultimate fracture capacity of pressurised pipes with defects – comparisons of large scale testing and numerical simulations

E. Berg, E. Østby, C. Thaulow, B. Skallerud

Engineering Fracture Mechanics **75**(8):2352–2366, 2008.

Ultimate fracture capacity of pressurised pipes with defects – comparisons of large scale testing and numerical simulations

E. Berg[1], E. Østby[2], C. Thaulow[3], B. Skallerud[1]

[1]Department of Structural Engineering, Norwegian University of Science and Technology, 7491 Trondheim, Norway
[2]SINTEF Materials and Chemistry, 7491 Trondheim, Norway
[3]Department of Engineering Design and Materials, Norwegian University of Science and Technology, 7491 Trondheim, Norway

ABSTRACT

In this paper results from large scale 4-point bending tests of pipe-segments are compared with numerical analyses using LINK$_{pipe}$. The experiments were carried out as a part of the joint industry project Fracture Control – Offshore Pipelines. The comparisons between large scale testing of pipelines and numerical analyses also address the effect of biaxial loading on the strain capacity. The defect is positioned on the tension side of the pipe when applying the load. A parametric study on changing the nominal wall thickness of the pipe is carried out. Due to variation in the yield stress, a parametric study to see the effect of this variation was also performed. The results demonstrate that considering ductile crack growth and biaxial loading are important elements in fracture assessment procedures for pipe-lines.

Keywords: Fracture mechanics; Line-spring; Biaxial loading; Ductile crack growth; Large scale testing

1 Introduction

Surface cracks due to welding defects, corrosion, etc., may occur in pipelines. Offshore pipelines usually consist of many kilometres of girth welds, thus the possibilities of defects being present must be taken into account during design. Further, there is an emerging trend that pipelines may be subject to larger deformation both during installation and operation. For installation scenarios the reeling method is well known, yielding plastic strains in the pipe up to 3%. But also other installation methods, like e.g. S-laying, may result in plastic strains. During operation on-bottom snaking, upheaval buckling, landslide and seismic activity can lead to

significant deformations in the pipe. For these latter cases this will usually occur while the pipe is pressurised, and there is a biaxial loading in the pipe wall. Current fracture assessment procedures are not developed to handle cases where global plastic deformations occur. Thus, there has been a great interest in developing a fracture assessment procedure to address such loading scenarios in the recent years (see e.g. Linkens et al. [11]; Bratfors [3]; Wang et al. [26]; Østby [14, 15]; Budden [4]), often referred to as strain-based approaches. A specific issue of concern is the effect biaxial loading. For pipes subjected to a global bending moment, two competing failure modes are acting at the same time. The first failure mode is fracture where the crack grows through the thickness, and the second failure mode is a structural failure, e.g. local buckling. For the local buckling failure mode the biaxial loading has been shown to have a beneficial effect on the deformation capacity (Vitali et al. [25]). However, numerical studies (Shimanuki and Inoue [21];Jayadevan et al. [9],[8] and Østby et al. [17]) have pointed in the direction that the biaxial loading may increase the crack driving force as a function of the applied strain, an effect not accounted for in existing assessment procedures. Thus, it could be detrimental for the deformation capacity of pressurised pipes with defects. Østby and Hellesvik [16] have recently provided experimental large scale verification of the detrimental effect of biaxial loading on the strain capacity of pipes. These results clearly demonstrate the need for assessment procedures capable of handling this effect.

In fracture assessments of pipelines, the wall-stresses are mainly of membrane type (see Chiesa et al. [6]). This will lower the constraint level in the near crack-tip stress field, thus increasing the fracture toughness. Use of tearing curve based on a high-constrained fracture specimen can lead to very conservative decisions. A methodology to account for reduced constraint using a single edge notched tensile specimen (SENT) for fracture assessment was proposed by Nyhus et al. [12] and demonstrated by Berg et al. [2]. To account for surface cracks, line-springs are used herein (Rice [18];Rice and Levy [19];White and Parks [27];Chiesa et al. [5];Skallerud et al. [22];Jayadevan et al. [8];Thaulow et al. [24]). The present study addresses comparisons between the shell- and line-spring model and the results from the large scale testing presented in Østby and Hellesvik [16]. The software LINK$_{pipe}$ is employed (see Skallerud et al. [23] for details). Ductile crack growth in thickness and circumferential direction is accounted for in the numerical analyses in this study by employing the crack growth resistance curve (see Sec. 5). The effects of changing the nominal wall thickness and yield stress are also studied and presented herein. Some of the experiments are also performed with biaxial loading by means of internal pressure in addition to global bending. All of the experiments are performed with an external surface crack, thus pressure on the crack faces is not relevant.

2 Theory

2.1 Line-spring

A surface flaw in a finite element model consisting of shell elements can be accounted for by employing line-spring elements. In the elastic line-spring formulation, the generalised displacements and the internal forces are related through the compliance matrix. This matrix is determined from single edge notched (SEN) specimens using the energy/compliance proposed

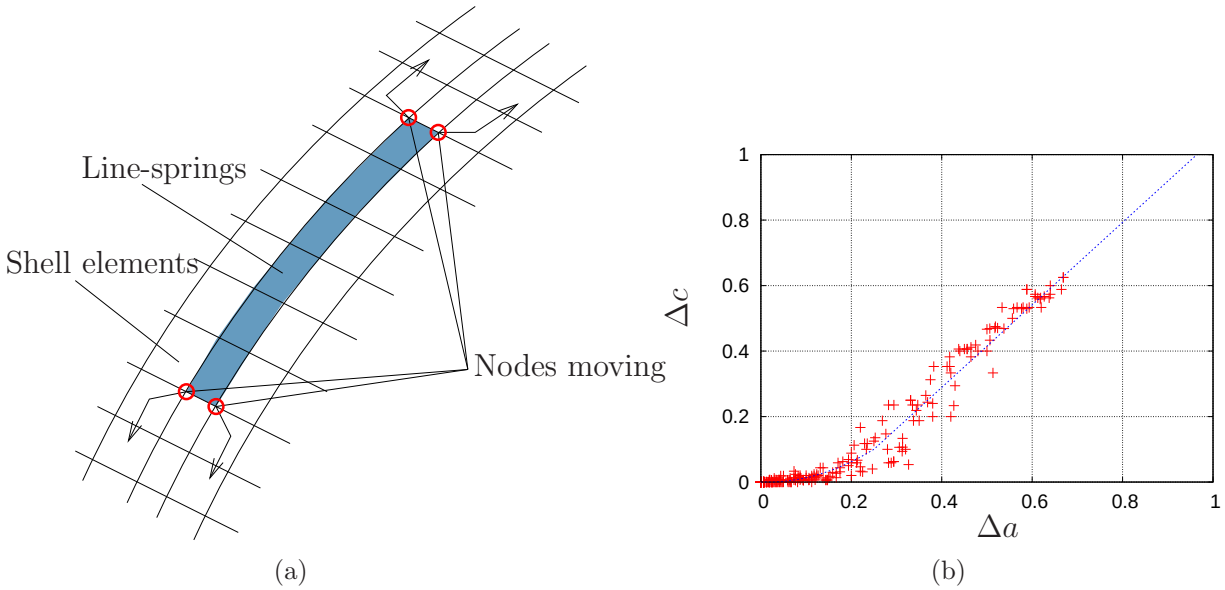

Figure 1: Crack growth in circumferential direction. (a) schematic view of the method and (b) interpolated trend line to quantify the circumferential crack growth based on a set of 3D-analyses performed by Sandvik et al. [20].

by Rice and Levy [19]. The elastic-plastic line-spring element is based on a set of convex yield surfaces, $\Phi\left\{Q_i; a; t; \sigma_y(\varepsilon^p)\right\}$, where Q_i are the generalised forces in the line-spring element, a is the crack depth, t is the wall thickness, and $\sigma_y(\varepsilon^p)$ is the current uniaxial yield stress at an equivalent plastic strain of ε^p according to the material's stress-strain curve. The yield surfaces for the line-spring element use the tabulated values for different crack depth to thickness ratios published by Lee and Parks [10]. Simulations of additional crack ratios were carried out by the authors to refine the transition between the tabulated crack ratios provided in the literature. Further details of theory and implementation of the software LINK$_{pipe}$ are provided by Skallerud et al. [22, 39].

Ductile crack growth is implemented in the line-spring element as an incremental formulation. The crack propagates quasi-statically through the thickness based on the crack growth resistance curve given as input to the analysis. This crack growth resistance curve can be treated as a material parameter for a given constraint level. The updated crack dimensions at the end of a load increment is expressed as $a^{(i+1)} = a^{(i)} + \Delta a^{(i)}$ and $c^{(i+1)} = c^{(i)} + \Delta c^{(i)}$. The crack growth resistance curve can be obtained from fracture mechanic experiments or from a damage mechanic numerical analysis (e.g. Gurson-Tvergaard-Needleman model). The crack growth resistance curve used is on the form presented in Fig. 7.

Crack growth in circumferential direction is accounted for and implemented as shown in Fig. 1a, and presented in detail by Berg et al. [2]. A set of 3D-analyses were performed by Sandvik et al. [20], and the circumferential crack growth was obtained in these analyses. An interpolation between these 3D-results was performed to make a general quantification of the circumferential crack growth (see Fig. 1b).

3 Experimental setup and measurements

A thorough presentation of the large scale testing can be found in Østby and Hellesvik [16].

3.1 Experimental set-up

The experiments were carried out by subjecting a tubular pipe to four point bending. The test rig was oriented horizontally along the floor. The load was applied using a hydraulic cylinder having a maximum capacity of $1500kN$. The maximum stroke of the cylinder was $1500mm$, which was capable of generating a strain level of 7-8% in the axial direction of the pipe body assuming constant curvature in the bending process. A complete setup of the rig and pipe is shown in Fig. 2. To ensure that the load was distributed evenly to the two inner rods, pin-loaded spreader plates were used. To prevent local buckling in the pipe where the tension rods were connected, the part between the outer and inner tension rod were filled with concrete. The open space of $1900mm$ between the two inner tension rods were then filled with air or water.

The crack was positioned on the tension side at the mid-span of the pipe where the minimum wall thickness was measured. Details on crack geometry is presented in Sec. 4. For the cases of biaxial loading, the space between the two inner tension rods were filled with pressurised water.

3.2 Measurement techniques

The measurement techniques include several approaches to measure the global and local behaviour of the experiments. The force in the hydraulic cylinder was directly measured using the hydraulic pressure. The cylinder stroke was measured using a displacement transducer. The forces in the tension rods were measured using load cells. Additional displacement measures were also performed - the displacement at the centre of the pipe and at 2 outer diameters at each side of the mid-pipe.

The strain in the pipe during the deformation was measured using two techniques. Strain gauges were attached on the pipe at distances 0.5, 1.0 and 2.0 times the outer diameter from the mid-span of the pipe on the tension and on the compression side (see Fig. 3). Another strain measure used was to assume constant curvature along the pipe for the inner $1900mm$ segment, $\varepsilon = \frac{r}{R}$, where r is the outer radius of the pipe and R is the radius of curvature. Østby and Hellesvik [16] showed that the two strain measurements yielded consistent values. The strain gauges showed the same strain values up to material yielding. Post-yielding in the pipe gave some difference between the strain gauges. To define a characteristic bending strain measure, the results from the different strain gauges were averaged.

The crack opening displacement ($CTOD$) can not be measured directly from the experiments, thus the crack mouth opening displacement ($CMOD$) was measured using clip gauges. The

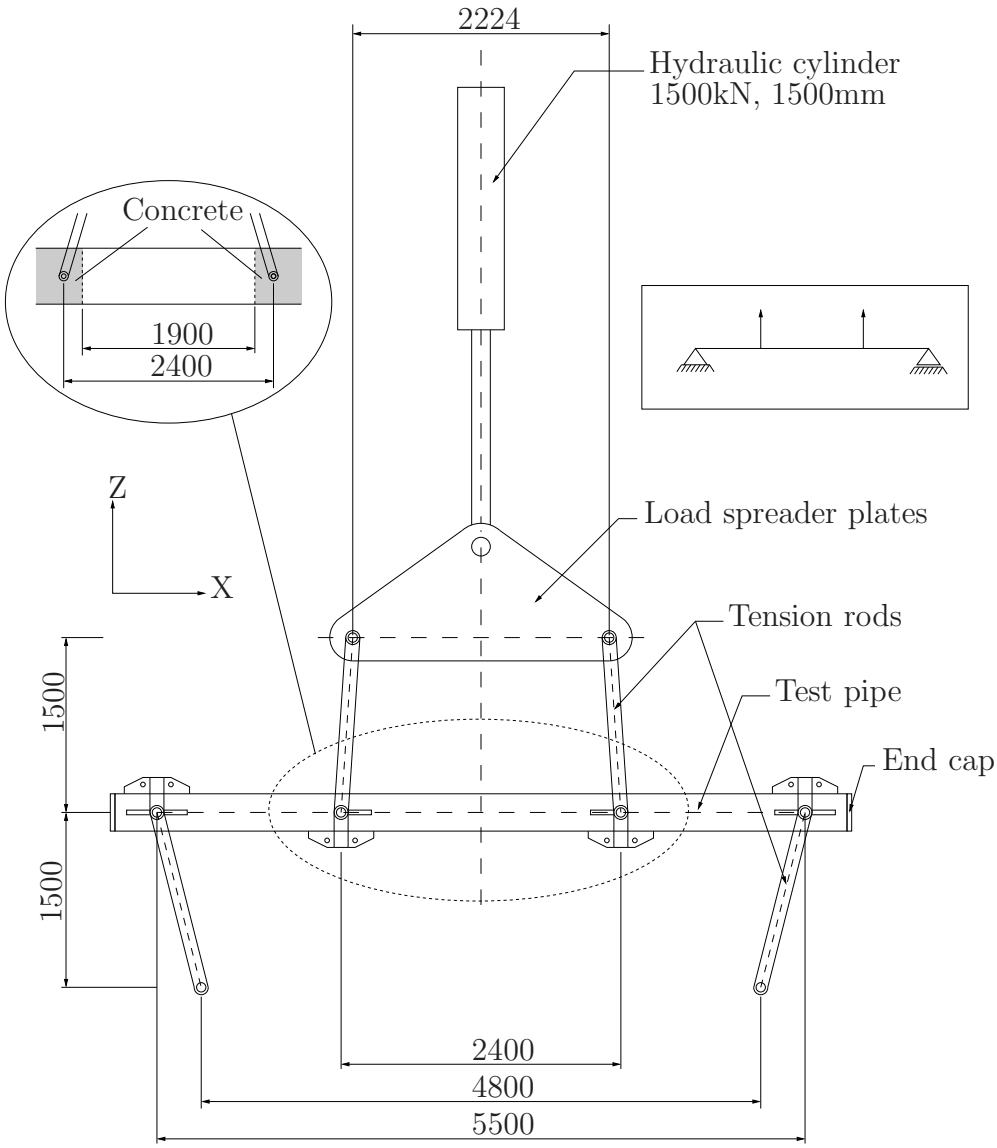

Figure 2: Overview of the experimental setup.

clip gauges were mounted in spark eroded grooves in the pipe at the centre of the defect. The attack point of the clip gauge was $0.2mm$ below the pipe surface.

For one pipe in each of the three pairs of pressure levels (see Table 1), silicon replica were made to measure the defect size during the experiment. An initial replica was produced as a reference. At different deformation levels, new replica were extracted. These replica were used to measure the current crack extension and the current $CTOD$. Cross sections of the replica were examined in a light optical microscope to measure the physical crack extension and $CTOD$. The amount of crack growth was calculated by comparing the current and the initial silicon replica, where the initial replica represented zero crack extension. They were then used to convert from the measured $CMOD$ to $CTOD$.

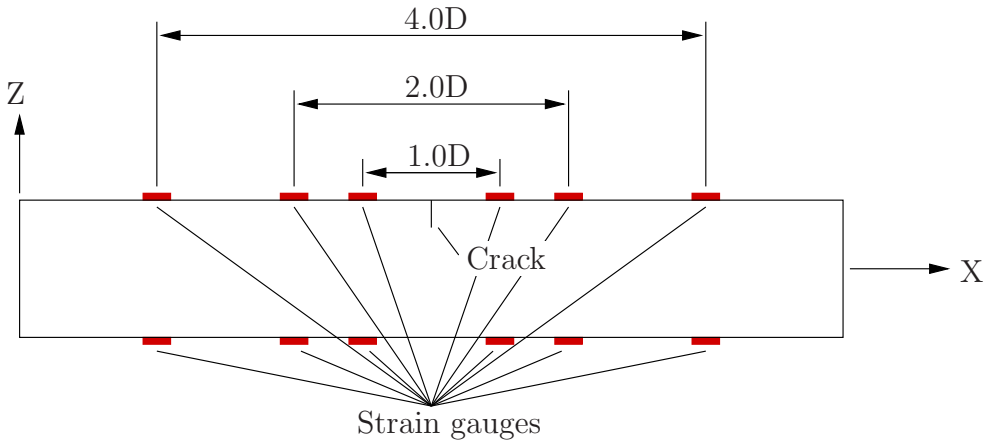

Figure 3: Positions of the strain gauges on the pipe wall. D is the outer diameter.

4 Geometry of the pipe and modelling aspects

The initial experimental configuration was a straight tubular pipe subjected to four point bending with/without internal pressure. The numerical model only consisted of the space between the concrete fillings, hence the length was $1900mm$. The nominal outer diameter of the pipe was $323.9mm$, and the nominal wall thickness $14.9mm$. The pipes were seamless, thus the wall thickness was varying somewhat around the circumference due to the manufacturing process. Spark erosion was used to introduce the crack.

The numerical pipe segment was subjected to a global constant bending moment. For the cases of biaxial loading, an internal pressure along with an axial tensile force due to the closed ends was also applied. Fig. 4 shows the boundary conditions. To avoid a singular system and rigid body motion, the left end of the pipe segments was constrained in the X- and Y- and Z-directions. The right end of the pipe segment was free to move in the X-direction, but constrained in the Y- and Z-directions. The rotational degree of freedom about the X-axis at the left end was constrained, whereas the other rotational degrees of freedom were free. The pipe segment was then subjected to a bending moment about the Y-axis at both ends. The end planes were kept planar during the analysis. The bending moment was applied at the center of the end planes, and the displacements were distributed to all the nodes in the end planes.

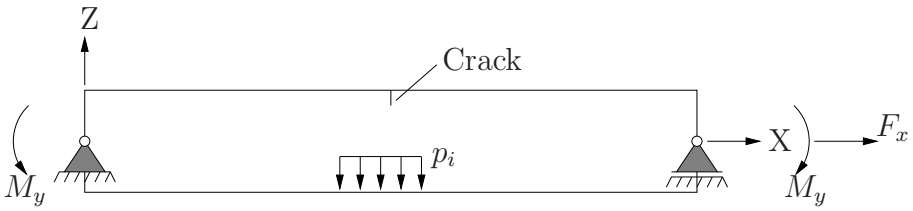

Figure 4: Boundary and loading conditions.

Fig. 5 shows the crack geometry used in the numerical analyses. The crack is symmetric about the Z-axis. The initial crack length, $2c_0$, was $100mm$ for all experiments, and thus the same for the analyses. The initial crack depth, a_0, was varying from $2.75mm$ to $3.25mm$ for the

different experiments. The analyses were performed using the crack depth that corresponded to the actual experiment. The wall thickness, t, showed variations from $13.97mm$ to $14.48mm$. The local variations in the wall thickness was not taken into account in the analyses. The wall thickness used in the analyses was kept constant corresponding to the smallest nominal measured value around the circumference for each of the experiments. The wall thickness used in the numerical analyses corresponds to the values in Table 1. A parametric study of the effect of changing the wall thickness is also performed and demonstrated later in this paper. Table 1 gives an overview of the geometries and internal pressure from each of the experiments.

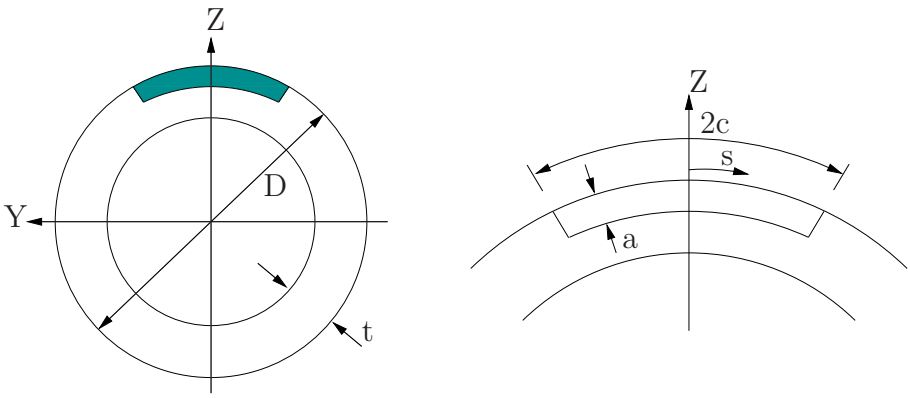

Figure 5: Crack position and geometry.

The initial crack was spark eroded at the position where the measured wall thickness was at its minimum, and the values are shown in Table 1. The initial crack depth was aimed to be $3.0mm$, but as can be seen in Table 1, some variation was measured.

Table 1: Local geometry and internal pressure for the experiments.

Experiment	$t[mm]$	$a_0[mm]$	$2c_0[mm]$	$p_i[MPa]$
1	14.45	2.75	100	32.5
2	14.12	3.11	100	0
3	14.48	2.78	100	32.5
4	14.45	3.20	100	13.5
5	13.97	3.25	100	0
6	14.23	3.09	100	13.5

5 Material properties

The pipe-material in these experiments was an X65 steel. To obtain the stress-strain curve, tensile specimens were cut from the pipe at four positions along the circumference, as shown in Fig. 6. The tensile specimens were cut from a region not subjected to plastic deformations during the tests. The elastic material properties were measured to Young's modulus, $E = 200GPa$, and Poisson's ratio, $\nu = 0.3$. The average yield stress ($\sigma_{0.2}$), average tensile strength

(σ_{TS}) and engineering strain at maximum load (ε_{max}) was measured to respectively 484.4MPa, 559.5MPa and 7.6%.

Although some variations in the yield stress level along the circumference can be seen in Fig. 6, the hardening is similar. The average material properties were used as input data to the finite element analyses. Note that the stress-strain curves used herein are monotonic curves.

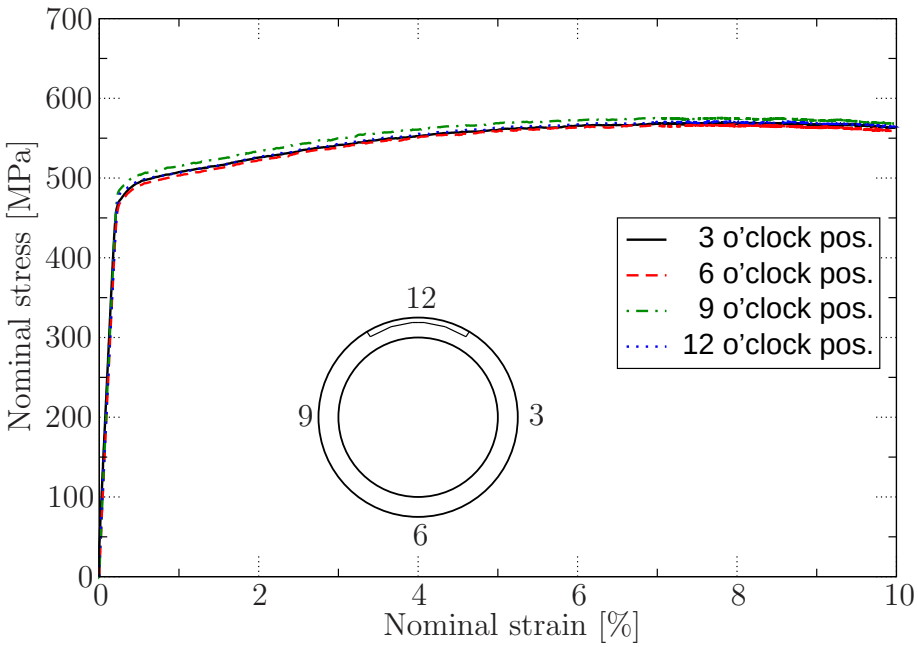

Figure 6: Stress-strain curves from the experiments at four different positions along the circumference for Test 1.

The crack growth resistance curve used in the numerical analyses is derived from results obtained from single edge notched tension (SENT) specimens from the same X65 material. It has been demonstrated in Østby and Hellesvik [16] that the crack growth resistance curves measured in the pipes in this study, based on the silicone replicas, were in accordance with the results from the SENT testing. The crack growth resistance curve is shown in Fig. 7a. As can be seen from Fig. 7b, the measured crack growth resistance curves for different levels of internal pressure for the pipes and the curve from the SENT-testing are very similar. The numerical curve from Fig. 7a is also shown together with the experimental curves for clarity. The difference between the experimentally obtained resistance curves is small, hence a size effect is not observed. This is in accordance to R6 [1]. The crack growth resistance curves seems to be insensitive to biaxial loading. This behaviour is previously reported also by Garwood et al. [7] and Nyhus et al. [13].

6 Numerical results

Numerical analyses using LINK$_{pipe}$ were carried out to compare with the large scale tests. For each of the three pairs of experiments, a direct comparison with one corresponding numerical

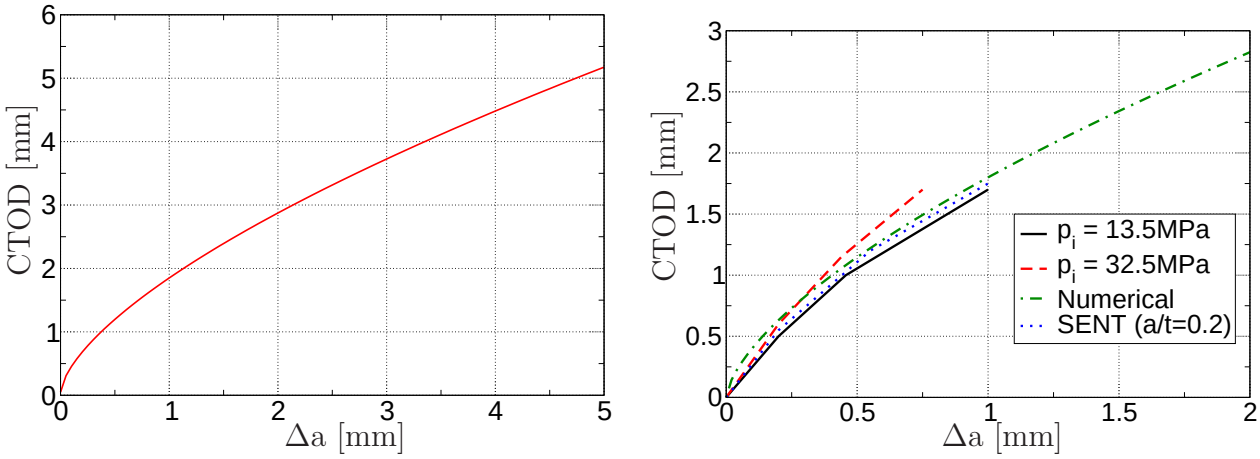

Figure 7: (a) the crack growth resistance curve used in the numerical analyses and (b) experimentally obtained crack growth resistance curves from the pipes with different levels of internal pressure and SENT-specimen.

analysis is presented. A parametric study of the effect of changing the wall thickness is carried out due to the fact that the wall thickness in the experiments are not uniform. A parametric study of varying the yield strength is also presented. The strain measure used in all the comparisons is based on the radius of curvature. For the cases with internal pressure (biaxial loading), an axial force was applied, corresponding to the force caused by the internal pressure when the pipe ends are closed.

Note that the term internal pressure (p_i) refers to the pressure applied in addition to the atmospheric pressure.

6.1 Direct comparisons

For the direct comparisons between large scale tests and numerical analyses, the minimum measured wall thickness is used. Because of the local variations around the pipe circumference, the numerical analyses have probably slightly under-predicted the load carrying area. This will however be discussed in the next section when presenting effect of wall thickness. The internal variations between the two experiments in each of the three pressure levels were small (see Table 1), hence the two numerical analyses did not give significant differences in the results. One of the analyses for each pair are presented here. The $CTOD$ is extracted at the point $s = 0$ (see Fig. 5).

In Fig. 8, the pair of experiments having an internal pressure of $32.5MPa$ (which introduces a hoop stress of about 60% of the yield stress), are compared with a numerical analysis having an initial crack depth of $2.75mm$, and a wall thickness of $14.45mm$. Fig. 8 shows that unstable crack growth occurs at a strain level of about 1.5%. The numerical analysis positions above the experimental curves, thus yields some conservatism. The two experimental curves deviates slightly from each other. Some deviation will always occur in large scale experiments due to

possible variations in the geometry and material. However, it is seen that the numerical analysis captures the tendencies well.

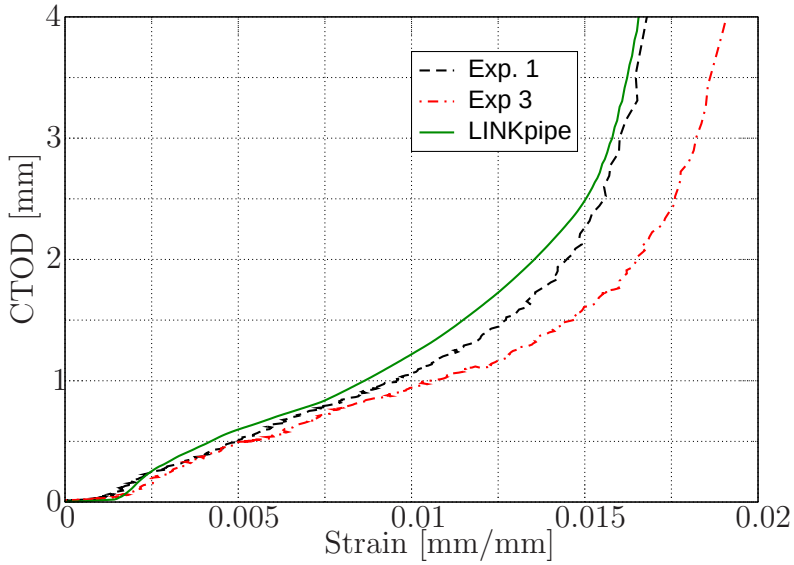

Figure 8: Comparison between large scale tests 1 and 3 and LINK$_{pipe}$ ($p_i = 32.5MPa$).

For this pressure level, the crack reached unstable crack growth and grew through the thickness, thus the failure mode is crack growth. Due to the internal pressure, the hoop stress prevented the pipe from ovalisation and buckling.

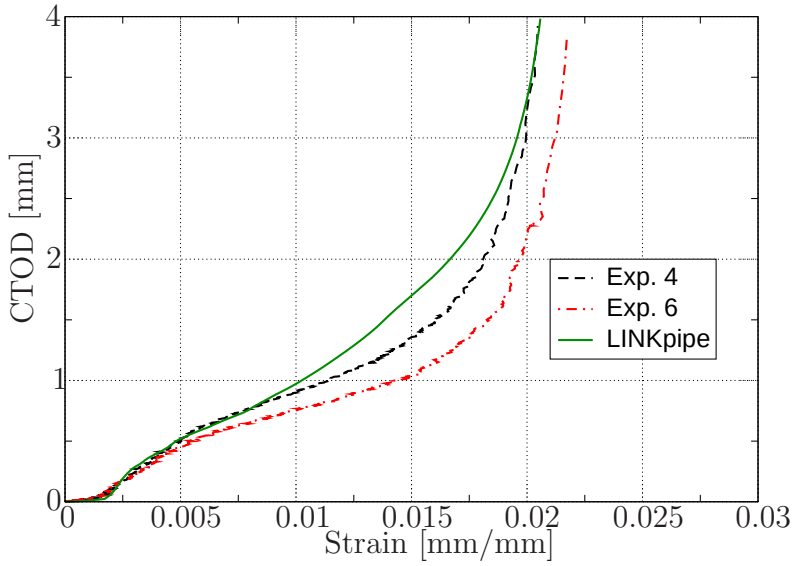

Figure 9: Comparison between large scale tests 4 and 6 and LINK$_{pipe}$ ($p_i = 13.5MPa$).

In Fig. 9, the internal pressure was reduced to $13.5MPa$. The numerical analysis corresponds to experiment 4 in Table 1. The same behaviour of the strain-$CTOD$ curve as from Fig. 8 is observed, but the global strain capacity is somewhat increased. This is in accordance with

results from Jayadevan et al. [8] and Skallerud et al. [22]. The failure mode is also here the crack growth. The results in Fig. 9 shows good correspondence between the numerical analysis and the experiments.

Experiments 2 and 5 were performed without biaxial loading, i.e. only external loading (see Fig. 10). The numerical analysis used in the comparison corresponds to experiment 5 from Table 1. The shape of the curves is very different from those in Figs. 8 and 9. When no internal pressure is introduced, the hoop-stress does not exist, hence resistance against ovalisation is reduced. This will relax the crack zone on the tension side when local buckling occurs on the compressive side of the pipe. At about 4-5% of global bending strain, the pipe suffers from local buckling, and the crack opening stops, thus the crack growth stops, and a structural collapse occurs. This response has earlier been reported from numerical simulations by Østby et al. [17], using 3D solid modelling, and Skallerud et al. [22], using shell and line-spring models. Here the numerical analysis seems to reach the buckling at a somewhat earlier stage than the experiments, hence the $CTOD$-evolution also saturates earlier. It is also here seen a deviation between the experimental curves.

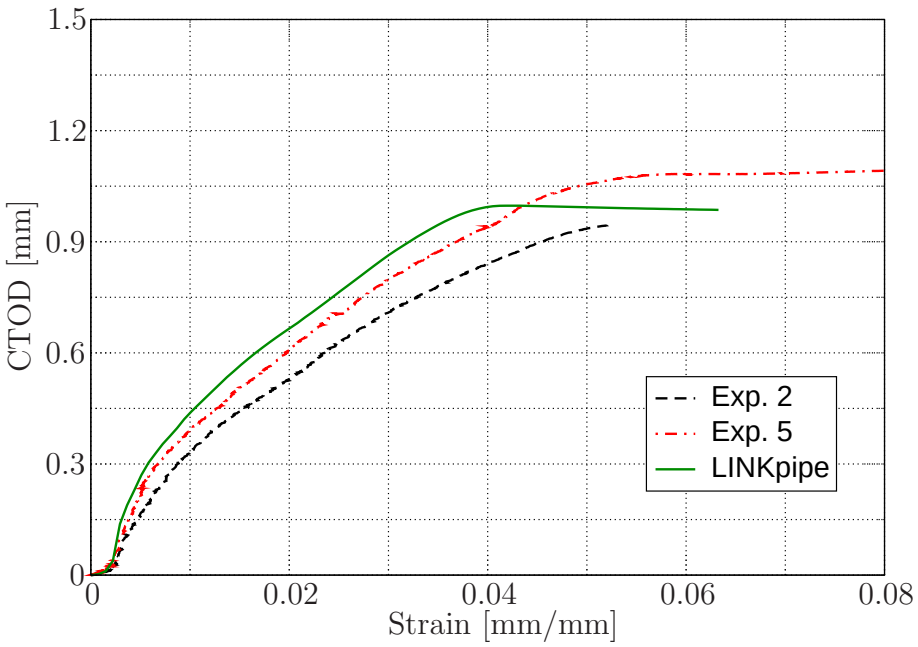

Figure 10: Comparison between large scale tests 2 and 5 and LINK$_{pipe}$ ($p_i = 0MPa$).

6.2 Effect of biaxial loading

In previous work (Shimanuki and Inoue [21]; Jayadevan et al. [8, 9] and Østby et al. [17]) it has been demonstrated that biaxial loading of pipelines reduces the deformation capacity of pipes with defects. Fig. 11 shows that when the internal pressure increases, the global deformation capacity decreases rapidly as the crack grows through the thickness. The case of an internal pressure of $13.5MPa$ gives a hoop stress to yield stress ratio of $\sigma_h/\sigma_{0.2} = 0.25$. If an internal pressure of $32.5MPa$ is present, this ratio increases to $\sigma_h/\sigma_{0.2} = 0.6$. The difference in strain

capacity between the cases with $\sigma_h/\sigma_{0.2} = 0.25$ and 0.6 is smaller than what should be expected from the numerical simulations in the references above. The main reason for this is due to the larger crack depth in the former case compared to the latter (see Table 1).

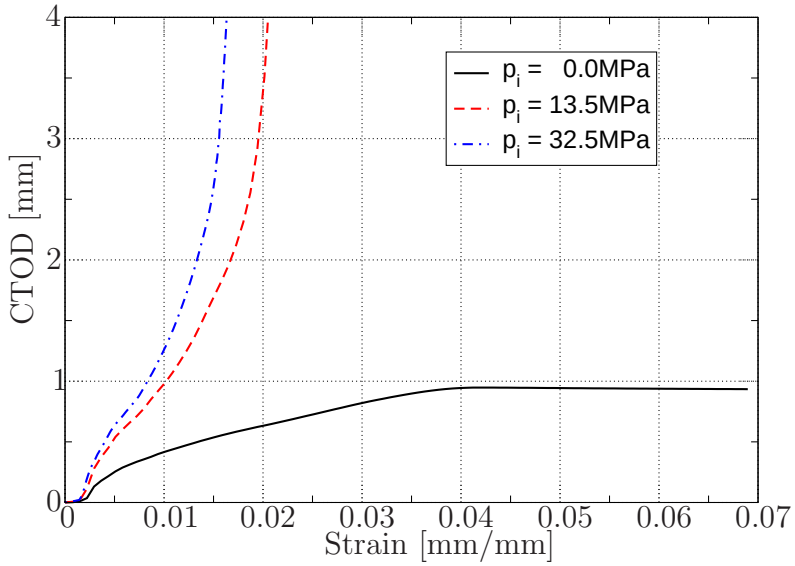

Figure 11: Effect of internal pressure from the numerical analyses.

In Fig. 12 ductile crack growth from experiments are compared with the corresponding numerical analyses for the cases with internal pressure. It is seen that the numerical analyses slightly over-predicts the ductile crack growth for a given strain level. This corresponds to the behaviour observed in Figs. 8 and 9 where the numerical curves are located above the experimental curves. Good agreement between the experimental and numerical values are observed.

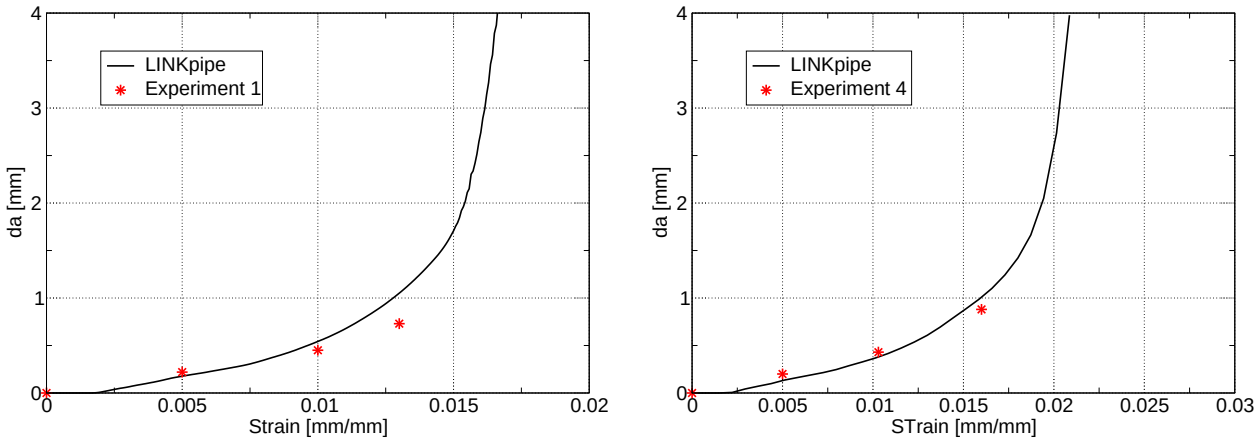

(a) (b)

Figure 12: Comparison of ductile crack growth versus applied strain for (a) experiment 1 and (b) experiment 4.

6.3 Effect of wall thickness

The pipes used in the experiments were seamless, and due to the production method, the wall thickness is not uniform all over. This section addresses the effect of altering the wall thickness within the thickness range observed in the pipe segments tested in this study. Note that the wall thickness is kept constant for each analysis, but for each of the different pressure levels, three different wall thicknesses are employed to see the effect. The crack depth is kept constant for each of the internal pressures, thus the crack depth to wall thickness ratio is varying with the wall thickness. Increasing the wall thickness reduces the crack depth ratio, thus reducing the slope of the strain-$CTOD$ curve.

In Fig. 13, the minimum measured wall thickness of $14.45mm$ is included along with two additional analyses with wall thickness of $15.0mm$ and $15.5mm$, i.e. a maximum increase in wall thickness by $1.05mm$. It is seen in Fig. 13 that increasing the wall thickness by $0.55mm$ gives a curve between the two experimental parallels. Increasing even further, the numerical curve is almost matching the lowest experimental curve.

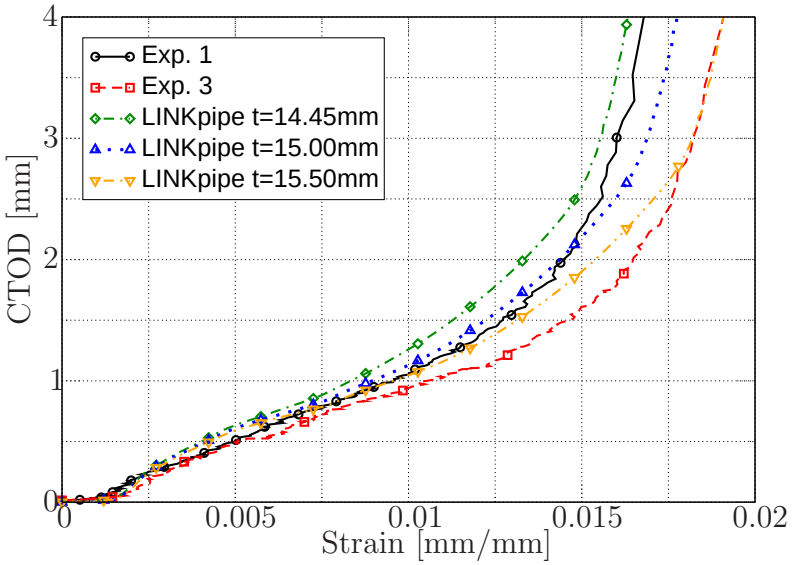

Figure 13: Effect of increasing the wall thickness for tests 1 and 3.

Fig. 14 shows the effect of increasing the wall thickness for the cases with an intermediate internal pressure ($13.5MPa$). The same tendency as for the cases shown in Fig. 13. When increasing the wall thickness by $0.77mm$, the comparison between the numerical response and experiment 4 is very good up to where the unstable crack growth starts. Then the slope of the curve from the numerical analysis is lower than for the experimental curve, thus yielding a slightly higher strain capacity. Although the strain capacity is slightly over-predicted by the largest wall thickness, the comparison between the experimental curves and the numerical analyses is good.

For the cases without biaxial loading, an increase in the wall thickness reduces the $CTOD$ at buckling slightly, but the strain corresponding to onset of buckling is marginally increased (see Fig. 15). When increasing the wall thickness by $0.38mm$, the response is very much equal

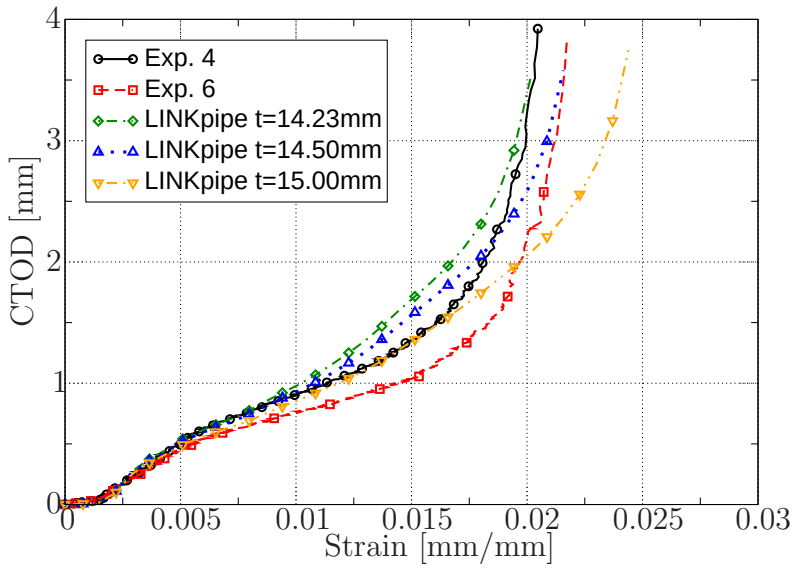

Figure 14: Effect of increasing the wall thickness for tests 4 and 6.

the experimental curve from experiment 5. When increasing the wall thickness by additional $0.5mm$, the response is positioning itself between the two experimental curves.

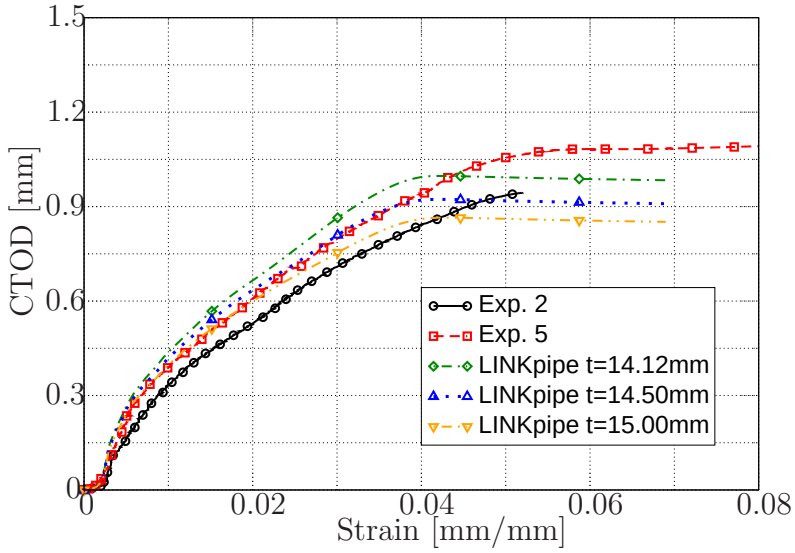

Figure 15: Effect of increasing the wall thickness for tests 2 and 5.

6.4 Effect of yield stress

Variation in a material's stress-strain curve is always expected. In the experiments from the present study, the stress-strain curve was measured at four positions around the circumference for all pipes (Fig. 6). It is seen from the measurements that the yield stress has some variations (standard deviation of $11.4MPa$). As the stress-strain curve is translated up- or downwards

(see Fig. 16) according to the measurements, the relation between the yield stress and the tensile strength will also change. If the curve is translated upwards, the hardening will slightly decrease, and vice versa as manifested as an increase and decrease in the $\sigma_{0.2}/\sigma_{TS}$-ratio. A lower hardening will results in a higher crack driving force as a function of the applied strain.

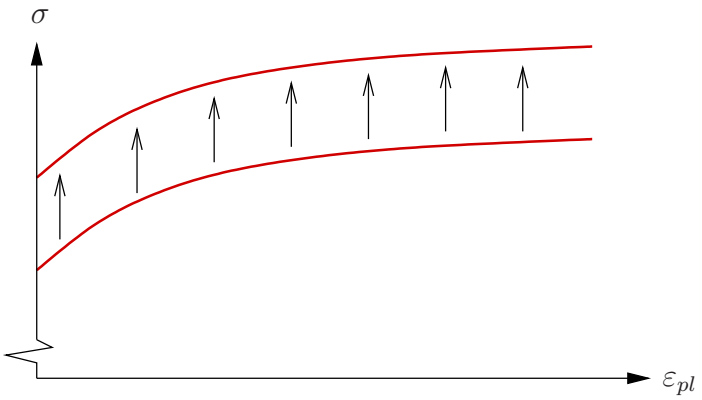

Figure 16: Schematic illustration of translating the material curve upwards.

In the subsequent analyses, the yield stress ($\sigma_{0.2}$) is varied from $466MPa$ to $506MPa$ and covers the whole range from the experiments. The stress-strain curves used in these analyses also corresponds to those shown in Fig. 6. The solid lines in Figs. 17-19 are the reference cases used in the previous comparisons.

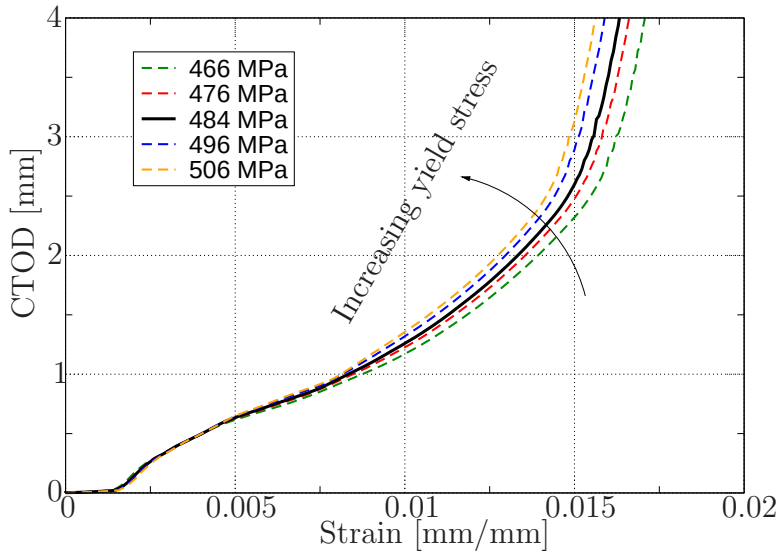

Figure 17: Effect of variation in the yield stress for the case with internal pressure of $p_i = 32.5MPa$.

Fig. 17 shows the effect of varying the yield stress for the case with an internal pressure of $32.5MPa$ ($\sigma_h/\sigma_{0.2} = 0.60$). The difference in the response is minor compared to changing the wall thickness for the same case (see Fig. 13). It is seen that increasing the initial yield stress gives raise to a higher $CTOD$ for the same deformation level.

In Fig. 18, the effect of varying the yield stress is performed for the case with an internal pressure of $13.5MPa$ ($\sigma_h/\sigma_{0.2} = 0.25$). The same trend as for the case with internal pressure of $32.5MPa$ is observed, although the effect is smaller.

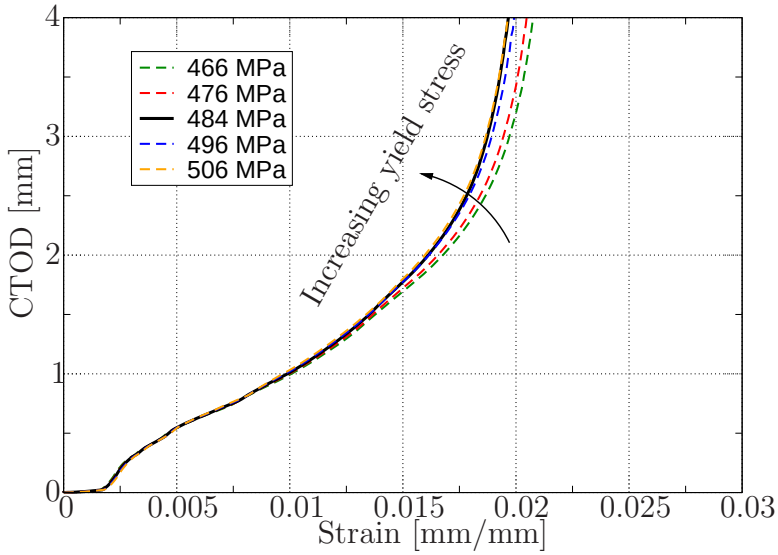

Figure 18: Effect of variation in the yield stress for the case with internal pressure of $p_i = 13.5MPa$.

For the case without internal pressure (Fig. 19), the effect of varying the yield stress is seen similar to the cases with internal pressure.

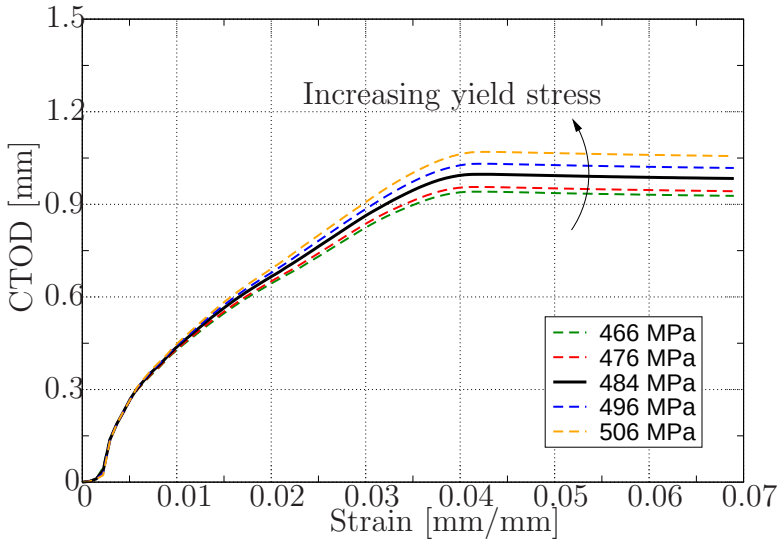

Figure 19: Effect of variation in the yield stress for the case without internal pressure.

7 Pipe capacity - failure criterion

A structure can reach different failure modes. Sandvik et al. [20] presents both a local and global fracture failure criterion. The local failure criterion (proposed by Østby [15]) predicts the $CTOD$ at maximum load in the crack ligament (δ_{max}) as

$$\delta_{max} = (0.03(t-a) + \delta_{\Delta a=1.0mm} - 0.61)\left(12.1\left(\frac{\sigma_{0.2}}{\sigma_{TS}}\right)^2 + 18.9\left(\frac{\sigma_{0.2}}{\sigma_{TS}}\right) - 6.28\right) \quad (1)$$

In Eq. 1, $\delta_{\Delta a=1.0mm}$ is the $CTOD$-level at ductile crack growth of $1.0mm$ (see Fig. 7). The global failure criterion used is based on the maximum applied load. For a problem where the failure mode is fracture, the load will drop when unstable crack growth occurs. The strain at maximum load is then recorded. This failure criterion is very helpful in engineering design. Note that the global and local failure criterion depends on the specific case since the structural response depends on geometry, material and loading conditions.

Fig. 20 shows the critical strain level when using the maximum load criterion, and Fig. 21 shows the critical point for the local failure criterion. In both figures, case 1 in Table 1 is employed.

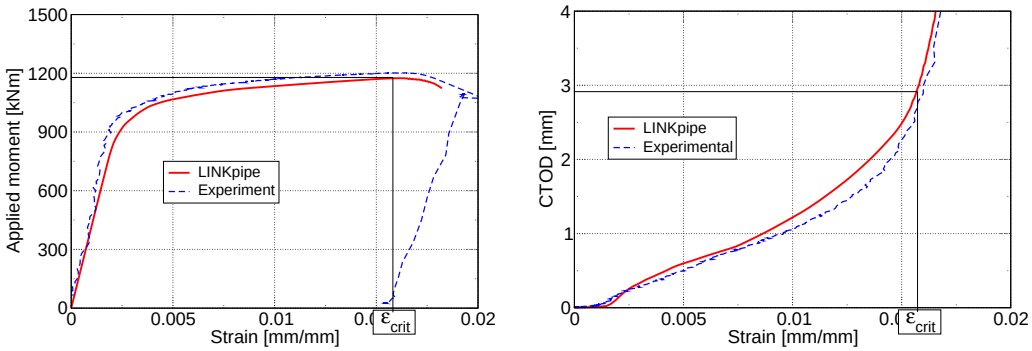

(a) (b)

Figure 20: Failure determined by the maximum load failure criterion. (a) shows the position in the global response, and (b) shows the corresponding point for the local response. The strain capacity, ε_{crit}, is marked in both plots.

It is seen from Figs. 20 and 21 that these two criteria give different results of what to be seen as the critical design point. If the global failure criterion is used, the $CTOD$ in this case is $2.9mm$. The computed ductile crack growth at this stage is $2.0mm$, but it is seen that a small increase in the applied strain will cause the crack to grow faster as the slope of the curve is getting steeper.

For the local failure criterion, the critical $CTOD$ is $1.56mm$ by using Eq. 1. At this $CTOD$-level, the ductile crack growth is $0.4mm$. In this case the maximum load capacity is not reached, and the crack growth is still stable.

It must be noted that a strain based methodology is not well established yet, and should

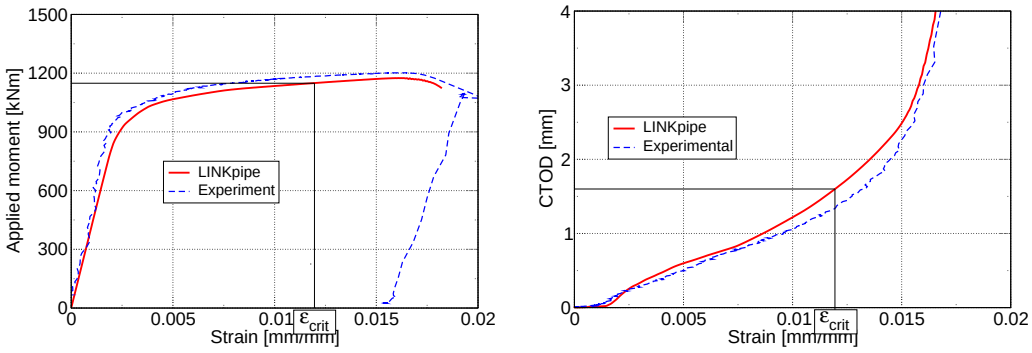

(a) (b)

Figure 21: Failure determined by the local failure criterion. (a) shows the position in the global response, and (b) shows the corresponding point for the local response. The strain capacity, ε_{crit}, is marked in both plots.

therefore be used with caution. More work and validation is required before it is used for industrial purposes.

8 Concluding remarks

The present study compares large scale experiments of pipe segments and numerical results performed with LINK$_{pipe}$. The external applied load was modelled as a pipe subjected to pure bending load. Three different levels of internal pressure are applied ($\sigma_h/\sigma_{0.2}$ = 0.0, 0.25 and 0.60).

The shell and line-spring model well captures the physics observed for bending of pipes with external surface defects. The results are generally in good quantitative correspondence with the results from the large scale testing. The differences observed are to be considered within what could be expected in reality, and lies within what should be assumed as uncertainty in assessment of pipes loaded well into the plastic regime. Thus, the results presented add support to the applicability of the LINK$_{pipe}$ program as a possible tool for fracture assessment of pipelines loaded beyond yielding.

A parametric study on the effect of wall thickness was also performed. For the cases with biaxial loading, a small increase in the wall thickness in the numerical models gave a better comparison than with the minimum nominal measured wall thickness. This is assumed to be a more realistic case since the wall thickness given from the large scale experiments were the minimum measured wall thickness around the circumference. For the case without internal pressure, the comparison between the experiments and the line-spring model is very good for the case with a small increase in the wall thickness (see Fig. 15).

The applied strain at buckling is somewhat higher for the experiments than for the line-spring model. The difference is still acceptable and could be due to possible geometrical variations or the measurement techniques.

The effect of varying the yield stress was also studied for the three levels of internal pressure. For the cases with internal pressure, an increase in the initial yield stress from $484MPa$ to $506MPa$ only slightly reduced the deformation capacity. For the case without internal pressure, an increase of the yield stress from $484MPa$ to $506MPa$ also here increased the $CTOD$ at the same deformation level.

Acknowledgements

The authors want to acknowledge the joint industry project Fracture Control – Offshore Pipelines supported by Statoil, Hydro, Eni Norge, BP, Technip and the Research Council of Norway.

References

[1] Assessment of the integrity of structures containing defects - revision 4, R6, British Energy, 2001.

[2] E. Berg, B. Skallerud, C. Thaulow. Two-parameter fracture mechanics and circumferential crack growth in surface cracked pipelines using line-spring elements. *Engineering Fracture Mechanics*, **75**:17–30, 2008.

[3] H. Bratfors. Use of strain-based ECA for the assessment of flaws in pipeline girth welds subjected to plastic deformation. *In: Proceedings of International Conference on Application an Evaluation of high Grade Linepipe in hostile environments*, pp. 957–985, Yokohama, Japan, 2000.

[4] P. Budden. Failure assessment diagram methods for strain-based fracture. *Engineering Fracture Mechanics*, **73**:537–552, 2006.

[5] M. Chiesa, B. Skallerud, D. Gross. Closed form line spring yield surfaces for deep and shallow cracks: formulation and numerical performance. *Computers and Structures*, **80**:533–545, 2002.

[6] M. Chiesa, B. Skallerud, B. Nyhus. Efficient numerical procedures for fracture assessments of surface cracked shells. *In: Proceeding of European Conference of Computational Mechanics*, Krakow, Poland, 2001.

[7] S. J. Garwood, T. G. Davey, S. L. Creswell. Behaviour of A533B under biaxial loading at +70°C. *International Journal of Pressure Vessels and Piping*, **36**:199–224, 1989.

[8] K. R. Jayadevan, E. Berg, C. Thaulow, E. Østby, B. Skallerud. Numerical investigation of ductile tearing in surface cracked pipes using line-springs. *International Journal of Solids and Structures*, **43**:2378–2397, 2006.

[9] K. R. Jayadevan, E. Østby, C. Thaulow. Fracture response of pipelines subjected to large plastic deformation under tension. *International Journal of Pressure Vessels and Piping*, **81**:771–783, 2004.

[10] H. Lee, D. M. Parks. Fully plastic analyses of plane strain single-edge-cracked specimens subjected to combined tension and bending. *International Journal of Fracture*, **63**:329–349, 1993.

[11] S. Linkens, C. L. Formby, R. A. Ainsworth. A strain-based approach to fracture assessment – example applications. *In: Proceedings of 5th International Conference on Engineering Structural Integrity Assessment*, EMAS 63, 2000.

[12] B. Nyhus, M. P. Loria, O. Ørjasæter. SENT specimens an alternative to SENB specimens for fracture mechanics testing of pipelines. *In: Proceedings of OMAE2003, 22nd International Conference of Offshore Mechanics and Arctic Engineering*, Cancun, Mexico, 2003.

[13] B. Nyhus, E. Østby, H. O. Knagenhjelm, S. Black, P. A. Røstadsand. Experimental studies on the effect of crack depth and asymmetric geometries on the ductile tearing resistance. *In: Proceedings of OMAE2005, 24th International Conference of Offshore Mechanics and Arctic Engineering*, Halkidiki, Greece, 2005.

[14] E. Østby. Fracture control-offshore pipelines – new strain-based fracture mechanics equations including the effect of biaxial loading, mismatch, and misalignment. *In: Proceeding of OMAE2005, 24th International Conference on Offshore Mechanics and Arctic Engineering*. Halkidiki, Greece 2005.

[15] E. Østby. Proposal for a strain-based fracture assessment procedure for offshore pipelines. *In: Proceedings of 17th International Offshore and Polar Engineering Conference*, Lisbon, Portugal, 2007.

[16] E. Østby, A. O. Hellesvik. Fracture control – offshore pipelines JIP, results from large scale testing of the effect of biaxial loading on the strain capacity of pipes with defects. *In: Proceedings of 17th International Offshore and Polar Engineering Conference*, Lisbon, Portugal, 2007.

[17] E. Østby, K. R. Jayadevan, C. Thaulow. Fracture response of pipelines subject to large plastic deformation under bending. *International Journal of Pressure Vessels and Piping*, **82**:201–215, 2005.

[18] J. R. Rice. The line spring model for surface flaws, *The Surface Crack: Physical Problems and Computational Solutions*, Edited by J. L. Swedlow. New York: American Society of Mechanical Engineers, pp. 171–185, 1972.

[19] J. R. Rice, N. Levy. The part-through surface crack in an elastic plate. *Journal of Applied Mechanics*, **39**:185–194, 1972.

[20] A. Sandvik, E. Østby, C. Thaulow. A probabilistic fracture mechanics model including 3D ductile tearing of bi-axially loaded pipes with surface cracks. *Engineering Fracture Mechanics*, **75**:76–96, 2008.

[21] H. Shimanuki, T. Inoue. Assessment of brittle fracture in girth weld joint of pipelines subjected to internal pressure and bending load. *In: Proceedings International Conference on the application and evaluation high grade linepipes in hostile environments*, Yokohama, Japan.

[22] B. Skallerud, E. Berg, K. R. Jayadevan. Two-parameter fracture assessment of surface cracked cylindrical shells during collapse. *Engineering Fracture Mechanics*, **73**:264–282, 2005.

[23] B. Skallerud, K. Holthe, B. Haugen. Thin shell and surface crack finite elements for simulation of combined failure modes. *Computer Methods in Applied Mechanics and Engineering*, **194**:2619–2640, 2005.

[24] C. Thaulow, B. Skallerud, K. Holthe, E. Berg, E. Østby, B. Nyhus, J. Ødegård. Fracture control of pipelines using LINKpipe: From rule based design to direct calculations. *In: Proceedings of HSLP-IA2006: International seminar on Application of High Strength Line Pipe and Integrity Assessment of Pipeline*, Xi'an, People's Republic of China, 2006.

[25] L. Vitali, R. Bruschi, K. Mørk, E. Levold, R. Verley. Hotpipe project – capacity of pipes subject to internal pressure, axial force and bending moment. *In: Proceedings of 9th International Offshore and Polar Engineering Conference*, France, 1999.

[26] Y.-Y. Wang, M. Liu, D. Horsley, J. Zhou. A quantitative approach to tensile strain capacity of pipelines. *In: Proceedings of IPC2006, 6th International Pipeline Conference*, Calgary, Alberta, Canada, 2006.

[27] C. S. White, D. M. Parks. Elastic-plastic line-spring finite elements for surface-cracked plates and shells. *Journal of Pressure Vessel Technology*, **104**:287–292, 1982.

PAPER IV

Cyclic plasticity modelling for ANDES thin shell and line-spring finite elements

E. Berg, K. Holthe, B. Skallerud

International Journal of Applied Mechanics, **1***(1):201–232*, 2009.

Cyclic plasticity modelling for ANDES thin shell and line-spring finite elements

E. Berg[1], K. Holthe[1], B. Skallerud[1]

[1]Department of Structural Engineering, Norwegian University of Science and Technology, N-7491 Trondheim, Norway

ABSTRACT

This paper presents a proposed methodology to account for cyclic plastic response of the thin shell ANDES and line-spring finite elements. A through thickness integration scheme is employed for the shell element and stress resultant plasticity is used for the line-spring element. A simplified contact formulation to account for crack closure in the line-spring element is also presented. Numerical comparisons between the proposed models and detailed 3D analyses (pipes) are carried out and presented herein. A comparison between the present implementation and large scale experiment of a surface cracked pipe subjected to large cyclic plastic strains is also presented. The purpose of the presented implementation is to account for cyclic loading in pipeline technology where significant amount of plasticity in the loading cycles occurs.

Keywords: kinematic hardening; thin shell; line-spring; low cycle fatigue; crack growth

1 Introduction

During the installation phase of offshore pipelines, the pipeline is subjected to severe cyclic plastic strains. One method used for installing pipelines is the reeling method. In reeling, pipe segments are welded together on land before reeled to a spool on a ship. The winded pipe has both large tensile and large compressive plastic strains. When the pipeline is to be un-reeled from the ship, the stress state is reversed in order to straighten the pipe. When the pipe touches the sea-bed, another load cycle takes place. If a defect is detected, the un-reeling must be reversed in order to repair the defect and another load cycle will affect the material.

After installation, the operation phase starts. During the operation, a number of start-ups and shutdowns are taking place. These occurrences give raise to a significantly larger stress state

than during normal operation. If the start-ups and shutdowns also lead to plastic behaviour in the material, it is vital to carry out a low cycle fatigue assessment. Pipelines in seismic unstable regions where earthquakes are likely to occur may also experience severe cyclic plastic strains.

During its lifetime, the pipeline is subjected to fatigue loading. Most of the time it is subjected to high cycle fatigue where the nominal loads cause elastic behaviour and the stress intensity factor, K_I, characterises the near-tip stress field. Some parts of the lifetime are met by low cycle fatigue, typically with tens or hundreds of load cycles to failure. In low cycle fatigue K_I is invalidated, but Dowling and Begley [9] introduced the cyclic J-integral as a measure of the near-tip stress field where nominal plasticity is occurring. For the parts of the lifetime where large plastic strains are present, the fatigue behaviour is a so called "*very low cycle fatigue*" or "*tearing fatigue*". This behaviour is not supposed to occur during operation phase. Large plastic strains are mainly a focus during the installation phase. For a discussion of interaction between low cycle fatigue and ductile tearing, see Skallerud and Zhang [30, 31].

For constructions subjected to cyclic plasticity, a kinematic strain hardening material model should be selected. The two classical kinematic hardening rules are the translation rules by Prager [24] and Ziegler [34]. Ziegler showed that the Prager model was not invariant when the dimensions of the stress space were reduced. For cases with plane stress or plane strain the Ziegler model is therefore more favourable.

The methodology of using a kinematic hardening model with more than one yield or memory surface has reached large popularity over the last decades. There are in principle two classes of these models. The first one is the so called bounding surface models. These models consists of two surfaces with one active surface and one bounding surface. The bounding surface is an isotropically expanded surface accounting for the maximum plastic domain for the analysis or it can translate according to kinematic hardening. The two surfaces can come into contact, but they can not intersect. The active surface is the boundary of the elastic domain. Alternatively the bounding surface can be a memory surface where the active surface and the bounding surface are identical at the initial load state. When loading occurs, the active surface translates and the bounding surface expands isotropically or translates. Examples of two-surface models are developed and presented by Krieg [13], Dafalias and Popov [7], Tseng and Lee [32] and Skallerud [27].

The second class is the multi-surface models, often named Mróz-like models after Mróz [19]. Many variants and refinements of the method have been proposed by numerous authors. Some recent implementations are presented by Caminero and Montáns [5], Khoei and Jamali [12] and Owolabi and Singh [23]. The multi-surface models use the point-wise stress-strain curve as input which make these models very attractive for the user of a finite element program. Each surface will then have a size corresponding to the stress level from the stress-strain curve. The number of surfaces will be identical to the number of points on the input stress-strain curve. The plastic modulus between two surfaces is determined as the slope of the stress-strain curve for the given segment.

A potential feature for nonlinear or multi-linear kinematic hardening models is to preserve the Masing's rule [17], [16]. This defines the stress-strain behaviour for reversed plasticity. A single or two-surface model does not have the Masing's rule inherited like the multi-surface

kinematic hardening models. Some effort must be put into the implementation to make the model behave according to the Masing's rule. The Masing's rule then makes the single or two-surface models somewhat more complex. The analytical non-linear kinematic translation rule presented by Lemaitre and Chaboche [16] and implemented in ABAQUS [1] has the Masing's rule inherited. It must be noted that the Masing's rule is an assumption where the hysteresis loop is a homothetic transformation of factor 2 with respect to the monotonic stress-strain curve. Many materials have a cyclic behaviour approximate to the Masing's rule, but the Masing's rule does not fit for all metallic materials.

The shell finite element used in the present study is rectangular thin shell ANDES element in a co-rotated formulation. This shell element was initially proposed by Felippa and Militello [10] and later extended to account for large rotations and inelasticity by Skallerud and Haugen [28]. The line-spring finite element used in fracture mechanics was proposed by Rice and Levy [25] and further extended by Parks and White [33] and Lee and Parks [14, 15]. Further information about the current implementation of the line-spring element can be found in Skallerud et al. [29] and Berg et al. [2, 3]. In the implementations of the shell and line-spring finite elements from the above references, only isotropic hardening was accounted for. This paper extends the material implementation to account for cyclic plasticity as well as presenting a methodology to account for tearing fatigue and crack closure for the line-spring finite element. Cyclic ageing, hardening or softening are not considered in this model.

The implementation presented in this paper makes use of the monotonic stress-strain curve as user input, hence no other material parameters need to be identified by the user prior to analysis.

2 Numerical implementation

The software LINK$_{pipe}$ is used in the present study [28, 29]. Four-noded thin shell ANDES finite elements and non-linear line-spring finite elements are used. In [28, 29] both the shell element and the line-spring element made use of isotropic hardening stress resultant plasticity. In the current study, the material models for these elements have been extended to account for kinematic hardening. The following sections describes the implementation of non-linear kinematic hardening models for both the shell and the line-spring finite element.

2.1 Kinematic hardening for shell element

In the present implementation, the material model is based on through thickness integration following the Lobatto quadrature. The Ziegler translation rule is used for a single yield surface. The memory is accounted for by keeping track of the maximum stress level experienced on the stress-strain curve. An approximation to the Masing's rule is preserved by storing the stress level from both tension and compression for each reversed loading. This makes the present model quite similar to a two surface model where the boundary surface acts as a memory surface.

Stress update in the integration points

A fully implicit backward Euler stress update algorithm with the Ziegler kinematic hardening rule [26] is implemented and used in this study. The uni-axial monotonic stress-strain curve is used as input for the stress update. The curve is transmitted as points (plastic strain versus true stress). The present implementation makes use of the Ziegler hardening rule for a non-linear stress-strain curve. Since the non-linear curve is presented as a point-wise curve, linear segments are used between the points, hence a modified Ziegler kinematic hardening rule with the Masing's rule can be used.

A plane stress situation is assumed in each layer through the thickness, thus the stress space is reduced from 3D to 2D where all stress components σ_{i3} and σ_{3j} from the stress tensor vanish. The yield function is shown in Eq. 1.

$$f = \underbrace{\sqrt{\tilde{\sigma}_x^2 + \tilde{\sigma}_y^2 - \tilde{\sigma}_x\tilde{\sigma}_y + 3\tilde{\tau}_{xy}^2}}_{\sigma_e} - \sigma_0 = 0 \tag{1}$$

where $\tilde{\sigma}$ is the normalised stress component expressed as $\tilde{\sigma} = \sigma - \alpha$. α is the kinematic back-stress vector and σ_e is the effective von Mises stress.

The consistent tangent stiffness matrix is expressed in matrix notation as

$$\mathbf{C}_{ct} = \left[\mathbf{R} - \frac{\left(\mathbf{n}^T\mathbf{R}\right)^T\left(\mathbf{n}^T\mathbf{R}\right)}{\mathbf{n}^T\mathbf{R}\mathbf{n} + \hat{H}}\right] \tag{2}$$

$$\mathbf{R} = \left[\mathbf{C}^{-1} + \Delta\lambda\frac{\partial\mathbf{n}}{\partial\boldsymbol{\sigma}}\right]^{-1} \tag{3}$$

where $\mathbf{n}$ is the normal vector to the yield surface (first derivative of the yield function). $\hat{H}$ is the current slope of the stress-strain curve, $\mathbf{C}$ is the elastic stiffness matrix and $\Delta\lambda$ is the plastic multiplier. The derivations of the consistent tangent stiffness matrix for a plane stress situation with a von Mises material can be found in the literature, e.g. Crisfield [6] and Simo and Hughes [26].

A Masing-like formulation to handle load reversals

The present formulation uses a pointwise stress-strain curve which is linear between the points. To be able to perfectly handle Masing's rule for a pointwise (piecewise linear) stress-strain curve a multi-surface formulation is needed. However, the present kinematic hardening model makes use of a single surface formulation, thus Masing's rule is not completely obtained. In order to make an approximation of the Masing's rule a set of conditions are presented in the following.

The Masing's rule for a stable half cycle is displayed in Fig. 1. The segments on the part AB form the virgin uniaxial stress-strain curve. The segments on part CD corresponds to the segments in part AB. The slope of each segment on part CD equals the corresponding ones from part AB, but the length of the segments on part CD is twice the length of the segments on AB.

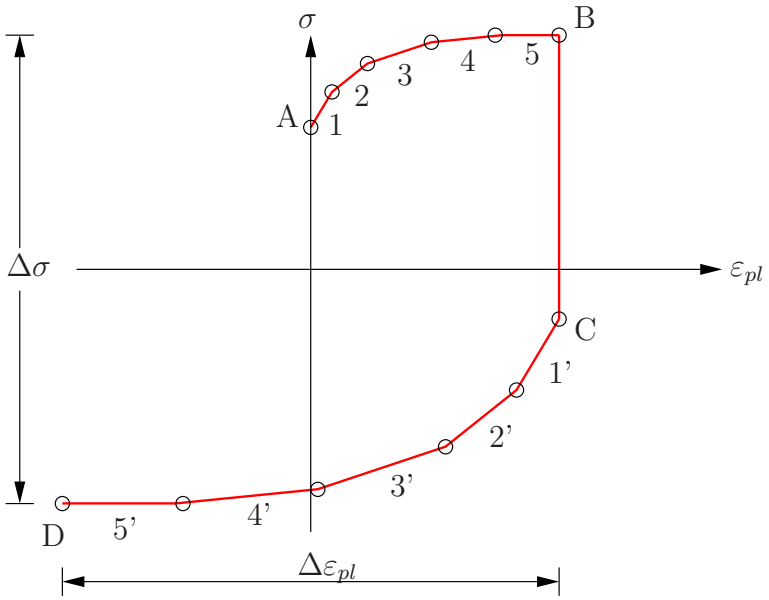

Figure 1: Schematic view of the Masing's rule for a point-wise stress-strain curve

Dowling [8] presents a set of rules for the reversed stress-strain behaviour. Each time the plastic load reverses in an integration point, the line segments of the stress-strain curve are used in ascending order starting with the first. If a segment (or part of) was used in the previous loading but not in the current, they must be skipped in the next reversed loading. With this in mind, the history effects are taken into account. Also the segments of the stress-strain curve should only be used once with its original length. If a segment is used later in the load sequence, the segments should be of double length corresponding to Fig. 1.

With these rules taken into account, a set of conditions are implemented in the present finite element code. It must be noted that the present formulation does not perfectly satisfy Masing's rule for all load sequences, but for the current applications of pipeline installation and operation phase the accuracy of the presented formulation is acceptable.

A set of internal variables handling the positions on the stress-strain curve are used to keep control of the different load cycles. Also the point on the stress-strain curve with the highest stress level ever experienced in the load sequence is recorded to know when to use the virgin curve (part AB on Fig. 1) and when to use the reversed (double) curve (part CD on Fig. 1).

The unloading point on the stress-strain curve from the previous tensile part of the loading cycle as well as the current position is recorded. The same recording is done for the compressive part of the loading cycle. Using these quantities, it is possible to determine if some segments (or part of) should be skipped in the following part of the loading cycle or the next loading cycle. The pseudo code in Alg. 1 together with Fig. 2 show how the handling of the cyclic stress-strain curve is implemented for a case where the first yielding was tensile. The implementation handles both initial tensile and compressive yielding. Fig. 2 shows an example of a loading sequence. The symbols in the pseudo code in Alg. 1 corresponds to Fig. 2.

In Alg. 1, the following symbols are used to track the position on the stress-strain curve.

Algorithm 1 Handle position on stress-strain curve for cyclic loading

if plastic → elastic **then**
  if tensile plastic → elastic **then**
    $\xi_{comp}^{last} = \xi_{comp}^{cur}$
    $\xi_{comp}^{cur} = 0$
  else {compressive plastic → elastic}
    $\xi_{tens}^{last} = \xi_{tens}^{cur}$
    $\xi_{tens}^{cur} = 0$
  end if
else {plastic → plastic}
  if $\xi^{cur}/2 > \psi_{max}$ **then**
    use monotonic (virgin) stress-strain curve
    $\psi^{max} = \xi^{cur}$
    clear all history
    Continue to accumulate the current plastic strain and position on the virgin stress-strain curve (part AB in Fig. 1)
  else
    use reverse stress-strain curve (part CD in Fig. 1)
  end if

  if compressive plastic behaviour **then**
    if $\xi_{comp}^{cur} < \xi_{tens}^{last}$ **then**
      Proceed and accumulate ξ_{comp}^{cur}
    else $\{\xi_{comp}^{cur} = \xi_{tens}^{last}\}$
      Skip part of stress-strain curve which lies between ξ_{comp}^{cur} and ξ_{tens}^{last}
      $\xi_{comp}^{cur} = \xi_{comp}^{last}$
    end if
  else {Tensile plastic behaviour}
    if $\xi_{tens}^{cur} < \xi_{tens}^{last}$ **then**
      Proceed and accumulate ξ_{tens}^{cur}
    else $\{\xi_{tens}^{cur} = \xi_{comp}^{last}\}$
      Skip part of stress-strain curve which lies between ξ_{tens}^{cur} and ξ_{comp}^{last}
      $\xi_{tens}^{cur} = \xi_{comp}^{last}$
    end if
  end if
end if

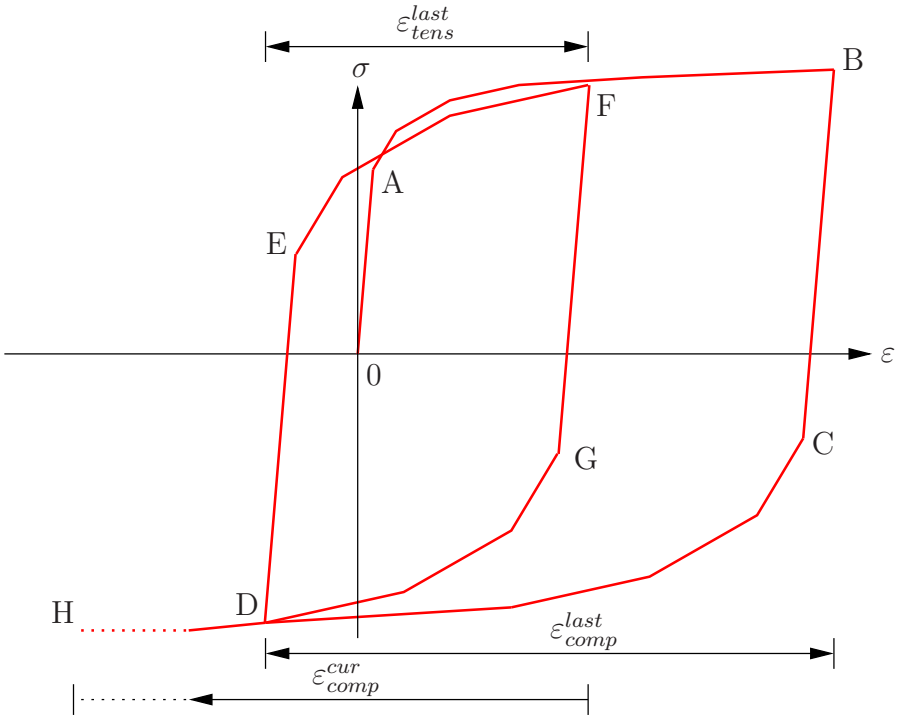

Figure 2: Example of a loading sequence with the load path $0-A-B-C-D-E-F-G-H$

ψ defines the position on the virgin stress-strain curve giving the largest stress value ever experienced in the analysis. ξ is the current position on the reversed stress-strain curve.

Alg. 1 and Fig. 2 are here explained using a uniaxial tension/compression bar. The initial loading, OAB in Fig. 2, will follow the virgin stress-strain curve. At point B the load is reversed and line 1–4 in Alg. 1 are executed. At this first reversal, the parameter ξ^{last}_{comp} is already zero. From point C the uniaxial bar undergoes plastic compression. This compressive loading is active until point D. From point C to D the reversed part of the stress-strain curve is used. As mentioned, the reversed stress-strain curve is a homothetic transformation of the monotonic stress-strain curve with a factor of 2, hence the position on the reversed stress-strain curve that corresponds to the position on the virgin stress-strain curve must be divided by 2 to determine the correct slope of the stress-strain curve. The part of Alg. 1 starting at line 18 is to be executed. ξ^{tens}_{last} is here equal ψ_{max}, and ξ^{cur}_{comp} will not exceed ξ^{tens}_{last}, hence ξ^{cur}_{comp} is to be accumulated as described in line 20 in Alg. 1.

At point D in Fig. 2 the load on the uniaxial bar is again reversed to tension. Now $\varepsilon^{last}_{comp}$ in Fig. 2 is converted to position ξ^{last}_{comp} on the monotonic stress-strain curve and stored for later use. In line 5–8 in Alg. 1 the parameter ξ^{last}_{tens} is initialised, and at point E in Fig. 2 the plastic tension loading starts from the initial point on the reversed stress-strain curve. During this loading the lines 25–31 in Alg. 1 are processed. For this example the position on the stress-strain curve will not exceed the maximum position from the previous compressive loading (BCD in Fig. 2) or the initial loading ($0AB$ in Fig. 2), thus ξ^{cur}_{tens} is accumulated according to the lines 26–27 in Alg. 1. At point F on Fig. 2 the load is again reversed to a compressive load state. First elastic unloading occurs (lines 2–4 in Alg. 1). Plastic compressive loading starts at point G. Here

the position on the stress-strain curve is initialised and further accumulated as the deformation compresses. During this compressive loading the position on the stress-strain curve is monitored to see if ξ_{comp}^{cur} exceeds ψ_{max} or ξ_{tens}^{last}. In this example, ξ_{comp}^{cur} equals ξ_{tens}^{last} at point D in Fig. 2. Lines 21–23 in Alg. 1 now cause the parameter ξ_{comp}^{cur} to be set equal ξ_{comp}^{last}, thus the parts of the stress-strain curve between ξ_{tens}^{last} and ξ_{comp}^{last} will be skipped. If this compressive loading continues and cause the parameter ξ_{comp}^{cur} to exceed the position ψ_{max}, the virgin stress-strain curve will be used.

Through the thickness integration method

The Lobatto quadrature [18] was chosen as a numerical integration scheme to perform through the thickness integration in order to include the outer fibres. Values for the abscissas and weight functions are tabulated in the code. The numerical integral can be expressed as shown in Eq. 4.

$$\int_{-1}^{1} f(z)dz = w_1 f(-1) + w_n f(1) + \sum_{i=2}^{n-1} w_i f(z_i) = \sum_{i=1}^{n} w_i f(z_i) \tag{4}$$

where z_i are the positions of the integration points in Lobatto quadrature (abscissas), w_i are the weights for the corresponding abscissas and n is the number of integration points through the thickness. $f(z_i)$ are the stress values for the given positions. The integrated stress components from each layer gives the stress resultants as expressed in Eq. 5.

$$\mathbf{N} = \left(\frac{t}{2}\right) \sum_{i=1}^{n} w_i \boldsymbol{\sigma}_i \qquad \mathbf{M} = \left(\frac{t}{2}\right)^2 \sum_{i=1}^{n} w_i z_i \boldsymbol{\sigma}_i \tag{5}$$

where t is the shell thickness. The constitutive equation system in the "stress resultant space" is expressed as

$$\begin{Bmatrix} d\mathbf{N} \\ d\mathbf{M} \end{Bmatrix} = \underbrace{\begin{bmatrix} \mathbf{K}_{NN} & \mathbf{K}_{MN} \\ \mathbf{K}_{NM} & \mathbf{K}_{MM} \end{bmatrix}}_{\mathbf{K}} \begin{Bmatrix} d\boldsymbol{\varepsilon}^0 \\ d\boldsymbol{\kappa}^0 \end{Bmatrix} \tag{6}$$

The sub-matrices in $\mathbf{K}$ in Eq. 6 are symmetric. The integrated consistent tangent stiffness matrix, $\mathbf{K}$, becomes

$$\begin{bmatrix} dN_x \\ dN_y \\ dN_{xy} \\ dM_x \\ dM_y \\ dM_{xy} \end{bmatrix} = \underbrace{\begin{bmatrix} A_{11} & A_{12} & A_{13} & B_{11} & B_{12} & B_{13} \\ A_{12} & A_{22} & A_{23} & B_{21} & B_{22} & B_{23} \\ A_{13} & A_{23} & A_{33} & B_{31} & B_{32} & B_{33} \\ B_{11} & B_{21} & B_{31} & D_{11} & D_{12} & D_{13} \\ B_{12} & B_{22} & B_{32} & D_{12} & D_{22} & D_{23} \\ B_{13} & B_{23} & B_{33} & D_{13} & D_{23} & D_{33} \end{bmatrix}}_{\mathbf{K}} \begin{bmatrix} d\varepsilon_x \\ d\varepsilon_y \\ d\gamma_{xy} \\ d\kappa_x \\ d\kappa_y \\ d\kappa_{xy} \end{bmatrix} \tag{7}$$

where

$$A_{kj} = \left(\frac{t}{2}\right) \sum_{i=1}^{n} w_i C_{kj}^i \tag{8}$$

$$B_{kj} = \left(\frac{t}{2}\right)^2 \sum_{i=1}^{n} w_i z_i C_{kj}^i \tag{9}$$

$$D_{kj} = \left(\frac{t}{2}\right)^3 \sum_{i=1}^{n} w_i z_i^2 C_{kj}^i \tag{10}$$

where C_{ij}^k are the stiffness matrices from the through thickness integration points. The stresses and stiffness matrices for each layer are integrated to form the stress resultants (see Eq. 5) and an equivalent stiffness matrix (see Eq. 7). The stress resultants and the equivalent stiffness matrix are transmitted back to the main program.

2.2 Kinematic hardening for the line-spring element

The line-spring yield surface for monotonic loading is based on 2D plane strain analyses published by Parks and co authors [14],[33] and further refined by Skallerud et al. [29] and Berg et al. [3]. The line-spring element is based on stress resultants and the yield surface is a point-wise curve depending on the crack depth to thickness ratio and yield stress (depending on equivalent plastic strain) presented by Parks and White [33]. A refinement by expanding the table was performed by Berg et al. [4]. The points forming the yield surface is ensuring a convex formulation satisfying Drücker's convexity postulate. The shape of the yield surface makes it very difficult to establish a single mathematical function expressing the curve. For crack depth to thickness ratios not tabulated, a linear interpolation between the tabulated line segments are used. A collection of tabulated yield surfaces is seen in Fig. 3.

The presented methodology can be used in many cases where the yield surface can not be described by a function but is described by linear segments between points. An issue which demands focus is that a point-wise curve consists of a lot of corners (discontinuities of the normal vector), which might lead to numerical challenges due to a non-unique normal vector in the points. The corner points must therefore be handled specifically as shown in Fig. 4.

The technique to handle corners in the current implementation is a pragmatic solution where the direction and the length of the normal vector for a point is the mean direction based on the two intersecting line segments.

Implementation of the kinematic hardening line-spring material model

The previous line-spring element implementation was based on incremental isotropic hardening where the yield surface expands according to the equivalent plastic strain. The new implementation makes use of a Ziegler-like kinematic translation rule in addition to the already existing isotropic hardening model. The stiffness matrix is a relation between the generalised

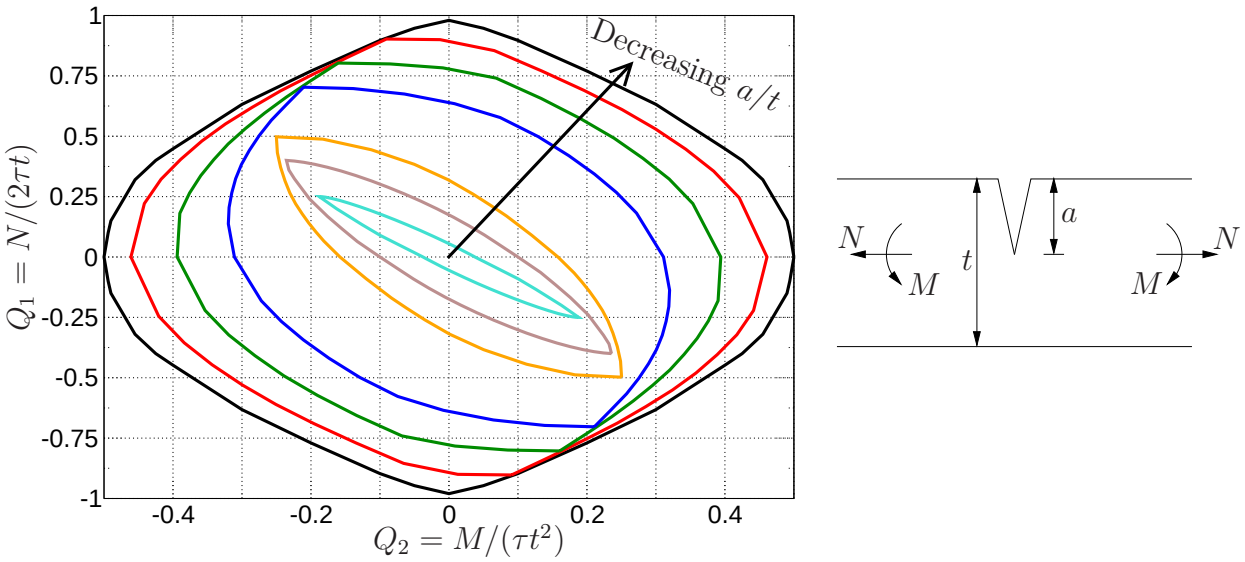

Figure 3: A collection of tabulated yield surfaces for the line-spring finite element

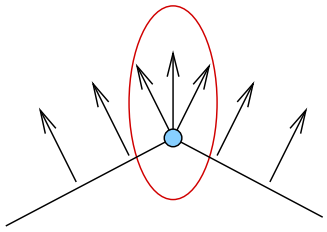

Figure 4: Non-unique normal vector in a point

displacements (elongation and rotation), and the generalised forces (membrane force and bending moment).

In the following, the generalised forces, $\mathbf{Q}$, the back stress vector, $\mathbf{X}$, and the elastic stiffness matrix, $\mathbf{C}$, in the line-spring element are normalised according to the axes definitions in Fig. 3. Considering a line segment from point number P_2 to P_3 on the pointwise yield surface as shown in Fig. 5 where the normalised stress resultant vector from last equilibrium is denoted $\tilde{\mathbf{Q}}_0$. The vector, $\mathbf{n}$, orthogonal to line segment $P_2 - P_3$ in Fig. 5 is defined as

$$\mathbf{n} = \frac{1}{S}\begin{bmatrix} \tilde{Q}_{1,P3} - \tilde{Q}_{1,P2} \\ -(\tilde{Q}_{2,P3} - \tilde{Q}_{2,P2}) \end{bmatrix} = \frac{1}{S}\mathbf{b} \tag{11}$$

$$S = \tilde{Q}_{2,P2} \cdot \tilde{Q}_{1,P3} - \tilde{Q}_{2,P3} \cdot \tilde{Q}_{1,P2} \tag{12}$$

where S is twice the area of the stapled, shaded triangle in Fig. 5. Note that $\mathbf{n}$ is not a unit vector. The yield function can be expressed as the product of the normalised stress resultant vector, $\tilde{\mathbf{Q}} = \mathbf{Q} - \mathbf{X}$, and the normal vector, $\mathbf{n}$, as

$$f^n = \mathbf{n}^T(\mathbf{Q}^n - \mathbf{X}^n) - 1 = 0 \tag{13}$$

The superscript n denotes configuration from last equilibrium.

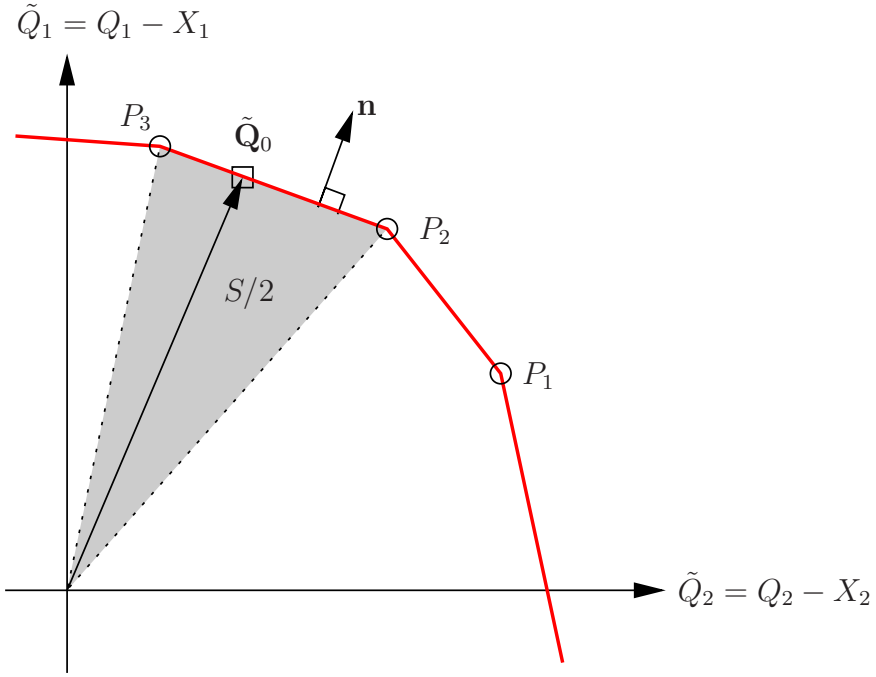

Figure 5: Definitions for the normal vector to a line segment

In a load increment the yield surface is first expanded isotropically (see Fig. 7b) and then translated according to the back stress vector (Fig. 7c). Fig. 6 shows schematically both the numerical expansion and the translation of the yield surface for the proposed kinematic hardening model.

The modified yield function for the isotropically expanded yield surface now reads

$$\tilde{f}^{n+1} = (\mathbf{n}^{n+1})^T(\mathbf{Q}^{n+1} - \mathbf{X}^n) - \left(\frac{\Delta\sigma^{n+1}}{\sigma_0} + 1\right) = 0 \tag{14}$$

where σ^{n+1} is the updated stress level, σ^n is the stress level from last equilibrium and σ_0 is the yield stress. The trial point is expressed as

$$\mathbf{Q}^{tr} = \mathbf{Q}^n + \mathbf{C}_{el}\Delta\mathbf{q} \tag{15}$$

where $\mathbf{C}_{el}$ is the elastic stiffness matrix and $\Delta\mathbf{q}$ are the normalised generalised displacements. The flow rule reads

$$\Delta\mathbf{q}_{pl} = \Delta\lambda\mathbf{n}^{n+1} \tag{16}$$

A plastic work equation for the line-spring element was proposed by Lee and Parks [15] and is expressed as shown in Eq. 17 for combined hardening.

$$(\mathbf{Q}^{n+1} - \mathbf{X}^{n+1})^T\Delta\mathbf{q}_{pl} = k \cdot \left(1 - \frac{a}{t}\right)^2 \sigma_0\Delta\varepsilon_{pl} = A \cdot \Delta\varepsilon_{pl} \tag{17}$$

where k is dimensionless scalar which Lee and Parks [15] named *the strain hardening factor* and $\Delta\varepsilon_{pl}$ is the equivalent plastic strain. Now combining Eqs. 16 and 17, the plastic multiplier is expressed as

$$\Delta\lambda = A \cdot \Delta\varepsilon_{pl} \tag{18}$$

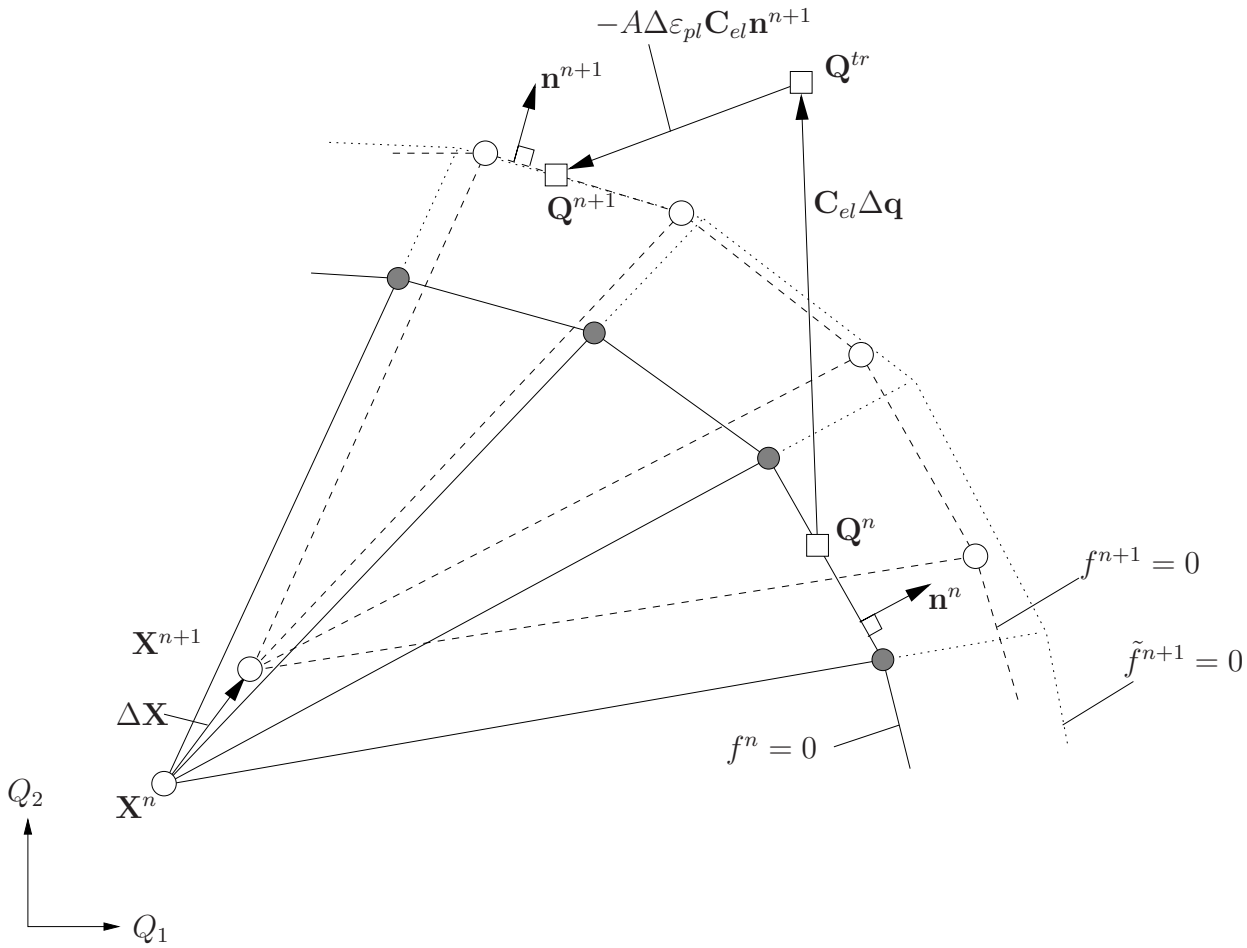

Figure 6: Proposed kinematic translation rule for line-spring element

Combining Eqs. 15 and 16 the updated stress resultants at the end of the load increment reads

$$\begin{aligned}\mathbf{Q}^{n+1} &= \mathbf{Q}^{n}+\mathbf{C}_{el}\Delta\mathbf{q}_{el}^{n+1}\\ &= \mathbf{Q}^{n}+\mathbf{C}_{el}\Delta\mathbf{q}^{n+1}-\mathbf{C}_{el}\Delta\mathbf{q}_{pl}^{n+1}\\ &= \mathbf{Q}^{tr}-A\Delta\varepsilon_{pl}\mathbf{C}_{el}\mathbf{n}^{n+1}\end{aligned} \tag{19}$$

Premultiplying Eq. 19 with the normal vector of the yield surface and combining with the updated yield function (Eq. 14), the result is

$$A\Delta\varepsilon_{pl}\left(\mathbf{n}^{n+1}\right)^{T}\mathbf{C}_{el}\mathbf{n}^{n+1}+\left(\frac{\Delta\sigma^{n+1}}{\sigma_0}+1\right)=\left(\mathbf{n}^{n+1}\right)^{T}\left(\mathbf{Q}^{tr}-\mathbf{X}^{n}\right) \tag{20}$$

Solving Eq. 20 for equivalent plastic strain, a Newton-Raphson iteration process is used. The iteration stops when the expression $\left|\Delta\varepsilon_{pl}^{(i+1)}-\Delta\varepsilon_{pl}^{(i)}\right|$ is less than some tolerance. The quantity i is here the local iteration number.

Now the updated stress resultant point is located on the isotropically expanded yield surface (dashed surface on Fig. 7b). The updated back stress vector is defined as the difference vector

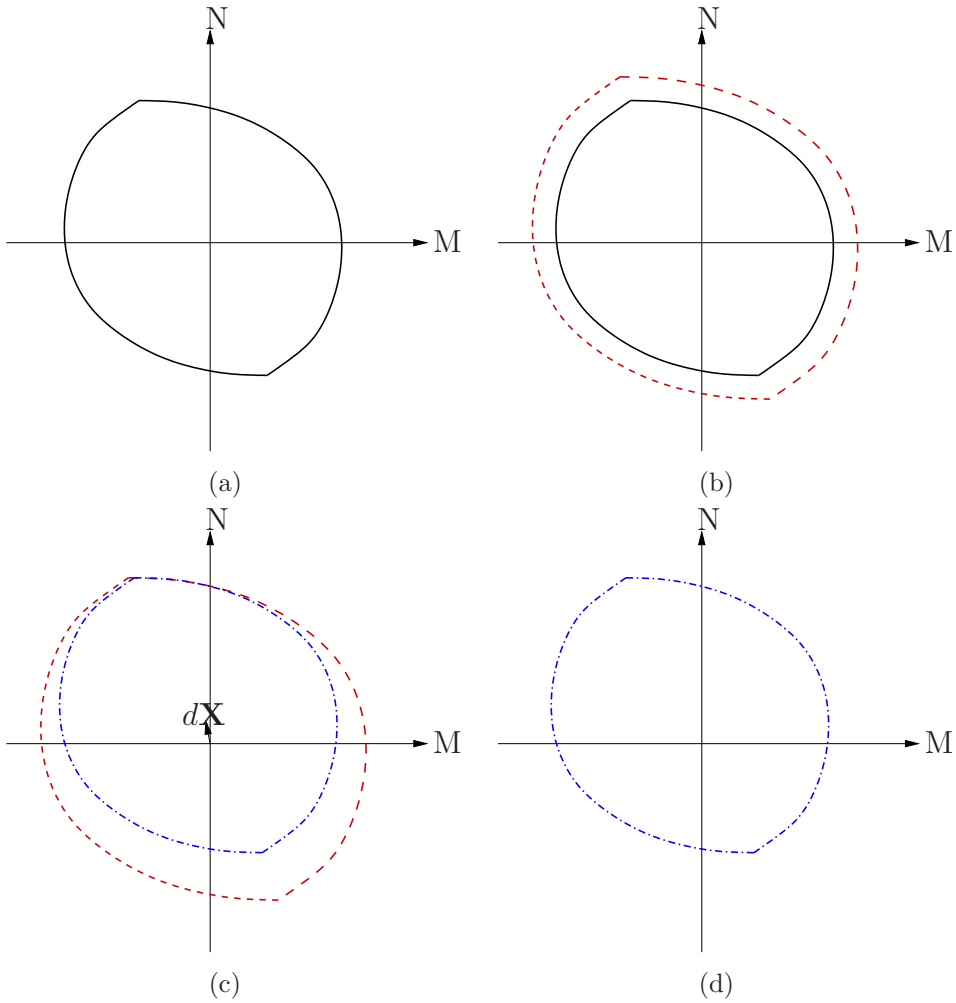

Figure 7: (a) Initial yield surface followed by (b) an incremental isotropic expansion due to hardening. The initial yield surface (c) is translated according to the method shown in Fig. 6, thus the yield surface position at the end of the load increment is shown in (d).

between the updated stress resultant point and the back stress from last equilibrium as shown in Eq. 21.

$$\Delta\mathbf{X} = \Delta\beta\left(\mathbf{Q}^{n+1} - \mathbf{X}^{n}\right) \tag{21}$$

where $\Delta\beta$ is still an unknown scalar. Premultiplication with $\mathbf{n}^{n+1}$ in Eq. 21 and inserting into yield function (Eq. 14) Eq. 21 is transformed to

$$\left(\mathbf{n}^{n+1}\right)^{T}\Delta\mathbf{X} = \Delta\beta\left(\mathbf{n}^{n+1}\right)^{T}\left(\mathbf{Q}^{n+1} - \mathbf{X}^{n}\right) = \Delta\beta\left(\frac{\Delta\sigma^{n+1}}{\sigma_0} + 1\right) \tag{22}$$

The yield function for the updated yield surface (Fig. 7c) is zero at the end of the stress update, and is now expressed as

$$f^{n+1} = \left(\mathbf{n}^{n+1}\right)^{T}\left(\mathbf{Q}^{n+1} - \mathbf{X}^{n+1}\right) - 1 = 0 \tag{23}$$

Combining Eqs. 14 and 23 gives

$$\begin{aligned}\left(\mathbf{n}^{n+1}\right)^T\left(\mathbf{Q}^{n+1}-\mathbf{X}^{n+1}\right)-1 &= \left(\mathbf{n}^{n+1}\right)^T\left(\mathbf{Q}^{n+1}-\mathbf{X}^{n}\right)-\left(\tfrac{\Delta\sigma^{n+1}}{\sigma_0}+1\right)\\ \Rightarrow \left(\mathbf{n}^{n+1}\right)^T\left(\mathbf{X}^{n+1}-\mathbf{X}^{n}\right) &= \tfrac{\Delta\sigma^{n+1}}{\sigma_0}\\ \Rightarrow \left(\mathbf{n}^{n+1}\right)^T\Delta\mathbf{X} &= \tfrac{\Delta\sigma^{n+1}}{\sigma_0}\end{aligned} \tag{24}$$

Now inserting Eq. 24 into Eq. 21, the scalar $\Delta\beta$ is expressed as

$$\Delta\beta = \frac{\Delta\sigma^{n+1}}{\Delta\sigma^{n+1}+\sigma_0} \tag{25}$$

Using the result from Eq. 25, the updated back stress vector for the line-spring element is expressed as

$$\begin{aligned}\mathbf{X}^{n+1} &= \mathbf{X}^{n}+\Delta\mathbf{X}\\ &= \mathbf{X}^{n}+\Delta\beta\left(\mathbf{Q}^{n+1}-\mathbf{X}^{n}\right)\end{aligned} \tag{26}$$

When the updated stress point and the updated back stress vector is found, the incremental elastic-plastic stiffness relation is found by introducing the consistency condition and applying the result from Eq. 16 as shown in the following.

The incremental stress resultant change, $\Delta\mathbf{Q}$ is expressed as

$$\Delta\mathbf{Q} = \mathbf{C}_{el}\Delta\mathbf{q}_{el} \tag{27}$$

where $\Delta\mathbf{q}_{el} = \Delta\mathbf{q} - \Delta\mathbf{q}_{pl}$ and $\Delta\mathbf{q}_{pl}$ is found from the flow rule in Eq. 16. Differentiation of Eq. 27 gives the infinitesimal stress resultant change as

$$d\mathbf{Q} = \mathbf{C}_{el}d\mathbf{q} - d\lambda\mathbf{C}_{el}\mathbf{n}^{n+1} - \Delta\lambda\mathbf{C}_{el}\frac{\partial\mathbf{n}}{\partial\mathbf{Q}}d\mathbf{Q} \tag{28}$$

Since the yield function is linear between two points, the second derivative vanishes, hence the infinitesimal stress resultant change can be expressed as

$$d\mathbf{Q} = \mathbf{C}_{el}d\mathbf{q} - d\lambda\mathbf{C}_{el}\mathbf{n}^{n+1} \tag{29}$$

The consistency condition based on the modified yield surface (Eq. 14) reads

$$\left(\mathbf{n}^{n+1}\right)^T d\mathbf{Q} - \frac{1}{\sigma_0}\frac{\partial\sigma}{\partial\varepsilon_{pl}}d\varepsilon_{pl} = 0 \tag{30}$$

where $\partial\sigma/\partial\varepsilon_{pl}$ is the current slope of the stress-strain curve. Combining the consistency condition and the infinitesimal stress change from Eq. 29, the incremental line-spring tangent stiffness matrix is written as

$$\begin{aligned}d\mathbf{Q} &= \mathbf{C}_{ct}d\mathbf{q}\\ &= \left[\mathbf{C}_{el} - \frac{\left(\mathbf{n}^T\mathbf{C}_{el}\right)^T\left(\mathbf{n}^T\mathbf{C}_{el}\right)}{\mathbf{n}^T\mathbf{C}_{el}\mathbf{n} + \frac{\partial\sigma}{\partial\varepsilon_{pl}}\frac{1}{\sigma_0 k\cdot\left(1-\frac{a}{t}\right)^2}}\right]d\mathbf{q}\end{aligned} \tag{31}$$

Masing's rule is accounted for in the line-spring element using the method presented in Sec. 2.1.

Crack growth is accounted for by employing the crack growth resistance curve. As seen from Fig. 3, the yield surface for a deep crack is smaller than the yield surface for a shallower crack. When the crack grows, the yield surface shrinks and rotates.

The crack growth resistance curve is on the form as shown in Eq. 32. The yield surface, f, is then expressed as in Eq. 33.

$$\begin{aligned} \delta &= C_1 \left(\Delta a\right)^{C_2} && (32) \\ \Rightarrow \quad f &= f\left(\frac{a+\Delta a}{t}, \mathbf{Q}, \varepsilon_{pl}\right) && (33) \end{aligned}$$

where δ is the crack tip opening displacement calculated from the line-spring displacement and rotation. This is presented in detail by Berg et al. [3]. The crack growth resistance curve used in the input file comes from experiments or from damage mechanics analyses, e.g. the Gurson model.

2.3 Contact formulation - crack closure

The concept of crack closure is challenging to manage. Here a simple methodology to account for crack closure for the line-spring element is presented.

To avoid material merging at the location of the crack mouth, an elastic spring with very large stiffness is used (see Fig. 8a). When the crack mouth points from each crack face get in contact due to reversed loading, the spring is activated to avoid further relative displacement. The same methodology is used to prevent material crossing in the cracked ligament. An elastic spring is positioned at mid-ligament position (see Fig. 8b). These springs will be a contribution to the stiffness matrix in the integration point as expressed in Eq. 34. The expression of the stiffness matrix of the springs are relative to the centre-line of the thickness, thus eccentric terms in the stiffness matrices occur as shown in the two last matrices in Eq. 34. Fig. 8 shows the location of the two springs.

$$\begin{aligned} k_s &= \alpha \frac{Ea}{l} \\ \mathbf{K} &= \mathbf{K}_{mat} + \mathbf{K}_{s,bend} + \mathbf{K}_{s,tens} \\ \begin{bmatrix} K_{11} & K_{12} \\ K_{21} & K_{22} \end{bmatrix} &= \begin{bmatrix} K_{11}^{mat} & K_{12}^{mat} \\ K_{21}^{mat} & K_{22}^{mat} \end{bmatrix} + \begin{bmatrix} k_s & d_{bend} \cdot k_s \\ d_{bend} \cdot k_s & d_{bend}^2 \cdot k_s \end{bmatrix} + \begin{bmatrix} k_s & -d_{tens} \cdot k_s \\ -d_{tens} \cdot k_s & d_{tens}^2 \cdot k_s \end{bmatrix} \end{aligned} \quad (34)$$

where α is a high value scalar, e.g. 10^7, to ensure sufficient high axial stiffness. E is the Young's modulus for the material, a is the crack depth and l is the axial length of the spring (small number). d_{tens} is the distance from the spring to the centre line of the thickness. For the temporary spring for bending situation, the value of d_{bend} is $(t-a)/2$. The terms K_{ij}^{mat} in Eq. 34 are the terms from the tangent stiffness matrix in Eq. 31.

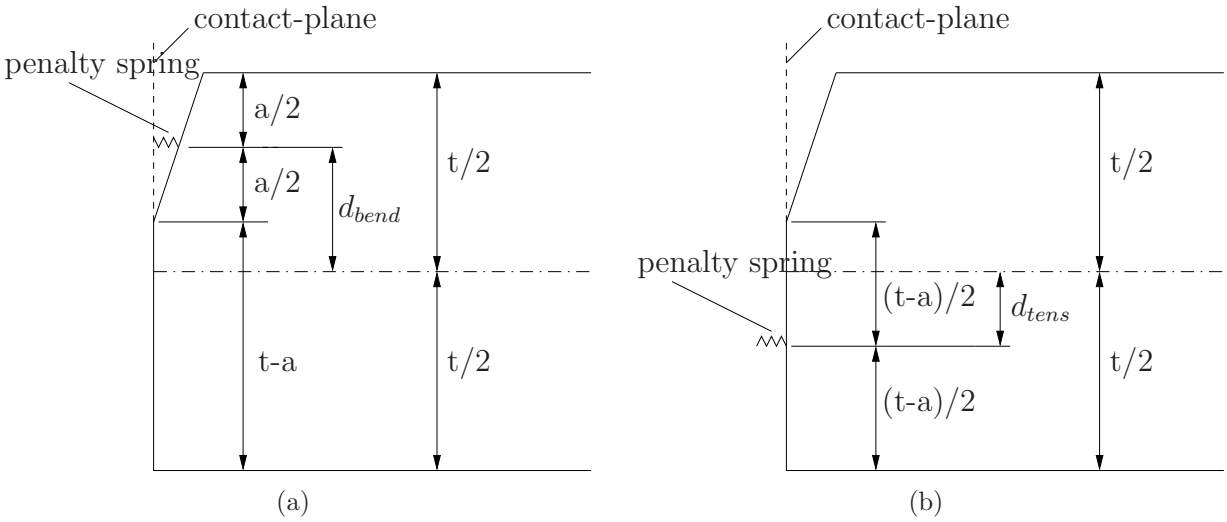

Figure 8: Schematic views of the high stiffness elastic contact springs illustrated for an open crack for (a) bending and (b) tensile situations

The high stiffness elastic spring introduced in membrane situations is similar to the one in bending situations. The main difference lies in the measure for when the spring should be activated, i.e. when the crack faces are in contact. The axial elongation of the line-spring element is used as a measure. When the axial elongation is reduced back to zero due to compressive loading, the elastic spring is activated. The formulation is equal to the formulation of the spring at bending situation. The eccentricity quantity, d_{tens}, is equal to half the crack depth, $a/2$. Fig. 8b shows the location of the spring.

When the crack faces are not in contact, the springs shown in Fig. 8 are not active. The springs are activated separately when they satisfy the contact conditions expressed in Eq. 35.

$$k_{s,bend} = \begin{cases} k_s & v_{bend} \leq 0 \\ 0 & v_{bend} > 0 \end{cases} \quad , \quad k_{s,tens} = \begin{cases} k_s & v_{tens} \leq 0 \\ 0 & v_{tens} > 0 \end{cases} \tag{35}$$

where v_{bend} and v_{tens} are expressed in Eq. 36.

$$v_{bend} = \Delta + \frac{t-a}{t}\theta \quad , \quad v_{tens} = \Delta - \frac{a}{2}\theta \tag{36}$$

where Δ and θ are the accumulated generalised line-spring displacement and rotation in the integration point.

2.4 Fatigue tearing

Ductile crack growth or tearing is accounted for by employing the crack growth resistance curve. When the crack opens the tearing is computed from the crack growth resistance curve. The crack closes when the local load is reversed. When the distance between the crack faces is reduced, the crack tip opening displacement also decreases and the crack does not grow.

When the crack faces come into contact, the crack is closed and the springs from Fig. 8 become active to prevent material crossing. When the load again reverses the crack starts to open again.

It is assumed that the crack depth has increased according to the accumulated tearing from the last crack opening. Fig. 9a shows one load cycle with indications of where crack opening occurs and how the crack depth update is handled. Fig. 9b shows an example of a crack growth resistance curve where the tearing intervals are marked.

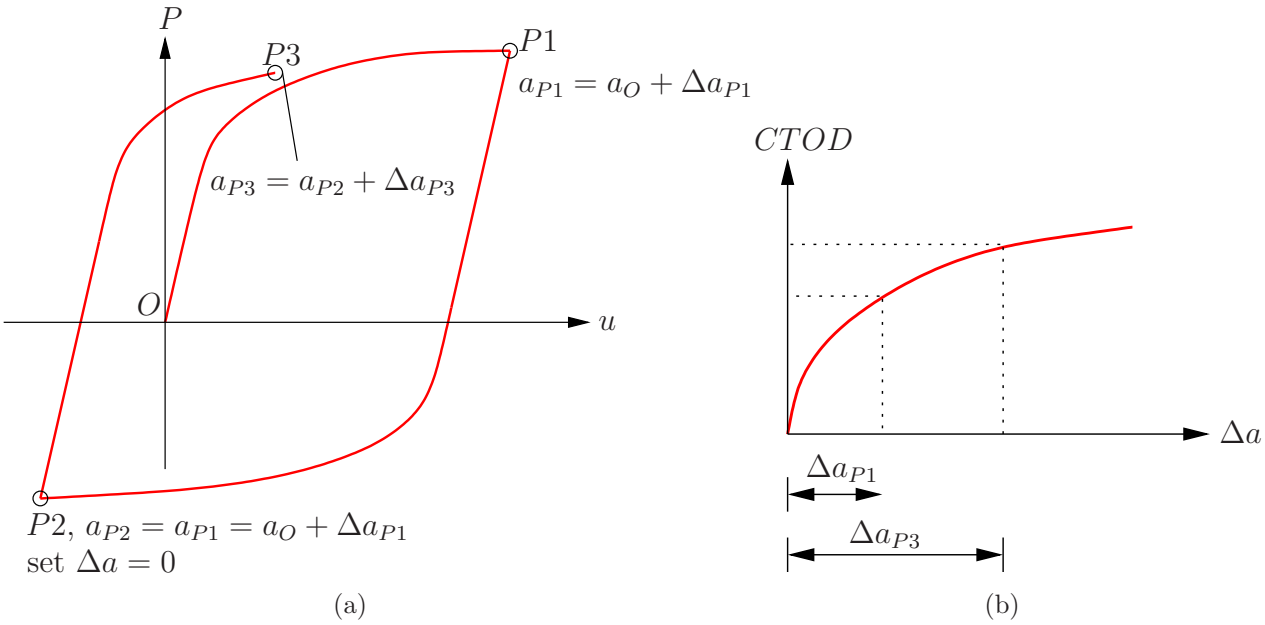

Figure 9: (a) an example of a load cycle with ductile tearing and (b) a crack growth resistance curve with tearing contributions from the load cycle in (a) are marked

In the example in Fig. 9a, the initial crack depth is a_O. At point $P1$, the crack growth is Δa_{P1} as marked on Fig. 9b. The load is reversed at $P1$. During the unloading sequence, the crack is gradually closing and no further tearing occurs. When the compressive load is completed (point $P2$ in Fig. 9a), the crack depth is updated as $a_{P2} = a_O + \Delta a_{P1}$ and the ductile tearing is set as zero. When the opening load from $P2$ to $P3$ starts, the crack growth starts at zero on the crack growth resistance curve in Fig. 9b. At load completion (point $P3$ on Fig. 9a) the ductile crack growth from point $P2$ to $P3$ is marked as Δa_{P3} on Fig. 9b. If now the load is again reversed, the updating procedure is repeated.

3 Modelling aspects

3.1 Material properties

The material used in this study for numerical comparisons between LINK_{pipe} and ABAQUS corresponds to an X65 construction steel with a yield strength of $460MPa$. The Young's

modulus is $200.000MPa$ and Poisson's ratio equals 0.3. The material curve used as input to LINK_{pipe} is shown in Fig. 10.

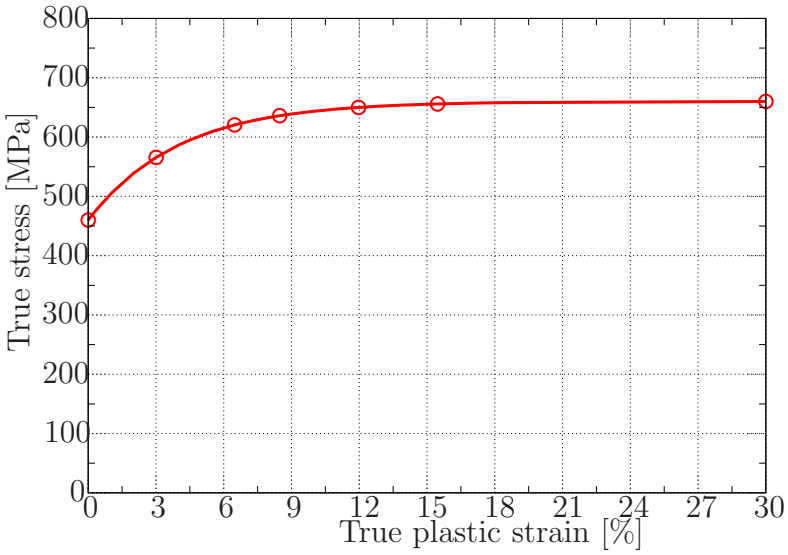

Figure 10: Plastic strain versus true stress for the material used in the following comparisons. Some points on the curve are marked with circle

The kinematic hardening model chosen in ABAQUS [1] uses the expression for the back-stress presented by Lemaitre and Chaboche [16] as shown in Eq. 37 for constant temperature.

$$d\boldsymbol{\alpha} = \frac{C}{\sigma_0} d\varepsilon_{pl} \left(\boldsymbol{\sigma} - \boldsymbol{\alpha}\right) - \gamma \boldsymbol{\alpha} d\varepsilon_{pl} \tag{37}$$

where C and γ are two fitting parameters for this material model. The first term in Eq. 37 gives a linear behaviour (original Ziegler), and the second recall term gives the non-linearity. The values of the fitting parameters are chosen to capture the monotonic stress-strain curve as accurately as possible. The parameters are chosen as $C = 5500MPa$ and $\gamma = 25$. σ_0 is also here $460MPa$.

For the experimental comparison of a surface cracked pipe subjected to cyclic bending loading, the stress-strain curve shown in Fig. 11 was obtained from the pipe material as presented by Nyhus et al. [20].

For the ductile crack growth behaviour the monotonic crack growth resistance curve from multiple single edge notched tension (SENT) specimens shown in Fig. 12 as reported by Nyhus et al. [20] is used.

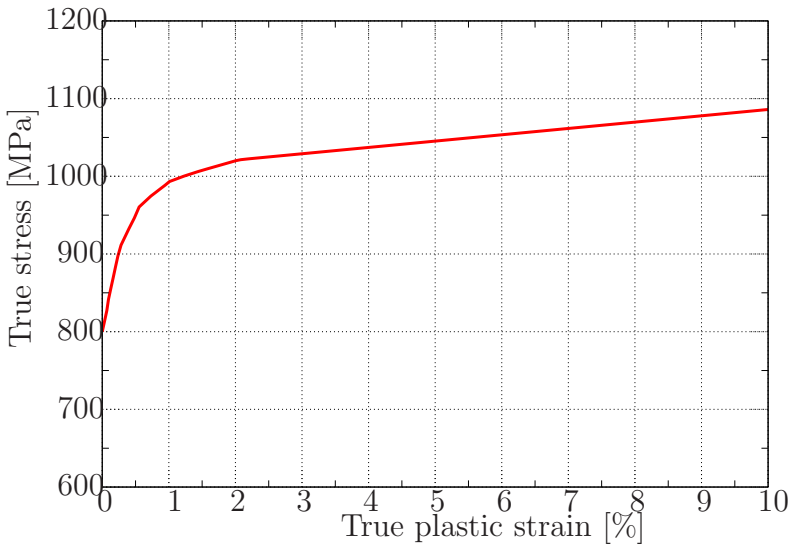

Figure 11: Monotonic stress strain curve from the experiment of a surface cracked pipe subjected to global bending loading (from Nyhus et al. [20])

3.2 Geometry, FE-properties and loading conditions

Un-cracked pipe

A selection of un-cracked pipes is employed first to verify the proposed kinematic hardening model for the shell element. The mesh used in LINK$_{pipe}$ is shown in Fig. 13a and the corresponding model for ABAQUS is shown in Fig. 13b. The outer diameter, D and wall thickness, t of the pipe are taken as $400mm$ and $20mm$ respectively. The total length, $2L$, of the pipe segments was chosen to be six times the outer diameter. The ABAQUS-models use twenty noded brick elements with reduced integration (C3D20R) as element type. The models contain 200 elements and approximately 3800 degrees of freedom. The corresponding models in LINK$_{pipe}$ consists of 144 ANDES elements and approximately 900 degrees of freedom. The number of Lobatto integration points through the thickness is 7.

Four load cases are considered. The first two cases are pipe segments subjected to cyclic tensile loading where one of them is preceded by an internal pressure giving a hoop stress of 20% of the yield stress. The other pipe segment is subjected to a pure cyclic tensile loading. The two last load cases are pipe segments subjected to a cyclic bending loading. One of the bending cases is preceded by the same internal pressure as the tensile one.

For the cases with an internal pressure, the pressure is fully introduced initially, and the external deformation (tensile or bending) is applied when the desired pressure level is reached. For the tensile cases, the end surface is translated in the global Z-direction. For the bending cases, a constraint between the nodes at the end surface and a centre node is applied to achieve end rotation in both the LINK$_{pipe}$ and the ABAQUS analyses. For the models in LINK$_{pipe}$ such a constraint is always performed when doing pipe analyses.

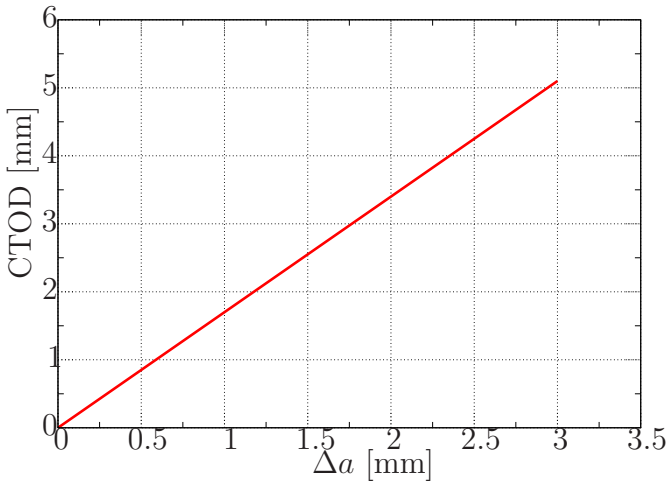

Figure 12: Crack growth resistance curve from Nyhus et al. [20]

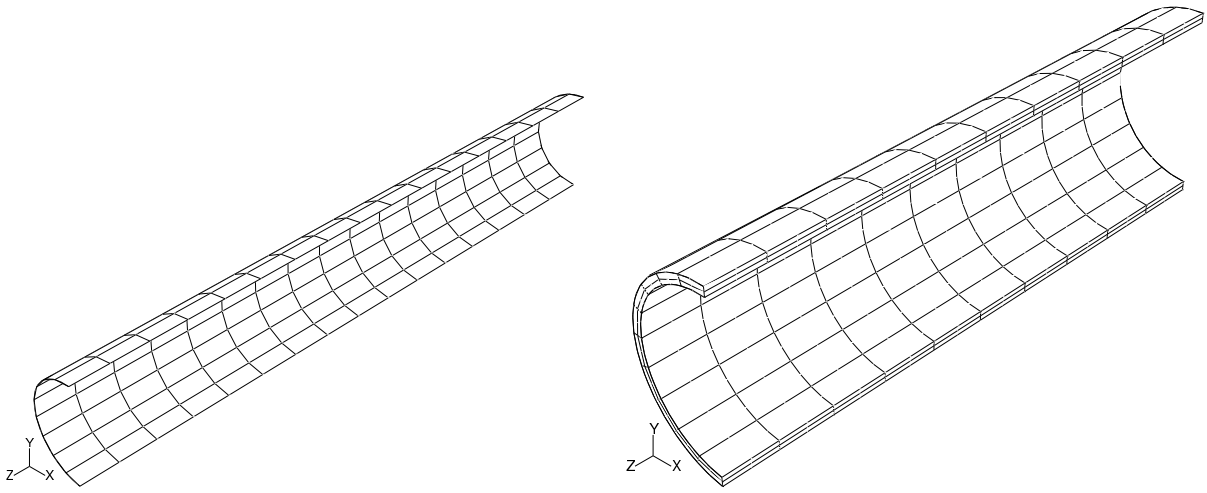

(a) (b)

Figure 13: (a) model analysed with LINK$_{pipe}$ and (b) model analysed with ABAQUS

Surface cracked pipe

The ABAQUS-models with a surface crack are more complicated to create as a very refined mesh at the crack zone is needed. The mesh distant from the crack zone is relatively little affected by the loading, thus a coarse mesh is chosen there. The number of degrees of freedom is about 38000. The corresponding pipe in LINK$_{pipe}$ has about 6500 degrees of freedom. A stationary crack, i.e. no crack growth, is assumed in these analyses, thus the coarse mesh surrounding the crack tip is sufficient to achieve reliable results. The crack geometries are crack depth to thickness ratios of 0.2 and 0.3 and the crack length to circumference is 0.1,

For the comparison width the large scale experiment only analysis performed with LINK$_{pipe}$ has been carried out. The outer diameter of the pipe was $325mm$ and the nominal wall thickness was $15.3mm$. The crack length (2c) is $60mm$ and the initial crack depth is $4.0mm$ ($a/t = 0.26$).

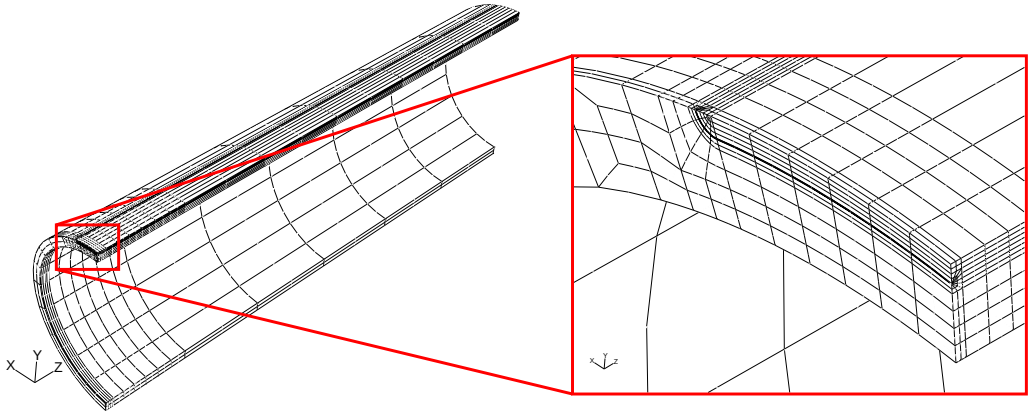

Figure 14: Example of a finite element mesh used for modelling a surface cracked pipe for the ABAQUS analyses

The length of the numerical pipe model is six times the outer diameter. Details about the experimental setup is described by Nyhus et al. [20].

4 Results and discussion

First, the results from the comparisons between pipes analysed with LINK$_{pipe}$ and ABAQUS are presented. Both tension and bending loads are presented along with the effect of internal pressure. Second, a section with comparison between the present model and large scale experiment is presented.

In the result presented here, the model in LINK$_{pipe}$ makes use of the stress-strain curve as direct input, and few material parameters must be fitted prior to the analyses. In general data from material testing must be filtered to ensure a monotonic increase in stress level from one point to the next.

4.1 Pipe models without surface flaw

In this section, the results obtained from LINK$_{pipe}$ are compared with 3D analyses performed with ABAQUS. For the tensile cases, the global tensile reaction force versus applied displacement is compared, and for the bending analyses, the global reaction bending moment versus applied end rotation is compared. The results are displayed in Fig. 15.

In Fig. 15a a pipe subjected to pure tensile loading went through a load cycle with initial tensile loading followed by a complete reversed compressive loading, and finally a fully reversed tensile loading. For the initial tensile load step, the two models follows very well. This can also be used as a verification of the input parameters in the kinematic hardening model used in ABAQUS. In the following reversed load step (compressive), the models are deformed from 2% nominal tension strain to 2% nominal compression strain. It is observed that the global response from

the 3D model is positioned slightly below the model from LINK$_{pipe}$. When the compressive load step is completed, the difference between the models is about 2%. It is worth mentioning that for the LINK$_{pipe}$ analysis the absolute value of the force at the end of the compressive load step equals the value at the end of the initial tensile load step. For the 3D analysis, the absolute value at the end of the compressive load step is somewhat larger than the one at the end of the initial tensile load step. The differences are however small.

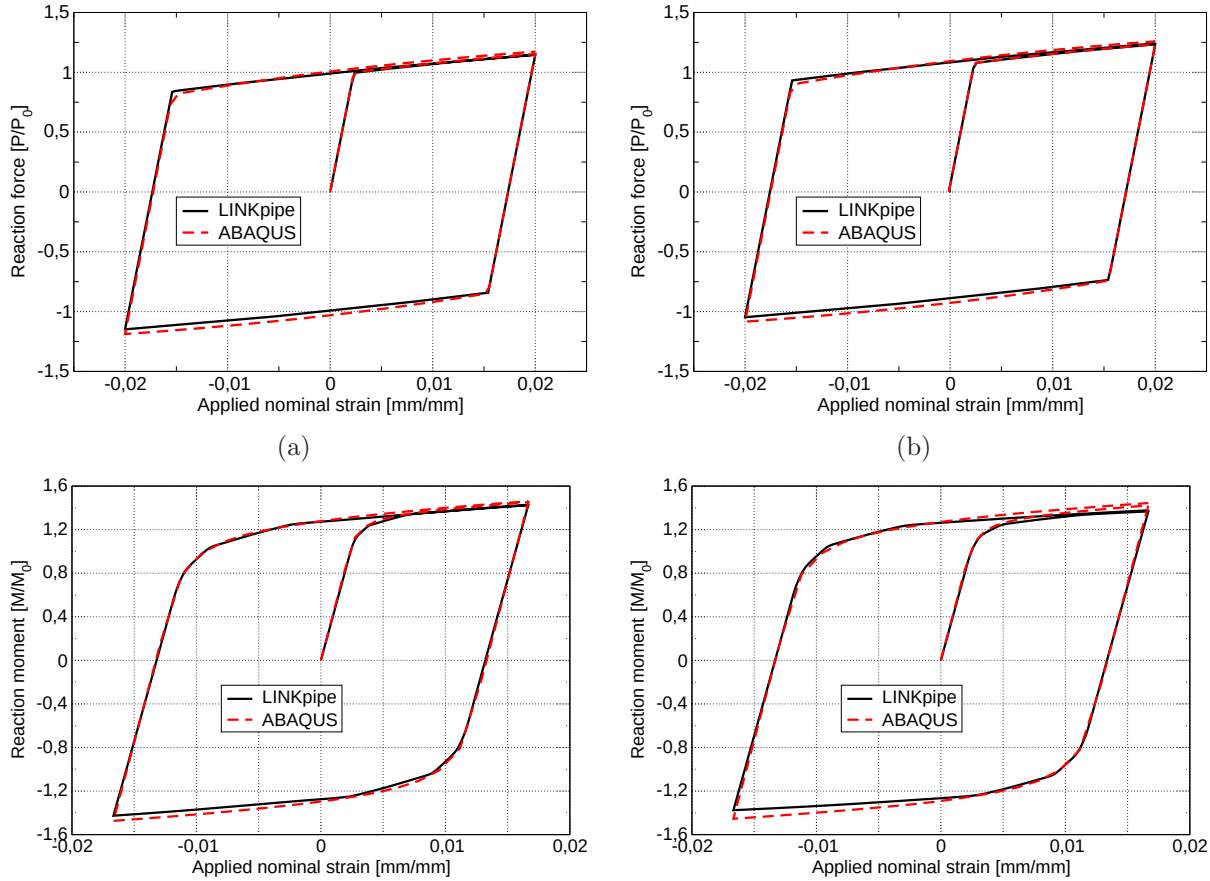

Figure 15: Comparisons of pipe segments between ABAQUS and LINK$_{pipe}$. (a) and (b) tension without and with internal pressure and (c) and (d) bending without and with internal pressure

In Fig. 15b an internal pressure of $10MPa$ is applied prior to the axial deformation. It is seen that the internal pressure induces a hoop stress in the pipe, thus to get the same level of deformation as for the case without internal pressure a higher axial reaction force is needed. Also here the difference in the global response between the numerical models is marginal.

Fig. 15c shows the global response from bending analyses without internal pressure for LINK$_{pipe}$ and 3D analyses. A rotation at the ends of the pipe segment is applied for both models to simulate a pure bending situation. The applied rotation is ± 0.1 radians which gives a nominal tensile strain at the outer pipe wall level of about $\pm 1.7\%$. As for the tensile cases, a marginal deviation between the models is also observed here. Fig. 15d shows the same result for a pipe subjected to an internal pressure prior to the global bending moment. The effect of the

internal pressure is marginal at this strain level. For higher strain levels, the internal pressure will prevent the pipe from local buckling as demonstrated by several authors, e.g. Østby et al. [22] and Berg et al. [2].

Fig. 16 contains only analyses from LINK$_{pipe}$ where the history effect is demonstrated. It is seen that the history effects are handled correctly for these variations of strain range in the cycles. Fig. 16a shows applied nominal strain versus tensile force for a pipe subjected to tensile deformation. In Fig. 16b a pipe is subjected to a pure bending situation.

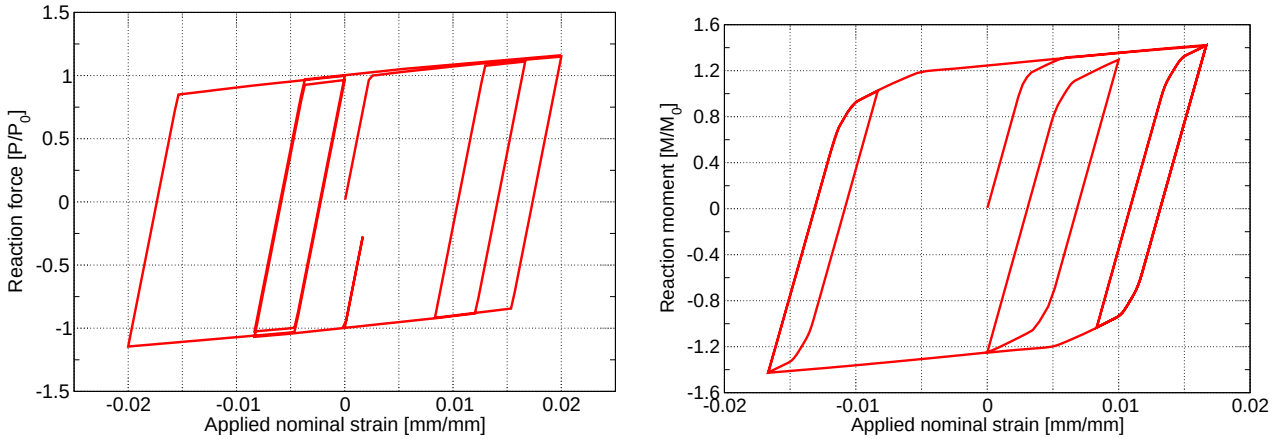

(a) (b)

Figure 16: History effects for a uniform pipe subjected to pure (a) tensile force and (b) bending moment

4.2 Pipe models with surface flaw

Pipe models with a surface flaw subjected to tensile loading are studied here to investigate the local behaviour of crack closure. The total crack length is 10% of the circumference. Two crack depth to thickness ratios are studied; 0.2 and 0.3. Note that only tension followed by compressive loading has been carried out. This is done in order to see the crack closure on the local behaviour. Full load cycles with a surface cracked pipe are explored in the comparisons with the large scale experiment at the end of this paper.

Fig. 17a and c show the applied elongation versus global reaction force for the pipes subjected to pure tensile loading. Results from the different crack geometries obtained from LINK$_{pipe}$ are displayed along with the corresponding 3D analyses. It is seen from the results that the global forces computed in LINK$_{pipe}$ corresponds very well with those from the 3D analyses. The effect of the crack depth on the global response from LINK$_{pipe}$ as shown in Fig. 17c is minimal. This corresponds with results from the literature, e.g. Jayadevan et al. [11].

The local response of the tensile models are shown in Fig. 17b and d. The crack face separation is plotted as a function of the applied nominal strain. Crack face separation is here defined as the opening distance for the penalty spring shown in Fig. 8a. For the first tensile load cycle (starting in origin), the response from LINK$_{pipe}$ follows the 3D analyses with reasonable agreement.

For the compressive load step, the results from the LINK$_{pipe}$ analyses follows the 3D analyses fairly well. The trends are captured although the crack faces come into full contact at slightly different global deformation levels. This can be due to the fact that the crack faces in the 3D analyses can change shape during the load cycle, whereas the crack face shape in the LINK$_{pipe}$ analyses does not change, i.e. shape change is not incorporated in the line-spring formulation. The chosen contact formulation seems to work well. When the crack faces come into contact, the crack face separation saturates when the applied global deformation increases.

The effect of the crack depth to thickness ratio on the crack face separation for pipe subjected to pure tensile loading is seen in Fig. 17f. It is seen that the crack face separation increases with increasing relative crack depth. Increasing relative crack depth gives raise to increasing crack faces, hence the crack face separation increases.

Fig. 18 shows the comparison between LINK$_{pipe}$ and 3D analyses for surface cracked pipes subjected to a global bending moment. Also here the total crack length is 10% of the circumference and the crack depth to thickness ratios are 0.2 and 0.3 respectively. It is seen that the global response corresponds very well for all crack depths. Fig. 18e shows the effect of crack depth on the global response. It is also here observed a marginal difference in the reaction bending moment which corresponds to results in the literature, e.g. Østby et al. [22].

The local behaviour of the crack face separation for the pipes subjected to pure bending is displayed in Fig. 18b and d. It is seen that the separation correspondence is most accurate for the crack depth to thickness ratio of 0.2 (Fig. 18b). The crack seems to open (first half of load cycle) with reasonable accuracy, but when the loads are reversed, a significant deviation between LINK$_{pipe}$ and the 3D model is seen.

Fig. 18f shows the effect of relative crack depth on crack face separation. As also observed for the tensile cases, the crack face separation increases with increasing crack depth for the same deformation level.

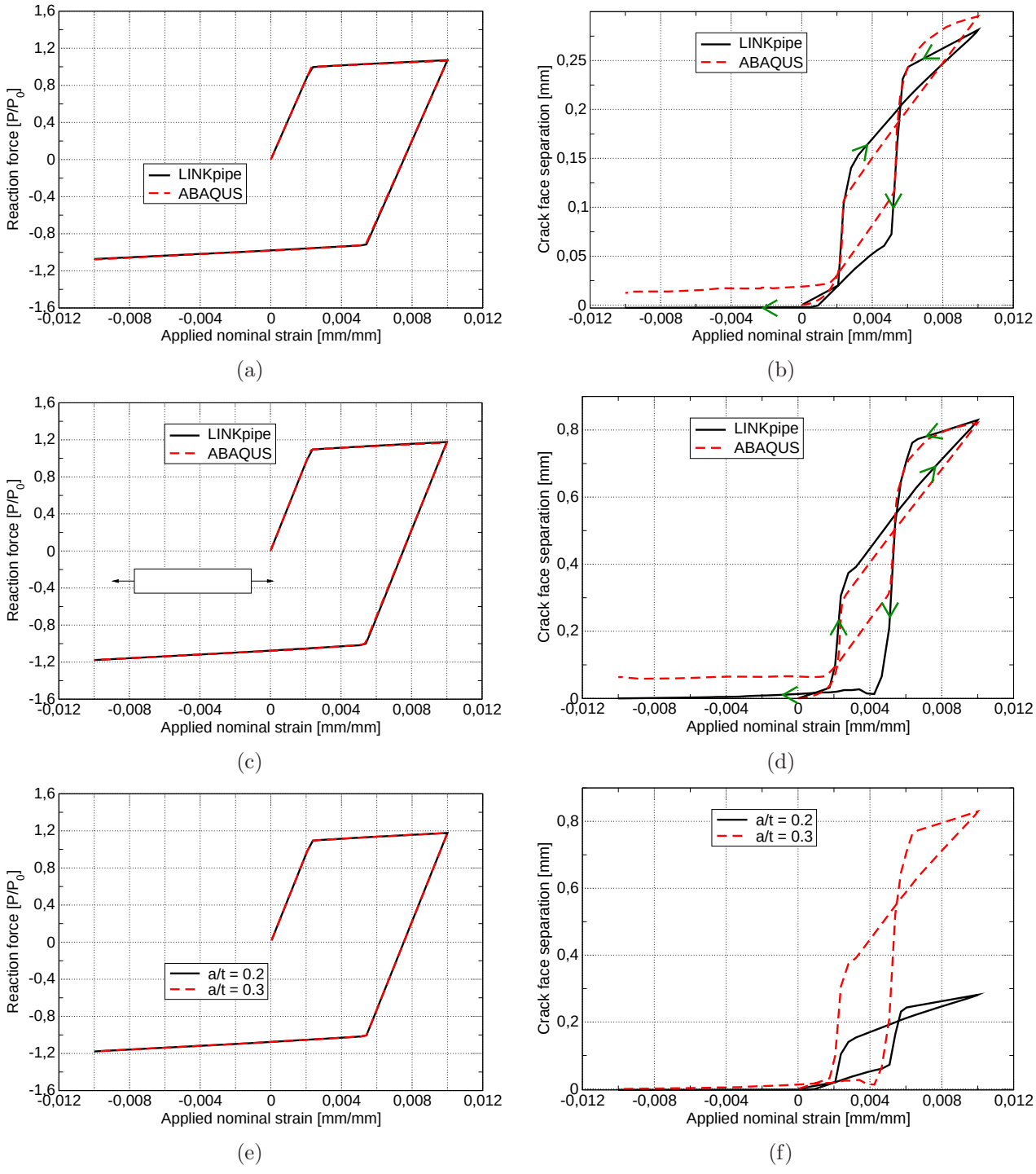

Figure 17: The variations of global axial force versus applied displacement (elongation) and crack face separation for a surface cracked pipe subjected to pure tensile loading, (a) global load for a/t=0.2 and (b) crack face separation for the same pipe. (c) global load for a/t=0.3 and (d) crack face separation for the same pipe. (e) shows the effect of crack depth on the global load and (f) shows the effect of the crack depth on the crack face separation for the LINK_{pipe} analyses

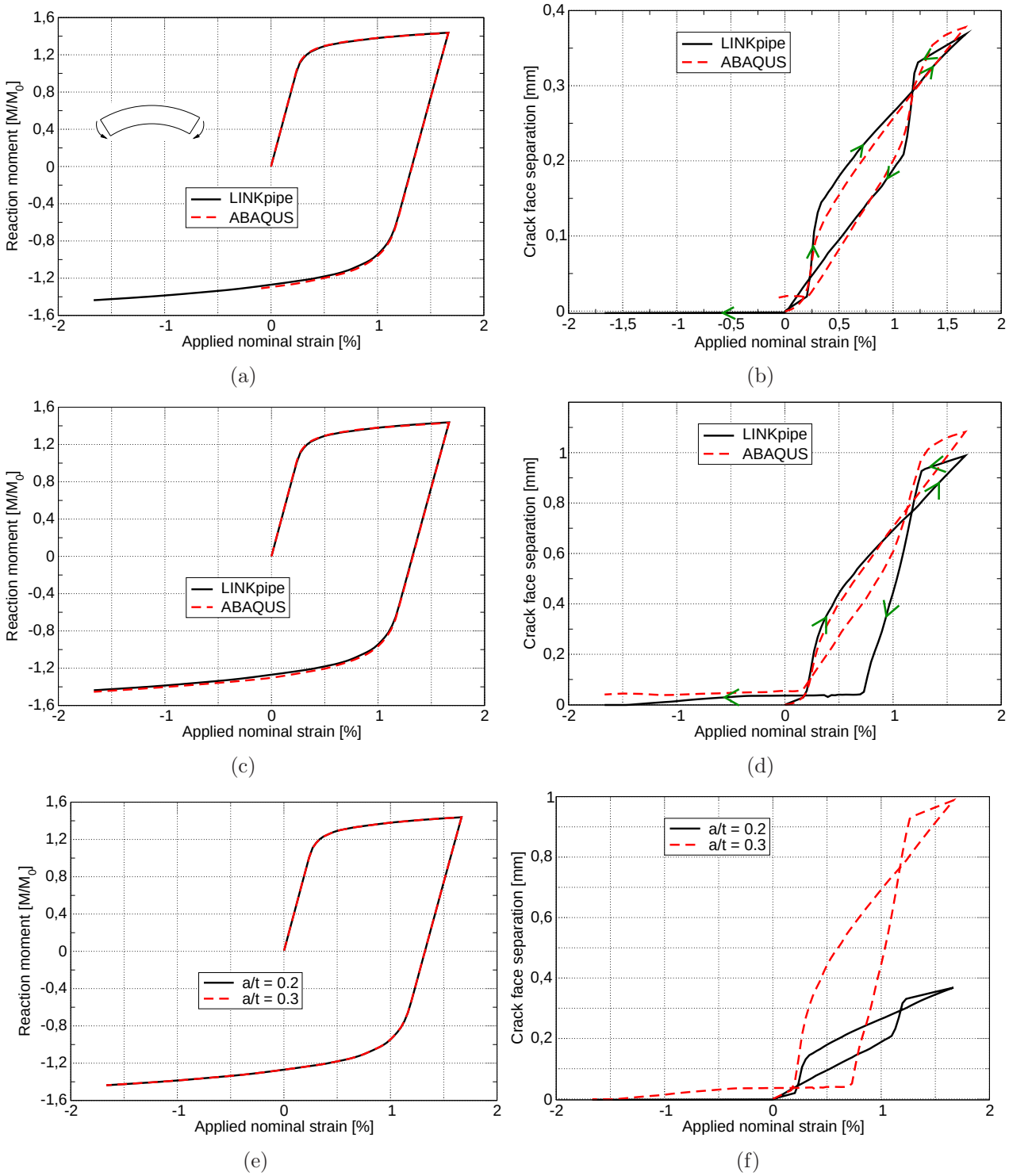

Figure 18: The variations of global moment versus applied rotation and crack face separation for a surface cracked pipe subjected to pure bending, (a) global load for a/t=0.2 and (b) crack face separation for the same pipe. (c) global load for a/t=0.3 and (d) crack face separation for the same pipe. (e) shows the effect of crack depth on the global load and (f) shows the effect of the crack depth on the crack face separation for the LINK$_{pipe}$ analyses

4.3 Cyclic loading of a surface cracked pipe

Large scale experiments of a surface cracked pipe subjected to cyclic loading was carried out by Nyhus et al. [20]. The pipe was subjected to a cyclic bending loading with a maximum nominal strain level of 2% and a negative nominal strain level of 0.57%.

The original experiment was done with a four point bending configuration of the pipe giving a constant curvature and strain level at the middle part of the pipe. The numerical analysis is carried out applying a bending moment giving the same nominal strain level. A reeling cycle for the experiment is displayed in Fig. 19. The initial crack depth (a) and crack length ($2c$) before cycling are $4.0mm$ and $60mm$ respectively.

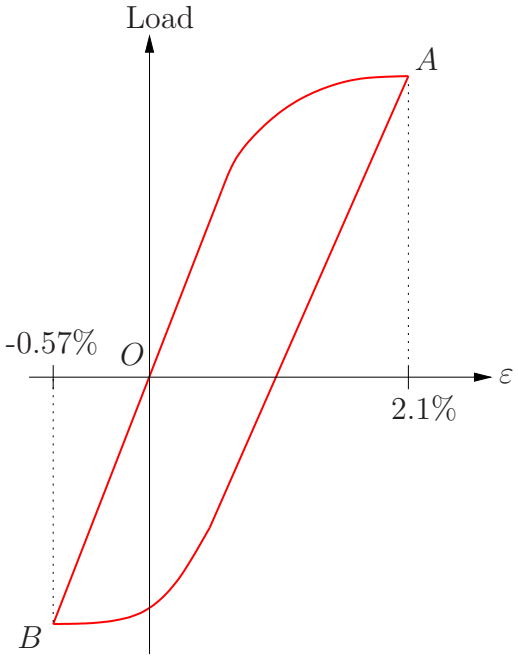

Figure 19: Reeling cycle starting with tension (OA), followed by a compressive loading (AB) before the applied forces are released and the elastic springback gives a straight pipe (BO)

The material's stress-strain curve and the crack growth resistance curve used in the comparison in Fig. 21 are shown in Figs. 11 and 12.

In Fig. 20 the generalised internal forces in an integration point in a line-spring element is displayed for the loading history in the comparison with the large scale experiment. It is seen how the stress resultant path rotates and shrinks after each reversal, indicating an increasing crack depth which gives a less steep slope on the curve. The hysteresis also contracts after each reversal indicating a contraction in the yield surface as described in Fig. 3.

The choice of using the monotonic crack growth resistance curve as base for determining the crack growth even for cyclic loading is because of the large cyclic plastic strains and very few cycles before failure. The crack growth mechanism in each load cycle from the experiment also reveals significant ductile tearing in each load cycle.

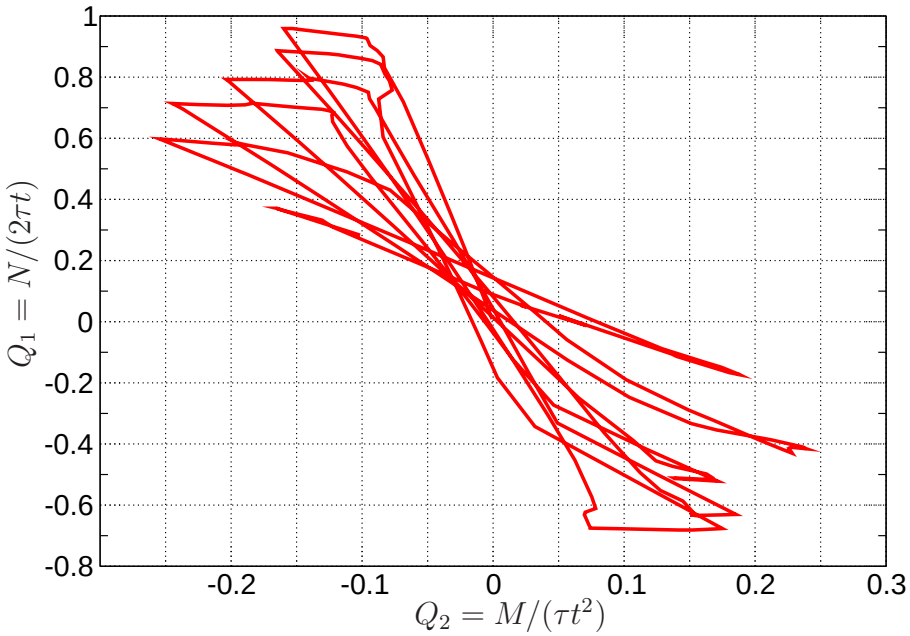

Figure 20: Normalised generalised forces in a line-spring element subjected to cyclic loading

The comparison of the accumulated crack growth at the deepest point versus number of load cycles is shown in Fig. 21. It is seen that the numerical analysis is conservative compared to the experimental measurement of accumulated crack growth. It must be remarked that the tearing curve presented by Nyhus et al. [20] (Fig. 22) is a linear relation between crack growth and CTOD. For a construction steel like the one used in this comparison, a significant amount of blunting is generally observed prior to the onset of ductile tearing. The numerical analysis assumes all crack extension to be tearing when the crack growth resistance curve starts in origin. The first reeling cycle appeared not to have any ductile tearing, thus blunting and resharpening of the crack occurred. The tearing was first observed in the second reeling cycle. The crack growth resistance curve used is taken from multiple SENT specimens loaded to different levels of crack growth. Østby et al. [21] demonstrated the effect of measurement techniques on the crack growth resistance curve. It was seen that the crack growth resistance curve measured on multiple SENT-specimens was generally more conservative than the one measured directly on the pipe using silicone replicas. Also the region where crack tip blunting is controlling was more clearly seen on the curves. The crack growth resistance curve reported by Nyhus et al. [20] does not have a distinct blunting region. Due to the lack of a blunting region on the crack growth resistance curve, the experimental data are shifted upwards corresponding to the blunting displacement prior to ductile tearing ($\approx 0.43mm$).

With this in mind it can be argued that the crack growth resistance curve used in the present comparison is conservative and a crack growth resistance curve measured on the actual pipe geometry accounting for crack tip blunting would be more accurate. A brief parametric study of the effect of having a higher crack growth resistance curve is now presented. Two approaches are studied. The first approach changes the slope of the crack growth resistance curve assuming the constraint level of the actual pipe is lower than the constraint level of the multiple SENT-specimens used to form the crack growth resistance curve. The second approach uses a non

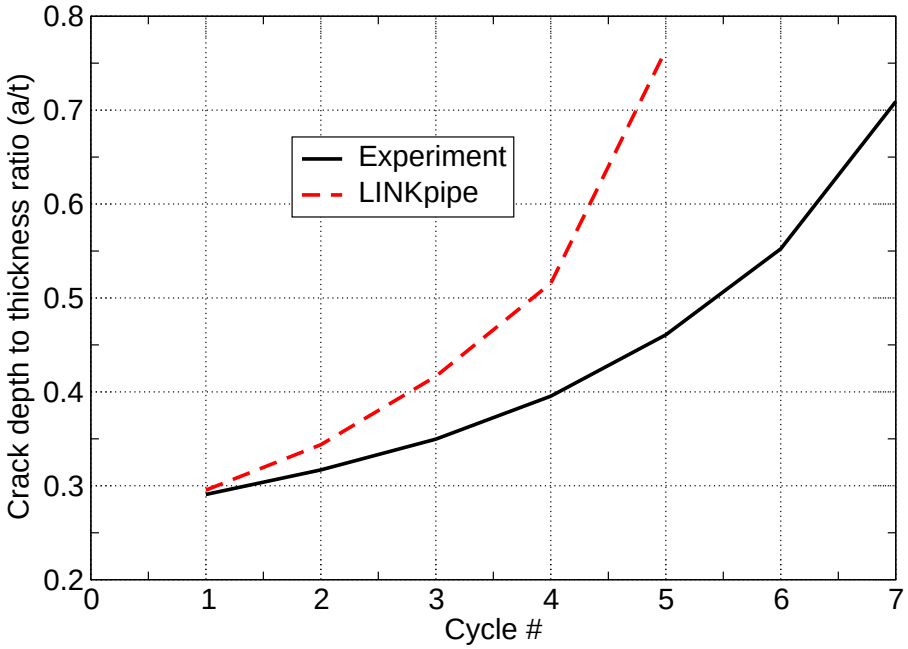

Figure 21: Comparison between large scale experiment and LINK$_{pipe}$ for a surface cracked pipe subjected to pure bending loading

linear crack growth resistance curve where the initial part of the curve where crack tip blunting is governing the behaviour is steeper than the region where tearing is controlling.

In Fig. 22, the effect of altering the slope on the crack growth resistance curve for the same pipe geometry and loading conditions as used in Fig. 21. An increasing slope increases the tearing resistance. The upper dashed curve (red) is the curve from Fig. 21.

Generally the monotonic crack growth resistance curve has a distinct blunting region which is seen as an initial steep curve where the slope is gradually reduced when tearing occurs. These curves can in many cases be approximated as a non linear function on the form $\delta = C_1(\Delta a)^{C_2}$ where C_1 and C_2 are two fitting constants. The current implementation assumes that the curve follows such a relation. Fig. 23 shows some analyses carried out using crack growth resistance curve on this form. Here the experimental data are not shifted since the chosen crack growth resistance curve has a distinct blunting region present. The parameter C_1 is kept constant to 2.3 and the exponent, C_2 varies from 0.6 to 0.8. The curve with an exponent of 0.7 gives almost a perfect match to the experimental curve.

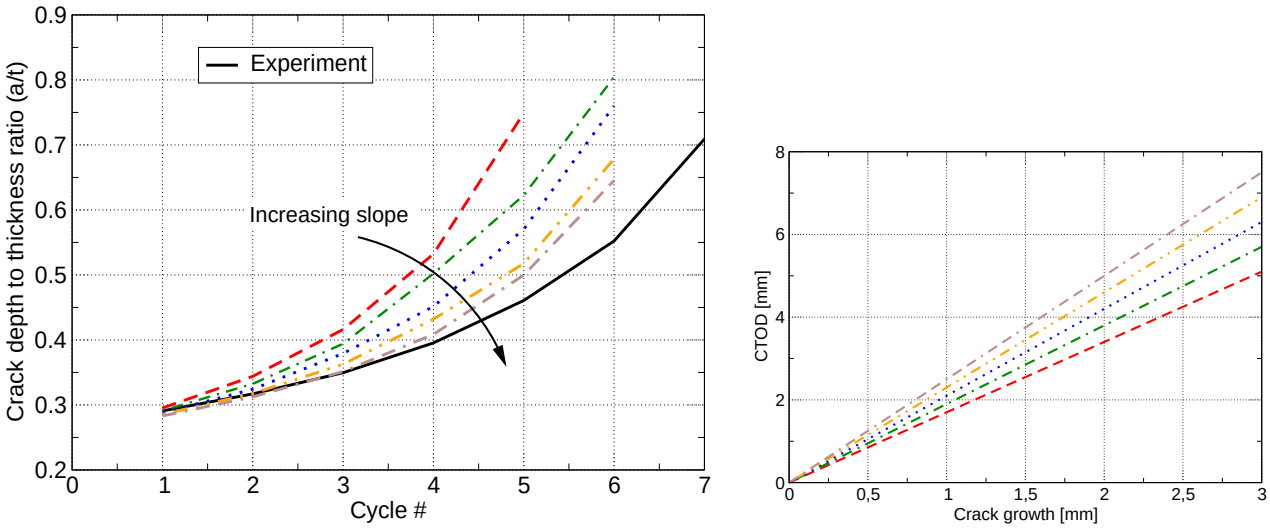

(a) (b)

Figure 22: (a) effect of changing the slope of a linear crack growth resistance curve on the cyclic crack growth behaviour and (b) collection of the linear crack growth resistance curves on the form $\delta = C_1(\Delta a)^{1.0}$ where $C_1 \in \{1.7, 1.9, 2.1, 2.3, 2.5\}$

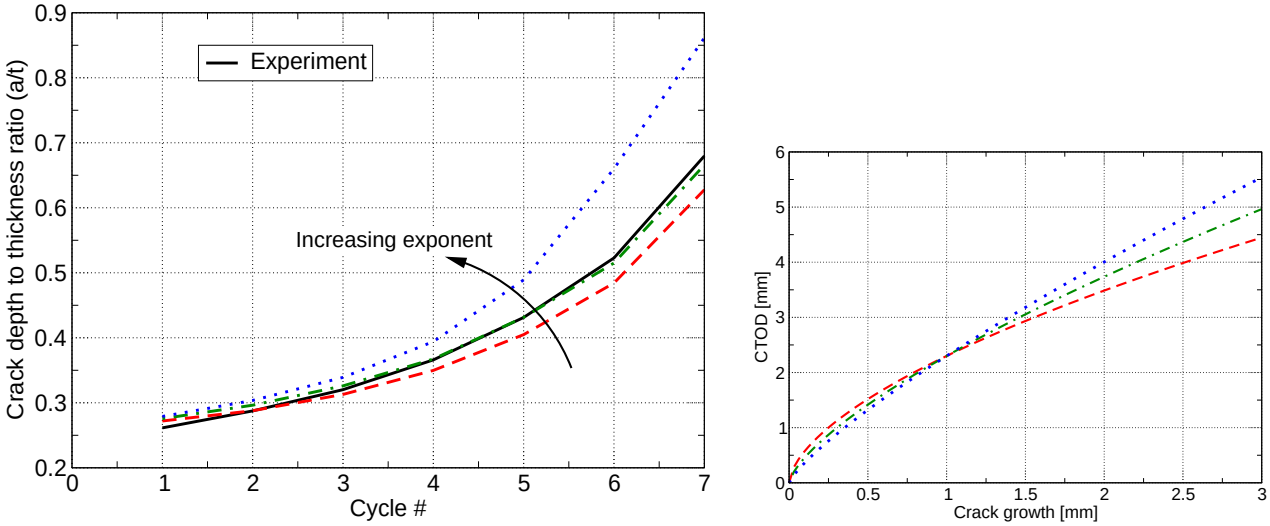

(a) (b)

Figure 23: (a) effect of having a distinct blunting region on the crack growth resistance curve on the cyclic crack growth behaviour and (b) a collection of the crack growth resistance curves on the form $\delta = 2.3(\Delta a)^{C_2}$ where $C_2 \in \{0.6, 0.7, 0.8\}$

5 Conclusions

In this study numerical models from LINK$_{pipe}$ are compared with corresponding 3D-models from ABAQUS. Pipe models subjected to cyclic loading are investigated. The different load cases have been tension, bending and internal pressure.

A proposed simple contact formulation for the line-spring element based on penalty springs is also presented. The contact between the crack faces seems to be captured well. When the crack faces come into contact, further compression of the line-spring element does not occur.

The Ziegler kinematic hardening rule is a linear kinematic hardening rule. In the current implementation in the ANDES thin shell finite element, the Ziegler rule is applied on a piecewise linear stress-strain behaviour with promising results. An approximation to the Masing's rule is also implemented to ensure a correct behaviour for reversed loading. The results from the pipe analyses using this hardening model show good correspondence with the 3D analyses for both tension, bending and with/without internal pressure.

A proposed kinematic hardening model for the line-spring element is presented herein. The yield surface for the line-spring element consists of tabulated points for different crack depth to thickness ratios where the points are connected by line segments. The crack growth follows the crack growth resistance curve and the yield surface contracts when the crack depth to thickness ratio increases.

Comparison between LINK$_{pipe}$ and large scale experiments of a pipe subjected to a cyclic global bending loading and ductile crack growth is also carried out. It shows that the present methodology can catch the tendencies despite a deviation in the comparison. The monotonic crack growth resistance curve used as input for the ductile tearing in this comparison has some implications due to its form. A parametric study of a tearing curve on the more general form with a distinct blunting region is carried out.

References

[1] ABAQUS. *Theory Manual, version 6.7-1.* Dassault Systèmes, Providence, RI, 2007.

[2] E. Berg, E. Østby, C. Thaulow, and B. Skallerud. Ultimate fracture capacity of pressurised pipes with defects - Comparisons of large scale testing and numerical simulations. *Engineering Fracture Mechanics*, 75:2352–2366, 2008.

[3] E. Berg, B. Skallerud, and C. Thaulow. Two-parameter fracture mechanics and circumferential crack growth in surface cracked pipelines using line-spring elements. *Engineering Fracture Mechanics*, 75:17–30, 2008.

[4] E. Berg, B. Skallerud, C. Thaulow, and K. Holthe. Using constraint correction to ductile crack growth in surface cracked shell-structures. *In proceedings: MekIT'05 Computational Mechanics, Trondheim, Norway. ISBN: 82-519-2052-3.*, pages 75–85, 2005.

[5] M. Á. Caminero and F. J. Montáns. An enhanced algorithm for nested surfaces plasticity using the implicit Mróz translation rule. *Computers and Structures*, 84:1684–1695, 2006.

[6] M. A. Crisfield. *Non-linear finite element analysis of solids and structures: Advanced topics*, volume 2. John Wiley & Sons Ltd., 1997. ISBN: 0-471-95649-X.

[7] Y. F. Dafalias and E. P. Popov. Cyclic loading for materials with a vanishing elastic region. *Nuclear Engineering and Design*, 41:293–302, 1977.

[8] N. E. Dowling. *Mechanical behavior of materials, engineering methods for deformation, fracture and fatigue.* Prentice Hall, second edition edition, 1999. ISBN: 0-13-905720-X.

[9] N. E. Dowling and J. A. Begley. Fatigue Crack Growth During Gross Plasticity and the J-Integral. In *Proceedings of the Eighth National Symposium on Fracture Mechanics*, volume STP 590, pages 82–103. ASTM, 1974.

[10] C. A. Felippa and C. Militello. Membrane triangles with corner drilling freedoms: II. The ANDES element. *Finite Elements in Analysis and Design*, 12:189–201, 1992.

[11] K. R. Jayadevan, E. Østby, and C. Thaulow. Fracture response of pipelines subjected to large plastic deformation under tension. *International Journal of Pressure Vessel and Piping*, 81:771–783, 2004.

[12] A. R. Khoei and N. Jamali. On the implementation of a multi-surface kinematic hardening plasticity and its applications. *International Journal of Plasticity*, 21:1741–1770, 2005.

[13] R. D. Krieg. A practical Two-Surface Plasticity Theory. *Journal of Applied Mechanics*, 42:641–646, 1975.

[14] H. Lee and D. M. Parks. Fully plastic analyses of plane strain single-edge-cracked specimens subjected to combined tension and bending. *International Journal of Fracture*, 63:329–349, 1993.

[15] H. Lee and D. M. Parks. Enhanced elastic-plastic line-spring finite element. *International Journal of Solids and Structures*, 32(16):2393–2418, 1995.

[16] J. Lemaitre and J.-L. Chaboche. *Mechanics of solid materials*. Cambridge University Press, 1990. ISBN: 0-521-32853-5.

[17] G. Masing. Eigenspannungen und Verfestigung beim Messing. *In proceedings: The 2nd International Congress for Applied Mechanics, Zürich, Switzerland*, pages 332–335, 1926.

[18] H. H. Michels. Abscissas and Weight Coefficients for Lobatto Quadrature. *Mathematics of Computation*, 17(83):237–244, 1963.

[19] Z. Mróz. On the description of anisotropic workhardening. *Journal of the Mechanics and Physics of Solids*, 15:163–175, 1967.

[20] B. Nyhus, M.P. Loria, and O.L. Ørjasæter. SENT specimens an alternative to SENB specimens for fracture mechanics testing of pipelines. *Proceedings of OMAE2003, 22nd International Conference of Offshore Mechanics and arctic engineering, Cancun, Mexico*, 2003.

[21] E. Østby, M. Hauge, E. Levold, A. Sandvik, B. Nyhus, and C. Thaulow. Strain capacity of SENT specimens – Influence of weld metal mismatch and ductile tearing resistance. *In proceedings: ISOPE2007, The 18th International Offshore and Polar Engineering Conference*, 2008.

[22] E. Østby, K. R. Jayadevan, and C. Thaulow. Fracture response of pipelines subject to large plastic deformation under bending. *International Journal of Pressure Vessels and Piping*, 82:201–215, 2005.

[23] G. M. Owolabi and M. N. K. Singh. Extension of a multi-surface plasticity model to two-phase materials. *International Journal of Solids and Structures*, 44:1086–1098, 2007.

[24] W. Prager. A new method of analyzing stresses and strains in work-hardening plastic solids. *Journal of Applied Mechanics*, 23:493–496, 1956.

[25] J.R. Rice and N. Levy. The part-through surface crack in an elastic plate. *Journal of Applied Mechanics*, 39:185–194, 1972.

[26] J.C. Simo and T.J.R. Hughes. *Computational Inelasticity*. Springer-Verlag, New York, Inc., 2000. ISBN: 0-387-97520-9.

[27] B. Skallerud. Constitutive modelling of cyclic plasticity and some implications for the computation of biaxial low cycle fatigue damage. *Engineering Fracture Mechanics*, 41(5):753–769, 1992.

[28] B. Skallerud and B. Haugen. Collapse of thin shell structures - stress resultant plasticity modelling within a co-rotated ANDES finite element formulation. *International Journal for Numerical Methods in Engineering*, 46:1961–1986, 1999.

[29] B. Skallerud, K. Holthe, and B. Haugen. Thin shell and surface crack finite elements for simulation of combined failure modes. *Computer Methods in Applied Mechanics and Engineering*, 194(21-24):2619–2640, 2005.

[30] B. Skallerud and Z. L. Zhang. A 3D numerical study of ductile tearing and fatigue crack growth under nominal cyclic plasticity. *International Journal of Solids and Structures*, 34(24):3141–3161, 1997.

[31] B. Skallerud and Z. L. Zhang. On numerical analysis of damage evolution in cyclic elastic-plastic crack growth problems. *Fatigue and Fracture of Engineering Materials and Structures*, 23:81–86, 2000.

[32] N. T. Tseng and G. C. Lee. Simple plasticity model of two-surface type. *Journal of Engineering Materials*, 109:795–810, 1983.

[33] D. M. Parks and C. S. White. Elastic-plastic line-spring finite elements for surface-cracked plates and shells. *Journal of Pressure Vessel Technology*, 104:287–292, 1982.

[34] H. Ziegler. A modification of Prager's hardening rule. *Quarterly of Applied Mechanics*, 17:55–65, 1959.

DEPARTMENT OF STRUCTURAL ENGINEERING
NORWEGIAN UNIVERSITY OF SCIENCE AND TECHNOLOGY

N 7491 TRONDHEIM, NORWAY
Telephone: +47 73 59 47 00 Telefax: +47 73 59 47 01

"Reliability Analysis of Structural Systems using Nonlinear Finite Element Methods",
C. A. Holm, 1990:23, ISBN 82-7119-178-0.

"Uniform Stratified Flow Interaction with a Submerged Horizontal Cylinder",
Ø. Arntsen, 1990:32, ISBN 82-7119-188-8.

"Large Displacement Analysis of Flexible and Rigid Systems Considering Displacement–Dependent Loads and Nonlinear Constraints",
K. M. Mathisen, 1990:33, ISBN 82-7119-189-6.

"Solid Mechanics and Material Models including Large Deformations",
E. Levold, 1990:56, ISBN 82-7119-214-0, ISSN 0802-3271.

"Inelastic Deformation Capacity of Flexurally-Loaded Aluminium Alloy Structures",
T. Welo, 1990:62, ISBN 82-7119-220-5, ISSN 0802-3271.

"Visualization of Results from Mechanical Engineering Analysis",
K. Aamnes, 1990:63, ISBN 82-7119-221-3, ISSN 0802-3271.

"Object-Oriented Product Modeling for Structural Design",
S. I. Dale, 1991:6, ISBN 82-7119-258-2, ISSN 0802-3271.

"Parallel Techniques for Solving Finite Element Problems on Transputer Networks",
T. H. Hansen, 1991:19, ISBN 82-7119-273-6, ISSN 0802-3271.

"Statistical Description and Estimation of Ocean Drift Ice Environments",
R. Korsnes, 1991:24, ISBN 82-7119-278-7, ISSN 0802-3271.

"Properties of concrete related to fatigue damage: with emphasis on high strength concret",
G. Petkovic, 1991:35, ISBN 82-7119-290-6, ISSN 0802-3271.

"Turbidity Current Modelling",
B. Brørs, 1991:38, ISBN 82-7119-293-0, ISSN 0802-3271.

"Zero-Slump Concrete: Rheology, Degree of Compaction and Strength. Effects of Fillers as Part Cement-Replacement",
C. Sørensen, 1992:8, ISBN 82-7119-357-0, ISSN 0802-3271.

"Nonlinear Analysis of Reinforced Concrete Structures Exposed to Transient Loading",
K. V. Høiseth, 1992:15, ISBN 82-7119-364-3, ISSN 0802-3271.

"Finite Element Formulations and Solution Algorithms for Buckling and Collapse Analysis of Thin Shells",
R. O. Bjærum, 1992:30, ISBN 82-7119-380-5, ISSN 0802-3271.

"Response Statistics of Nonlinear Dynamic Systems",
J. M. Johnsen, 1992:42, ISBN 82-7119-393-7, ISSN 0802-3271.

"Digital Models in Engineering. A Study on why and how engineers build and operate digital models for decisison support",
J. Høyte, 1992:75, ISBN 82-7119-429-1, ISSN 0802-3271.

"Sparse Solution of Finite Element Equations",
A. C. Damhaug, 1992:76, ISBN 82-7119-430-5, ISSN 0802-3271.

"Some Aspects of Floating Ice Related to Sea Surface Operations in the Barents Sea",
S. Løset, 1992:95, ISBN 82-7119-452-6, ISSN 0802-3271.

"Modelling of Cyclic Plasticity with Application to Steel and Aluminium Structures",
O. S. Hopperstad, 1993:7, ISBN 82-7119-461-5, ISSN 0802-3271.

"The Free Formulation: Linear Theory and Extensions with Applications to Tetrahedral Elements with Rotational Freedoms",
G. Skeie, 1993:17, ISBN 82-7119-472-0, ISSN 0802-3271.

"Høyfast betongs motstand mot piggdekkslitasje. Analyse av resultater fra prøving i Veisliter'n",
T. Tveter, 1993:62, ISBN 82-7119-522-0, ISSN 0802-3271.

"A Nonlinear Finite Element Based on Free Formulation Theory for Analysis of Sandwich Structures",
O. Aamlid, 1993:72, ISBN 82-7119-534-4, ISSN 0802-3271.

"The Effect of Curing Temperature and Silica Fume on Chloride Migration and Pore Structure of High Strength Concrete",
C. J. Hauck, 1993:90, ISBN 82-7119-553-0, ISSN 0802-3271.

"Failure of Concrete under Compressive Strain Gradients",
G. Markeset, 1993:110, ISBN 82-7119-575-1, ISSN 0802-3271.

"An experimental study of internal tidal amphidromes in Vestfjorden",
J. H. Nilsen, 1994:39, ISBN 82-7119-640-5, ISSN 0802-3271.

"Structural analysis of oil wells with emphasis on conductor design",
H. Larsen, 1994:46, ISBN 82-7119-648-0, ISSN 0802-3271.

"Adaptive methods for non-linear finite element analysis of shell structures",
K. M. Okstad, 1994:66, ISBN 82-7119-670-7, ISSN 0802-3271.

"On constitutive modelling in nonlinear analysis of concrete structures",
O. Fyrileiv, 1994:115, ISBN 82-7119-725-8, ISSN 0802-3271.

"Fluctuating wind load and response of a line-like engineering structure with emphasis on motion-induced wind forces",
J. Bogunovic Jakobsen, 1995:62, ISBN 82-7119-809-2, ISSN 0802-3271.

"An experimental study of beam-columns subjected to combined torsion, bending and axial actions",
A. Aalberg, 1995:66, ISBN 82-7119-813-0, ISSN 0802-3271.

"Scaling and cracking in unsealed freeze/thaw testing of Portland cement and silica fume concretes",
S. Jacobsen, 1995:101, ISBN 82-7119-851-3, ISSN 0802-3271.

"Damping of water waves by submerged vegetation. A case study of laminaria hyperborea",
A. M. Dubi, 1995:108, ISBN 82-7119-859-9, ISSN 0802-3271.

"The dynamics of a slope current in the Barents Sea",
Sheng Li, 1995:109, ISBN 82-7119-860-2, ISSN 0802-3271.

"Modellering av delmaterialenes betydning for betongens konsistens",
Ernst Mørtsell, 1996:12, ISBN 82-7119-894-7, ISSN 0802-3271.

"Bending of thin-walled aluminium extrusions",
Birgit Søvik Opheim, 1996:60, ISBN 82-7119-947-1, ISSN 0802-3271.

"Material modelling of aluminium for crashworthiness analysis",
Torodd Berstad, 1996:89, ISBN 82-7119-980-3, ISSN 0802-3271.

"Estimation of structural parameters from response measurements on submerged floating tunnels",
Rolf Magne Larssen, 1996:119, ISBN 82-471-0014-2, ISSN 0802-3271.

"Numerical modelling of plain and reinforced concrete by damage mechanics",
Mario A. Polanco-Loria, 1997:20, ISBN 82-471-0049-5, ISSN 0802-3271.

"Nonlinear random vibrations - numerical analysis by path integration methods",
Vibeke Moe, 1997:26, ISBN 82-471-0056-8, ISSN 0802-3271.

"Numerical prediction of vortex-induced vibration by the finite element method",
Joar Martin Dalheim, 1997:63, ISBN 82-471-0096-7, ISSN 0802-3271.

"Time domain calculations of buffeting response for wind sensitive structures",
Ketil Aas-Jakobsen, 1997:148, ISBN 82-471-0189-0, ISSN 0802-3271.

"A numerical study of flow about fixed and flexibly mounted circular cylinders",
Trond Stokka Meling, 1998:48, ISBN 82-471-0244-7, ISSN 0802-3271.

"Estimation of chloride penetration into concrete bridges in coastal areas",
Per Egil Steen, 1998:89, ISBN 82-471-0290-0, ISSN 0802-3271.

"Stress-resultant material models for reinforced concrete plates and shells",
Jan Arve Øverli, 1998:95, ISBN 82-471-0297-8, ISSN 0802-3271.

"Chloride binding in concrete. Effect of surrounding environment and concrete composition",
Claus Kenneth Larsen, 1998:101, ISBN 82-471-0337-0, ISSN 0802-3271.

"Rotational capacity of aluminium alloy beams",
Lars A. Moen, 1999:1, ISBN 82-471-0365-6, ISSN 0802-3271.

"Stretch Bending of Aluminium Extrusions",
Arild H. Clausen, 1999:29, ISBN 82-471-0396-6, ISSN 0802-3271.

"Aluminium and Steel Beams under Concentrated Loading",
Tore Tryland, 1999:30, ISBN 82-471-0397-4, ISSN 0802-3271.

"Engineering Models of Elastoplasticity and Fracture for Aluminium Alloys",
Odd-Geir Lademo, 1999:39, ISBN 82-471-0406-7, ISSN 0802-3271.

"Kapasitet og duktilitet av dybelforbindelser i trekonstruksjoner",
Jan Siem, 1999:46, ISBN 82-471-0414-8, ISSN 0802-3271.

"Etablering av distribuert ingeniørarbeid; Teknologiske og organisatoriske erfaringer fra en norsk ingeniørbedrift",
Lars Line, 1999:52, ISBN 82-471-0420-2, ISSN 0802-3271.

"Estimation of Earthquake-Induced Response",
Símon Ólafsson, 1999:73, ISBN 82-471-0443-1, ISSN 0802-3271.

"Coastal Concrete Bridges: Moisture State, Chloride Permeability and Aging Effects" Ragnhild Holen Relling, 1999:74, ISBN 82-471-0445-8, ISSN 0802-3271.

"Capacity Assessment of Titanium Pipes Subjected to Bending and External Pressure", Arve Bjørset, 1999:100, ISBN 82-471-0473-3, ISSN 0802-3271.

"Validation of Numerical Collapse Behaviour of Thin-Walled Corrugated Panels", Håvar Ilstad, 1999:101, ISBN 82-471-0474-1, ISSN 0802-3271.

"Strength and Ductility of Welded Structures in Aluminium Alloys", Miroslaw Matusiak, 1999:113, ISBN 82-471-0487-3, ISSN 0802-3271.

"Thermal Dilation and Autogenous Deformation as Driving Forces to Self-Induced Stresses in High Performance Concrete", Øyvind Bjøntegaard, 1999:121, ISBN 82-7984-002-8, ISSN 0802-3271.

"Some Aspects of Ski Base Sliding Friction and Ski Base Structure", Dag Anders Moldestad, 1999:137, ISBN 82-7984-019-2, ISSN 0802-3271.

"Electrode reactions and corrosion resistance for steel in mortar and concrete", Roy Antonsen, 2000:10, ISBN 82-7984-030-3, ISSN 0802-3271.

"Hydro-Physical Conditions in Kelp Forests and the Effect on Wave Damping and Dune Erosion. A case study on Laminaria Hyperborea", Stig Magnar Løvås, 2000:28, ISBN 82-7984-050-8, ISSN 0802-3271.

"Random Vibration and the Path Integral Method", Christian Skaug, 2000:39, ISBN 82-7984-061-3, ISSN 0802-3271.

"Buckling and geometrical nonlinear beam-type analyses of timber structures", Trond Even Eggen, 2000:56, ISBN 82-7984-081-8, ISSN 0802-3271.

"Structural Crashworthiness of Aluminium Foam-Based Components", Arve Grønsund Hanssen, 2000:76, ISBN 82-7984-102-4, ISSN 0809-103X.

"Measurements and simulations of the consolidation in first-year sea ice ridges, and some aspects of mechanical behaviour", Knut V. Høyland, 2000:94, ISBN 82-7984-121-0, ISSN 0809-103X.

"Kinematics in Regular and Irregular Waves based on a Lagrangian Formulation", Svein Helge Gjøsund, 2000-86, ISBN 82-7984-112-1, ISSN 0809-103X.

"Self-Induced Cracking Problems in Hardening Concrete Structures", Daniela Bosnjak, 2000-121, ISBN 82-7984-151-2, ISSN 0809-103X.

"Ballistic Penetration and Perforation of Steel Plates",

Tore Børvik, 2000:124, ISBN 82-7984-154-7, ISSN 0809-103X.

"Freeze-Thaw resistance of Concrete. Effect of: Curing Conditions, Moisture Exchange and Materials",
Terje Finnerup Rønning, 2001:14, ISBN 82-7984-165-2, ISSN 0809-103X

"Structural behaviour of post tensioned concrete structures. Flat slab. Slabs on ground",
Steinar Trygstad, 2001:52, ISBN 82-471-5314-9, ISSN 0809-103X.

"Slipforming of Vertical Concrete Structures. Friction between concrete and slipform panel",
Kjell Tore Fosså, 2001:61, ISBN 82-471-5325-4, ISSN 0809-103X.

"Some numerical methods for the simulation of laminar and turbulent incompressible flows",
Jens Holmen, 2002:6, ISBN 82-471-5396-3, ISSN 0809-103X.

"Improved Fatigue Performance of Threaded Drillstring Connections by Cold Rolling",
Steinar Kristoffersen, 2002:11, ISBN: 82-421-5402-1, ISSN 0809-103X.

"Deformations in Concrete Cantilever Bridges: Observations and Theoretical Modelling",
Peter F. Takâcs, 2002:23, ISBN 82-471-5415-3, ISSN 0809-103X.

"Stiffened aluminium plates subjected to impact loading",
Hilde Giæver Hildrum, 2002:69, ISBN 82-471-5467-6, ISSN 0809-103X.

"Full- and model scale study of wind effects on a medium-rise building in a built up area",
Jónas Thór Snæbjørnsson, 2002:95, ISBN82-471-5495-1, ISSN 0809-103X.

"Evaluation of Concepts for Loading of Hydrocarbons in Ice-infested water",
Arnor Jensen, 2002:114, ISBN 82-417-5506-0, ISSN 0809-103X.

"Numerical and Physical Modelling of Oil Spreading in Broken Ice",
Janne K. Økland Gjøsteen, 2002:130, ISBN 82-471-5523-0, ISSN 0809-103X.

"Diagnosis and protection of corroding steel in concrete",
Franz Pruckner, 20002:140, ISBN 82-471-5555-4, ISSN 0809-103X.

"Tensile and Compressive Creep of Young Concrete: Testing and Modelling",
Dawood Atrushi, 2003:17, ISBN 82-471-5565-6, ISSN 0809-103X.

"Rheology of Particle Suspensions. Fresh Concrete, Mortar and Cement Paste with Various Types of Lignosulfonates",
Jon Elvar Wallevik, 2003:18, ISBN 82-471-5566-4, ISSN 0809-103X.

"Oblique Loading of Aluminium Crash Components",
Aase Reyes, 2003:15, ISBN 82-471-5562-1, ISSN 0809-103X.

"Utilization of Ethiopian Natural Pozzolans",
Surafel Ketema Desta, 2003:26, ISSN 82-471-5574-5, ISSN:0809-103X.

"Behaviour and strength prediction of reinforced concrete structures with discontinuity regions",
Helge Brå, 2004:11, ISBN 82-471-6222-9, ISSN 1503-8181.

"High-strength steel plates subjected to projectile impact. An experimental and numerical study",
Sumita Dey, 2004:38, ISBN 82-471-6281-4 (electronic version), ISBN 82-471-6282-2 (printed version), ISSN 1503-8181.

"Alkali-reactive and inert fillers in concrete. Rheology of fresh mixtures and expansive reactions",
Bård M. Pedersen, 2004:92, ISBN 82-471-6401-9 (printed version), ISBN 82-471-6400-0 (electronic version), ISSN 1503-8181.

"On the Shear Capacity of Steel Girders with Large Web Openings",
Nils Christian Hagen, 2005:9 ISBN 82-471-6878-2 (printed version), ISBN 82-471-6877-4 (electronic version), ISSN 1503-8181.

"Behaviour of aluminium extrusions subjected to axial loading",
Østen Jensen, 2005:7, ISBN 82-471-6872-3 (electronic version) , ISBN 82-471-6873-1 (printed version), ISSN 1503-8181.

"Thermal Aspects of corrosion of Steel in Concrete",
Jan-Magnus Østvik, 2005:5, ISBN 82-471-6869-3 (printed version) ISBN 82-471-6868 (electronic version), ISSN 1503-8181.

"Mechanical and adaptive behaviour of bone in relation to hip replacement. A study of bone remodelling and bone grafting,"
Sébastien Muller, 2005:34, ISBN 82-471-6933-9 (printed version) (ISBN 82-471-6932-0 (electronic version), ISSN 1503-8181.

"Analysis of geometrical nonlinearities with applications to timber structures",
Lars Wollebæk, 2005:74, ISBN 82-471-7050-5 (printed version), ISBN 82-471-7019-1 (electronic version), ISSN 1503-8181.

"Pedestrian induced lateral vibrations of slender footbridges",
Anders Rönnquist, 2005:102, ISBN 82-471-7082-5 (printed version), ISBN 82-471-7081-7 (electronic version), ISSN 1503-8181.

"Initial Strength Development of Fly Ash and Limestone Blended Cements at Various Temperatures Predicted by Ultrasonic Pulse Velocity",
Tom Ivar Fredvik, 2005:112, ISBN 82-471-7105-8 (printed version), ISBN 82-471-7103-1 (electronic version), ISSN 1503-8181.

"Behaviour and modelling of thin-walled cast components",
Cato Dørum, 2005:128, ISBN 82-471-7140-6 (printed version), ISBN 82-471-7139-2 (electronic version), ISSN 1503-8181.

"Behaviour and modelling of selfpiercing riveted connections",
Raffaele Porcaro, 2005:165, ISBN 82-471-7219-4 (printed version), ISBN 82-471-7218-6 (electronic version), ISSN 1503-8181.

"Behaviour and Modelling og Aluminium Plates subjected to Compressive Load",
Lars Rønning, 2005:154, ISBN 82-471-7169-1 (printed version), ISBN 82-471-7195-3 (electronic version), ISSN 1503-8181

"Bumper beam-longitudinal system subjected to offset impact loading",
Satyanarayana Kokkula, 2005:193, ISBN 82-471-7280-1 (printed version), ISBN 82-471-7279-8 (electronic version), ISSN 1503-8181.

"Control of Chloride Penetration into Concrete Structures at Early Age",
Guofei Liu, 2006:46, ISBN 82-471-7838-9 (printed version), ISBN 82-471-7837-0 (electronic version), ISSN 1503-8181.

"Modelling of Welded Thin-Walled Aluminium Structures",
Ting Wang, 2006:78, ISBN 82-471-7907-5 (printed version), ISBN 82-471-7906-7 (electronic version), ISSN 1503-8181.

"Time-variant reliability of dynamic systems by importance sampling and probabilistic analysis of ice loads",
Anna Ivanova Olsen, 2006:139, ISBN 82-471-8041-3 (printed version), ISBN 82-471-8040-5 (electronic version), ISSN 1503-8181.

"Fatigue life prediction of an aluminium alloy automotive component using finite element analysis of surface topography",
Sigmund Kyrre Ås, 2006:25, ISBN 82-471-7791-9 (printed version), ISBN 82-471-7791-9 (electronic version), ISSN 1503-8181.

"Constitutive models of elastoplasticity and fracture for aluminium alloys under strain path change",
Dasharatha Achani, 2006:76, ISBN 82-471-7903-2 (printed version), ISBN 82-471-7902-4 (electronic version), ISSN 1503-8181.

"Simulations of 2D dynamic brittle fracture by the Element-free Galerkin method and linear fracture mechanics",
Tommy Karlsson, 2006:125, ISBN 82-471-8011-1 (printed version), ISBN 82-471-8010-3 (electronic version), ISSN 1503-8181.

"Penetration and Perforation of Granite Targets by Hard Projectiles",

Chong Chiang Seah, 2006:188, ISBN 82-471-8150-9 (printed version), ISBN 82-471-8149-5 (electronic version) ISSN 1503-8181.

“Deformations, strain capacity and cracking of concrete in plastic and early hardening phases”, Tor Arne Hammer, 2007:234, ISBN 978-82-471-5191-4 (printed version), ISBN 978-82-471-5207-2 (electronic version) ISSN 1503-8181.

“Crashworthiness of dual-phase high-strength steel: Material and Component behaviour”, Venkatapathi Tarigopula, 2007:230, ISBN 82-471-5076-4 (printed version) ISBN 82-471-5093-1 (electronic version) ISSN 1503-8181.

“Fibre reinforcement in load carrying concrete structures”, Åse Lyslo Døssland, 2008:50, ISBN 978-82-471-6910-0 (printed version), ISBN 978-82-471-6924-7 (electronic version), ISSN 1503-8181.

“Low-velocity penetration of aluminium plates”, Frode Grytten, 2008:46, ISBN 978-82-471-6826-4 (printed version) ISBN 978-82-471-6843-1 (electronic version) ISSN 1503-8181.

“Robustness studies of structures subjected to large deformations”, Ørjan Fylling, 2008:24, ISBN 978-82-471-6339-9 (printed version) ISBN 978-82-471-6342-9 (electronic version) ISSN 1503-8181.

“Constitutive modelling of morsellised bone”, Knut Birger Lunde, 2008:92, ISBN 978-82-471-7829-4 (printed version) ISBN 978-82-471-7832-4 (electronic version) ISSN 1503-8181.

“Experimental Investigations of Wind Loading on a Suspension Bridge Girder”, Bjørn Isaksen, 2008:131, ISBN 978-82-471-8656-5 (printed version) ISBN 978-82-471-8673-2 (electronic version) ISSN 1503-8181.

“Cracking Risk of Concrete Structures in the Hardening Phase”, Guomin Ji, 2008:198, ISBN 978-82-471-1079-9 (printed version), ISBN 978-82-471-1080-5 (electronic version) ISSN 1503-8181.

“Modelling and numerical analysis of the porcine and human mitral apparatus”, Victorien Emile Prot, 2008:249, ISBN 978-82-471-1192-5 (printed version), ISBN 978-82-471-1193-2 (electronic version), ISSN 1503-8181.

“Strength analysis of net structures”, Heidi Moe, 2009:48, ISBN 978-82-471-1468-1 (printed version), ISBN 978-82-471-1469-8 (electronic version) ISSN 1503-8181.